



THE HONG KONG
POLYTECHNIC UNIVERSITY

香港理工大學

Pao Yue-kong Library

包玉剛圖書館

Copyright Undertaking

This thesis is protected by copyright, with all rights reserved.

By reading and using the thesis, the reader understands and agrees to the following terms:

1. The reader will abide by the rules and legal ordinances governing copyright regarding the use of the thesis.
2. The reader will use the thesis for the purpose of research or private study only and not for distribution or further reproduction or any other purpose.
3. The reader agrees to indemnify and hold the University harmless from and against any loss, damage, cost, liability or expenses arising from copyright infringement or unauthorized usage.

IMPORTANT

If you have reasons to believe that any materials in this thesis are deemed not suitable to be distributed in this form, or a copyright owner having difficulty with the material being included in our database, please contact lbsys@polyu.edu.hk providing details. The Library will look into your claim and consider taking remedial action upon receipt of the written requests.

**OPTICAL COMMUNICATION AND SENSING DEVICES
BASED ON SPECIALTY FIBERS ASSISTED WITH
NOVEL MATERIALS**

WEIHAO YUAN

PhD

The Hong Kong Polytechnic University

2022

The Hong Kong Polytechnic University
Department of Electronic and Information Engineering

**Optical Communication and Sensing Devices Based on
Specialty Fibers Assisted with Novel Materials**

Weihaio Yuan

A thesis submitted in partial fulfillment of the requirements for the
degree of Doctor of Philosophy

August 2021

Certificate of Originality

I hereby declare that this thesis is my own work and that, to the best of my knowledge and belief, it reproduces no material previously published or written, nor material that has been accepted for the award of any other degree or diploma, except where due acknowledgment has been made in the text.

..... (Signed)

.....YUAN Weihao..... (Name of student)

Dedicated
To my Families

Abstract

In the thesis, we studied the various applications of novel structured fibers for optical communication and sensing devices.

For the part of optical communication, the light modulators assisted with 2D materials are introduced. The mechanisms of graphene-based light modulation and modulators with different fiber structures are presented. Then the light modulator with down-tapered SMF structure assisted with graphene is proposed and demonstrated. The performances of the proposed and successfully fabricated light modulator are studied and improved, and the analysis of experimental results is included. The experimental results demonstrate a feasible method for all-optical light modulation with down-tapered fiber structure assisted with graphene nanoflakes. The measured response time is up to 0.4 ns, indicating the potential for optical signal processing with bandwidth of up to 2.5 GHz. The research will play a very important part in the optical communication system to simplify the optical components and realize all-fiber light modulation.

For the part of sensing devices, the fiber sensors are introduced including characteristics of fiber sensors, different sensing principles and various physical structures. The fiber sensors are constructed by different structures, such as mismatched single-mode fibers, ring-core fiber and hollow core Bragg fiber. Firstly, a mismatched fiber structure is successfully created and simulated that demonstrates its application for sensing temperature and humidity based on cladding modes modulation. With CNT attached to the fiber, the sensitivity of temperature detection in small ranges is enhanced from 0.24561 to 1.65282 dB/°C, and the humidity sensing becomes more reliable for real application. Secondly, the

MZI fiber sensor based on SMF-NCF-RCF-SMF structure is successfully achieved. The experiments on temperature, RI and curvature sensing are conducted. Dual demodulation of temperature and RI is realized. The maximum sensitivity of temperature sensing is 69 pm/°C and that of RI sensing reaches 182.07 dB/RIU and -31.44 nm/RIU with the intensity and wavelength demodulation methods, respectively. The maximum sensitivity of curvature sensing is -3.68 nm/m⁻¹ with the measurement range of 1.3856 to 3.6661 m⁻¹. Based on the linear relationship between dip wavelength shift and the variation of temperature and curvature, these two parameters can be simultaneously demodulated by using the 2 × 2 matrix. Thirdly, an all-fiber sensor based on HCBF has been successfully created which displays excellent performance on human breath monitoring. The response time of the proposed sensor is around 0.15 s which enables the rapid and precise recording of breath signals. The applied distance between the fiber sensor and the human face is also investigated to reveal its influences on sensing results. Moreover, the HCBF sensor proves substantial insensitivity to temperature and curvature variation, which demonstrates its reliable sensing performance in different application environments.

The all fiber-based light modulator and fiber sensors are investigated which will be beneficial to explore the novel applications of fibers with different configurations.

Acknowledgments

Until now, I realize that I am going to reach the end of my study. Hereby, I want to thank a number of people during my Ph.D. studies. First, I would like to express my deepest appreciation to my supervisor, Prof. YU Changyuan. He not only provides me the opportunity to conduct my Ph.D. study in PolyU but also contributes great help and support to my research work. During the special and difficult COVID-19 period, he offered me the opportunity to do my research work in PolyU Shenzhen Institute so that my normal experimental work didn't be disturbed and bogged down. As a good mentor and friend, Prof. YU teaches me a lot, not only the professional knowledge and skills but also the enthusiasm and rigorous attitude of research.

In addition, I have met many good friends in PolyU who have offered me a lot of help on my Ph.D. study and daily life. Without them, I wouldn't conduct my research work smoothly. I want to thank Dr. LIU Yi and Dr. CHENG Xin who helped me a lot at the beginning of my Ph.D. study. I want to thank Dr. XUE Min, Dr. WANG Biwei, Dr. TAN Fengze, Mr. WANG Zhuo, Mr. LUO Huaijian, Mr. Abdullah Al Noman, Miss. CHEN Shuyang, Mr. YANG Zongru, Mr. LIU Yifan, Miss. QU Jiaqi, Mr. YU Jianxun. Also, I want to thank my partners in PolyU Shenzhen Base. I want to thank Dr. JIANG Shoulin, Dr. ZHAO Qiancheng, Mr. LI Lingduo, Mr. LYU Weimin, Mr. LIU Zhongxu, Mr. WANG Rui, Mr. ZHOU Jing, Mr. YANG Fangang, Mr. CHEN Feifan for their kind help on my experiments.

Finally, I want to thank my families. Without their full support, I wouldn't be able to complete my Ph.D. studies. Especially, I want to thank my wife, Mrs. LI Jiaying. Thank

you for your unconditional love, for accompanying me and for taking care of me during my Ph.D. study.

August 2021

Table of Contents

Certificate of Originality	i
Abstract.....	v
Acknowledgments.....	vii
Table of Contents	ix
List of abbreviations	xiii
List of major notations	xv
List of Figures	xvii
List of Tables	xxiii
1 Introduction.....	1
1.1 Overview.....	2
1.1.1 Optical fiber structure	2
1.1.2 Fiber modes.....	3
1.1.3 Fiber categories.....	5
1.2 Optical fibers assisted with graphene used for light modulation	7
1.2.1 The introduction of graphene material	7
1.2.2 The mechanism of graphene-based light modulation	11
1.2.3 Light modulators with different fiber structures.....	13
1.3 Optical fibers used for sensing	17
1.3.1 The characteristics of fiber optic sensors	19
1.3.2 The sensing principles of fiber sensors	20
1.3.3 Various physical structures of fiber interferometers	23

1.4 Research objectives	29
1.5 Organization of the thesis	30
1.6 Publications	31
2 All-Optical Light Modulator with Down-Tapered SMF Assisted with Graphene	33
2.1 Overview of light modulators.....	34
2.2 The experimental setups.....	36
2.3 The experiment results and analysis.....	39
2.4 Conclusion	45
3 The Humidity and Temperature Sensor Constructed by Mismatched SMFs Assisted with CNT.....	46
3.1 Introduction.....	47
3.1.1 The importance of humidity sensor	47
3.1.2 The introduction of CNT.....	47
3.2 Experiments and simulation work.....	48
3.2.1 The fabrication of humidity sensor.....	48
3.2.2 The experimental design.....	48
3.2.3 The simulation works.....	49
3.3 The sensing mechanism	50
3.4 Experimental results and discussions	52
3.4.1 The performance of temperature sensing.....	52
3.4.2 The performance of humidity sensing	54
3.5 Conclusion.....	56
4 The Fiber Sensor Based on RCF for Dual Demodulation of Temperature and RI	

.....	57
4.1 Introduction.....	58
4.2 Experimental setups	59
4.3 The sensing mechanism.....	61
4.4 Experimental results and analysis	64
4.4.1 The performance of temperature sensing	64
4.4.2 The performance of RI sensing	66
4.5 Discussion	69
4.6 Conclusion	70
5 The RCF-Based Sensor Used for Simultaneous Measurement of Temperature and Curvature	71
5.1 Introduction.....	72
5.2 Experimental setups.....	75
5.2.1 The structure of the curvature sensor	75
5.2.2 The experimental setups for curvature sensing	75
5.3 The sensing mechanism.....	77
5.3.1 The principles of temperature and curvature detection	77
5.3.2 The Rsoft simulation results	78
5.4 Experiments and discussions.....	80
5.4.1 The influence of NCF and RCF	80
5.4.2 The performance of curvature sensing	81
5.4.3 The performance of temperature sensing	83
5.4.4 The method for simultaneous measurement of temperature and curvature	85
5.5 Conclusion.....	86

6 The HCBF-Based Sensor for Human Breath Monitoring.....	88
6.1 Introduction.....	89
6.2 Fiber design and sensor fabrication	90
6.3 The sensing mechanism.....	93
6.4 Experimental results and analysis	96
6.4.1 Experimental setups	96
6.4.2 Test on human breath monitoring.....	96
6.4.3 Test on temperature and curvature sensitivity	100
6.5 Discussion	103
6.6 Conclusion	105
7 Conclusions and Suggestions for Future Research	106
7.1 Conclusions.....	107
7.2 Suggestions for future research.....	108
Bibliography	112

List of abbreviations

A

ALD	Atomic layer deposition
ARROW	Anti-resonant reflecting optical waveguide
APD	Avalanche photodetector
ASE	Amplified spontaneous emission

B

BBS	Broadband source
-----	------------------

C

CNT	Carbon nanotube
CVD	Chemical vapor deposition
CW	Continuous wave

D

DSP	Digital signal processing
-----	---------------------------

E

EDFA	Erbium-doped fiber amplifier
EOM	Electro-optic modulator
ER	Extinction ratio

F

FBG	Fiber Bragg grating
FMF	Few mode fiber
FPI	Fabry-Pérot interferometer
FSR	Free spectral range
FUT	Fiber under test
FWM	Four-wave mixing
FWHM	Full-width at half-maximum

G

GeO ₂	Germanium oxide or Germanium dioxide
------------------	--------------------------------------

H

HCBF	Hollow core Bragg fiber
------	-------------------------

L

LEAF	Large effective area fiber
------	----------------------------

M		
MCF		Multi-core fiber
MD		Modulation depth
MF		Microfiber
MMF		Multimode fiber
MOFI		Miniaturized optical fiber interferometer
MZI		Mach-Zehnder interferometer
N		
NCF		No core fiber
O		
OSA		Optical spectrum analyzer
OSNR		Optical signal-to-noise ratio
OT		Optical transmittance
OTDR		Optical time domain reflectometry
P		
PC		Polarization controller
PCF		Photonic crystal fiber
POF		Plastic optical fiber or Polymer optical fiber
PD		Photodetector
R		
RCF		Ring core fiber
RF		Radio frequency
RH		Relative humidity
S		
SMF		Single-mode fiber
SNR		Signal-to-noise ratio
T		
TL		Tunable laser
W		
WDM		Wavelength division multiplexing

List of major notations

V	Volume of medium
E	Electric field of optical wave
c	Velocity of light in vacuum
μ_0	Vacuum magnetic permeability
ϵ_0	Vacuum permittivity
ϵ_g	Relative permittivity of graphene
χ	Dielectric susceptibility or Electric susceptibility
ρ	Density of medium
T	Temperature
γ_e	Electrostrictive coefficient
κ	Thermal conductivity of medium
q, \mathbf{q}	Wave number/wave vector of density fluctuation
Ω	Rotation
k, \mathbf{k}	Wave number/wave vector of optical field
ω	Frequency (angular) of optical wave
n	Refractive index
λ	Optical wavelength
ν	Frequency of optical wave
\mathbf{e}	Normalized polarization vector of optical field
A	Normalized amplitude of optical field
α	Attenuation coefficient of optical fiber
γ	Nonlinear parameter of optical fiber
A_{eff}	Effective mode area of optical fiber
P	Power of optical field
L_{eff}	Effective length of optical fiber
$\Delta\tau$	Pulse width

ΔT	Variation of temperature
L	Fiber length
v_g	Group velocity
σ	Normalized amplitude error (Normalized noise level)
n_s	Carrier density
v_F	Fermi velocity
ω	Radian frequency
μ_c	Chemical potential
Γ	Scattering rate
t_g	Thickness of graphene

List of Figures

Figure 1.1: The schematic diagrams of (a) cross-section view of optical fiber and (b) light transmission in the fiber core.....	2
Figure 1.2. The schematic diagram of graphene.	8
Figure 1.3. Overview of different light modulation methods with thermal (red), electrical (green) and optical (blue) excitations. The data are adapted from [14].	11
Figure 1.4. Typical approaches for 2D material-based optical modulation. The data are adapted from [14].....	12
Figure 1.5: The schematic diagram of the optical amplitude modulator. (a) The diagram of graphene coated down-tapered SMF, (b) Differential transmittance of the probe light through a 1.4 μm GCM with 20 μm long graphene cladding as a function of the pump–probe time delay with a pump power of 200 nW, showing a response time of ~ 2.2 ps. The data are adapted from [19].....	15
Figure 1.6: The schematic diagram of optical Kerr effect phase modulator based on (a) optical amplitude modulation in a GCM, and (b) optical phase modulation in a GCM in one arm of an all-fiber MZI. VOA, variable optical attenuator; WDM, wavelength division multiplexing; MF, microfiber; APD, avalanche photodetector. The data are adapted from [20].....	16
Figure 1.7: The schematic diagram of optical thermal effect modulator. (a) Schematic of the experimental setup for measuring the phase shift of light transmitting in graphene-coated microfiber, (b) measured interference patterns without (blue) and with (red) pumping laser. The data are adapted from [18]. ..	17
Figure 1.8. The schematic diagram of microbend fiber sensor.....	21

Figure 1.9. The schematic diagram of MZI.....	24
Figure 1.10. The schematic diagram of Michelson fiber interferometer.....	25
Figure 1.11. The schematic diagram of Sagnac fiber interferometer.	26
Figure 1.12. The schematic diagram of FPI.	27
Figure 2.1. The experimental setups of the fiber tapering process and light modulation.....	37
Figure 2.2. The image of the fiber tapering machine.	38
Figure 2.3. The user interface of the FTM software.	38
Figure 2.4. The relationship between input power and output power through the pure microfiber (blue points) and graphene-coated microfiber (red points)	39
Figure 2.5. The transmission spectrum of femtosecond laser.....	40
Figure 2.6. The oscillogram of the femtosecond laser used for pumping.	40
Figure 2.7. The oscillogram of the output signals with different input light of (a) 200 mA pumping laser only (b) 200 mA pumping laser and CW laser (c) 400 mA pumping laser only (d) 400 mA pumping laser and CW laser (e) 600 mA pumping laser only (f) 600 mA pumping laser and CW laser.	41
Figure 2.8. The microscope images of (a) normal fiber and (b) tapered fiber.....	42
Figure 2.9. The oscillogram of femtosecond laser and continuous-wave laser with (a) 1550 nm filter and (b) 1530 nm filter.....	43
Figure 2.10. The oscillogram of femtosecond laser and CW laser with different CW laser energy of (a) 10 mW and (b) 20 mW.....	43
Figure 2.11. The response time of light modulation assisted with graphene nanoflakes.....	44
Figure 3.1: (a) The schematic diagram of the mismatched SMF and (b) the	

microscope images of the mismatched node and (c) the CNT coated part [68]..	
.....	49
Figure 3.2: The Rsoft simulation results of the proposed sensor with (a-c) normal cladding and (d-f) thick cladding [68]. .	50
Figure 3.3: The relationship between the wavelength shift of the interference dip and the temperature variation from 40 to 125 °C with the step of 5 °C [68].....	52
Figure 3.4: The relationship between the temperature and the intensity of interference dips at the wavelength of 1593 nm [68].....	53
Figure 3.5: The spectra of temperature sensing (a) without and (b) with CNT coating [68].....	54
Figure 3.6: The relationship and linear fit between temperature variation and the intensity change of interference dips without (blue line) and with (red line) CNT coating [68].....	54
Figure 3.7: The spectra of relative humidity (RH) and interference wavelength (a) without and (b) with CNT attached [68].....	55
Figure 3.8: The relationship and linear fit between RH and interference dip wavelength without (blue line) and with (red line) CNT attached [68]..	56
Figure 4.1: (a) The microscope images of RCF and (b) the RI distribution along the diameter (dash line) [108].	60
Figure 4.2: The schematic diagram of the MZI with the SMF-NCF-RCF-SMF structure [108].....	60
Figure 4.3: The Rsoft simulation results of (a) SMF-RCF-SMF structure and (b) SMF-NCF-RCF-SMF structure [108].....	61
Figure 4.4: The interference spectrum of the MZI (inset) and the FFT spectrum	

[108].....	63
Figure 4.5: (a) The interference spectra of the proposed MZI sensor at different temperatures from 35 °C to 70 °C with the interval of 5 °C and (b) the relationship between temperature and dip wavelength with temperature increasing and decreasing [108].....	66
Figure 4.6: The relationship between temperature and intensity of interference dips at the dip wavelength around 1508 nm [108].	66
Figure 4.7: (a) The MZI interference spectra with different RIs ranging from 1.33 to 1.38 with the interval of 0.01 and (b) the relationship between RI and the intensity of interference dips [108].	67
Figure 4.8: The mathematical statistics of RI and wavelength shift at the dip of around 1505 nm [108].	68
Figure 5.1: The microscope images of section views of NCF and RCF [137].....	75
Figure 5.2: The schematic diagrams of (a) the experimental setup for curvature sensing and (b) the MZI sensor based on the RCF [137].	76
Figure 5.3: The Rsoft simulation results of light transmission in (a) straight RCF and (b) curved RCF [137].	79
Figure 5.4: The simulated mode distribution of the cross-section region of the straight RCF with the transmission distance of (a) 1 mm, (b) 10 mm, (c) 20 mm, and that of the curved RCF with the transmission distances of (d) 1 mm, (e) 10 mm, and (f) 20 mm [137].....	79
Figure 5.5: (a) The interference spectra of 1-mm NCF MZI sensor with different lengths of RCF at 10 cm, 6.7 cm, 4.3 cm, 2.5 cm, 2 cm, 1.5 cm, 1 cm, and 0.5 cm and (b) that of 2-cm RCF MZI sensor with different lengths of NCF at 10 mm, 7	

mm, 5 mm, 3 mm, 1 mm and 0 [137].	81
Figure 5.6: The interference spectra of the MZI fiber sensor with different bending curvatures [137].	82
Figure 5.7: (a) The interference spectra of dip 1 with different curvature and (b) the relationship between curvature and dip wavelength with curvature increasing and decreasing [137].	82
Figure 5.8: (a) The interference spectra of dip 2 with different curvature and (b) the relationship between curvature and dip wavelength with curvature increasing and decreasing [137].	83
Figure 5.9: The interference spectra of (a) dip 1 and (b) dip 2 with different temperatures from 25 °C to 55 °C with an interval of 5 °C [137].	84
Figure 5.10: The mathematical statistics of temperature and wavelength shift of (a) dip 1 and (b) dip 2 [137].	84
Figure 5.11. The linear relationship between curvature and wavelength of dip 1 (red line) and dip 2 (blue line) [137].	85
Figure 6.1: (a) The cross-section view of HCBF and (b) refractive index distribution along the radial direction [171].	91
Figure 6.2: (a) The schematic diagram of HCBF based sensor and (b) the microscope image of splicing point between HCBF and SMF [171].	92
Figure 6.3: The schematic diagram of the guiding mechanism of the HCBF [171].	93
Figure 6.4: The transmission spectra of the (a) HCBF and (b) HCC with both lengths of 7 mm [171].	95
Figure 6.5: The schematic diagram of experimental setups [171].	96

Figure 6.6: (a) The transmission spectra of fiber sensor without breath (red line) and with breath (blue line) and (b) electrical signals without breath (black line) and with breath (red line) [171]..... 97

Figure 6.7: Breath signal with one deep expiration [171] 98

Figure 6.8: (a) Electrical signals with different distances between the human face and fiber sensor at 2 cm, 5 cm, and 10 cm and (b) response time of human breath monitoring [171] 99

Figure 6.9: The transmission spectra of fiber sensor at different temperatures of 25 °C, 30 °C, 35 °C, 40 °C, 45 °C, 50 °C [171] 100

Figure 6.10: (a) The details of transmission spectra at different temperatures of 25 °C, 30 °C, 35 °C, 40 °C, 45 °C, 50 °C, (b) the peak intensities statistics at different temperatures and (c) the relationship between temperature and dip (1550 nm) wavelength [171]..... 101

Figure 6.11: The schematic diagram of the experimental setup for curvature sensing [171] 101

Figure 6.12: (a) The transmission spectra of fiber sensor with different curvature values of 0, 0.8841, 1.5313, 1.9769, 2.7957, 3.4240, 3.9537, 4.4204 m⁻¹ and (b) the peak intensities statistics at different curvature values [171]..... 102

Figure 7.1. Schematic diagram of electrically controlled graphene based electro-optical modulator. 109

List of Tables

Table 6.1 Comparison of the key parameters between the proposed all-fiber sensor and other recent-developed fiber-optic sensors in literatures for human breath monitoring [171]	103
---	-----

1 Introduction

In this chapter, the overview of optical fibers is presented including the fiber structures, fiber modes and fiber categories. Then the all-fiber light modulators assisted with 2D materials are introduced. The mechanism of 2D materials-based light modulation and modulators with different fiber structures are illustrated. After that, the fiber sensors are introduced including characteristics of fiber sensors, different sensing principles and various physical structures. Subsequently, research objectives and outlines of the thesis are given. Finally, the publications during the period of the Ph.D. study are highlighted.

1.1 Overview

1.1.1 Optical fiber structure

Optical fiber is a kind of dielectric waveguides that works in the optical waveband. Optical fibers are generally known as cylindrical structures which can confine the electromagnetic wave energy within the internal interfaces based on the principle of total reflection. The transmission light in the fiber will be guided along the direction of the fiber axis. The transmission characteristics of an optical fiber are determined by its structure and material.

Generally, an optical fiber is constructed of three parts: core, cladding and jacket, as shown in Figure 1.1(a). The fiber core serves as the inner layer and cladding is the outer layer. The refractive index of the core is slightly larger than that of the cladding to satisfy the total reflection. When the incident light meets particular conditions, the light wave can be confined in the core area and propagate forward along the core axis. As the core-cladding structure can be vulnerable to the external environment, the actual optical fiber has a protective layer (jacket) outside the cladding, which is used to protect the optical fiber from environmental pollution and mechanical damage. In addition, some optical fibers have more complex structures to meet different requirements in practical applications.

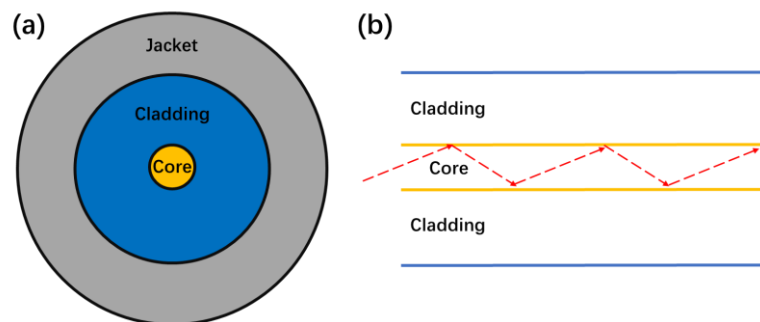


Figure 1.1: The schematic diagrams of (a) cross-section view of optical fiber and (b) light transmission in the fiber core.

1.1.2 Fiber modes

Light is a kind of electromagnetic wave with a much higher frequency compared to radio waves. Thus, the fundamental properties of light wave transmitting in optical fibers can be derived from the basic equations of electromagnetic field, namely Maxwell's equations.

The electromagnetic field in the vacuum can be described by two vectors, electric field intensity (E) and magnetic induction intensity (B). To describe the effect of the field on matter, three vectors are introduced which are electric displacement vector (D), magnetic field intensity (H) and conduction current density (J). The five vectors will vary with the change of time and space and the relationship can be determined by Maxwell's equations:

$$\nabla \times \vec{E} = -\frac{\partial \vec{B}}{\partial t} \quad (1.1)$$

$$\nabla \times \vec{H} = \frac{\partial \vec{D}}{\partial t} + \vec{J} \quad (1.2)$$

$$\nabla \cdot \vec{D} = \rho \quad (1.3)$$

$$\nabla \cdot \vec{B} = 0 \quad (1.4)$$

Maxwell's equations indicate the relation between E , D , B and H . To find out the propagation law of light waves in optical fibers, the relation between each factor with time and space should be figured out. We can use the following formula transformation to work out the relationship between E (or H) with time and space based on Maxwell's equations:

$$\nabla \times (\nabla \times \mathbf{E}) = -\nabla \times \frac{\partial \mathbf{B}}{\partial t} = -\frac{\partial (\nabla \times \mu \mathbf{H})}{\partial t} \quad (1.5)$$

$$\nabla \times (\nabla \times \mathbf{H}) = \frac{\partial (\nabla \times \varepsilon \mathbf{E})}{\partial t} + \nabla \times \mathbf{j} \quad (1.6)$$

After the formula transformation, we can get

$$\nabla^2 E + \nabla \left(E \cdot \frac{\nabla \varepsilon}{\varepsilon} \right) - \nabla \left(\frac{\rho}{\varepsilon} \right) + \frac{\nabla \mu}{\mu} \times \nabla \times E = \mu \varepsilon \frac{\partial^2 E}{\partial t^2} + \mu \frac{\partial j}{\partial t} \quad (1.7)$$

$$\nabla^2 H + \nabla \left(\frac{\nabla \varepsilon}{\varepsilon} \cdot H \right) + \frac{\nabla \varepsilon}{\varepsilon} \times \nabla \times H = \mu \varepsilon \frac{\partial^2 H}{\partial t^2} + \frac{\nabla \varepsilon}{\varepsilon} \times j - \nabla \times j \quad (1.8)$$

Considering the light transmitting in optical fiber, we have $\mu = \mu_0$, $\rho = 0$, the equations can be further simplified as

$$\nabla^2 \mathbf{E} + \nabla \left(\mathbf{E} \cdot \frac{\nabla \varepsilon}{\varepsilon} \right) = \mu_0 \varepsilon \frac{\partial^2 \mathbf{E}}{\partial t^2} \quad (1.9)$$

$$\nabla^2 \mathbf{H} + \frac{\nabla \varepsilon}{\varepsilon} \times \nabla \times \mathbf{H} = \mu_0 \varepsilon \frac{\partial^2 \mathbf{H}}{\partial t^2} \quad (1.10)$$

For uniform fiber structure, ε can be seemed as a constant, so that we have

$$\nabla^2 \mathbf{E} = \mu_0 \varepsilon \frac{\partial^2 \mathbf{E}}{\partial t^2} \quad (1.11)$$

$$\nabla^2 \mathbf{H} = \mu_0 \varepsilon \frac{\partial^2 \mathbf{H}}{\partial t^2} \quad (1.12)$$

For homogeneous light, we have

$$\mathbf{E}(\mathbf{r}) = \mathbf{E}_0(\mathbf{r}) \exp[-ik_0 \varphi(\mathbf{r})] \exp[i\omega t] \quad (1.13)$$

$$\mathbf{H}(\mathbf{r}) = \mathbf{H}_0(\mathbf{r}) \exp[-ik_0 \varphi(\mathbf{r})] \exp[i\omega t] \quad (1.14)$$

After the formula transformation, we can get

$$\nabla^2 \mathbf{E} + k^2 \mathbf{E} = 0 \quad (1.15)$$

$$\nabla^2 \mathbf{H} + k^2 \mathbf{H} = 0 \quad (1.16)$$

The above equations are known as Helmholtz equations. According to Helmholtz equations and given boundary conditions, the characteristic solutions can be figured out and each characteristic solution is named one mode. The fiber mode is a basic concept in the optical waveguide. When a fiber mode transmits along the longitudinal direction, its field distribution is constant which means that it has a stable distribution along the z-direction. It should also be noted that the total field distribution in an optical waveguide is a linear superposition of the fiber modes and different modes satisfy the orthogonality relation.

1.1.3 Fiber categories

When the light wave propagates in an optical fiber, the solution of the electromagnetic field is discontinuous due to the limitation of the core boundary. The discontinuous solutions of the electromagnetic field are called fiber modes. The fibers can be classified into two categories according to the number of transmission modes: single-mode fiber (SMF) and multi-mode fiber (MMF). The fiber that can only transmit one mode is called single-mode fiber, and fiber that can transmit multiple modes at the same time is called multi-mode fiber. The main differences between SMFs and MMFs are the size and refractive index (RI) differentials between core and cladding. For MMFs, the diameter of the fiber core is large (50~500 μm), and the RI difference between core and cladding is large ($\Delta = 0.01 \sim 0.02$). For SMFs, the diameter of the fiber core is small (2~12 μm), and the RI difference between core and cladding is small ($\Delta = 0.005 \sim 0.01$). Except for the aforementioned SMFs and MMFs, the optical fibers can also be classified into various categories according to different classification criteria. There are some examples listed below.

Based on the RI distribution in the core area, fibers can be divided into step-index fiber and gradient-index fiber. The former one has the uniform RI distribution of the core, and there is an abrupt change (or step change) of RI at the interface between the core and the cladding. For the gradient-index fiber, the RI of the core shows gradient changes from the fiber center to the core-cladding interface in the radial direction. And also, the RI alteration has a certain functional relationship with the distance to the fiber center.

Based on the polarization state of transmission, SMFs can be further divided into non-polarization-maintaining fibers (non-PMFs) and polarization-maintaining fibers (PMFs). The difference between the two kinds of fibers is that the former cannot transmit polarized light while the latter can. PMFs can be further divided into four types: single-polarization

fibers, high birefringence fibers, low birefringence fibers, and circular polarization-maintaining fibers. Single polarization fiber means a PMF that can only transmit one polarization mode. The fiber that can only transmit two orthogonal linear polarization modes with different propagation speeds is called high birefringence fiber, and that with nearly equal propagation speed is low birefringence fiber. The one that can transmit circularly polarized light is called circular birefringent fiber.

Based on the materials used to manufacture the optical fiber, it can be divided into high-purity fused silica fiber, multi-component glass fiber, plastic optical fiber (POF), infrared optical fiber, liquid core fiber, crystal fiber and photonic crystal fiber (PCF). High-purity fused silica fiber is characterized by extremely low optical transmission loss which can be as low as 0.2 dB/km at a certain wavelength (generally less than 1 dB/km). Multi-component glass fiber is characterized by the large RI between the core and cladding, which is beneficial to the manufacture of fibers with a large numerical aperture (NA). However, the transmission loss is generally large (1 dB/m in the visible light band), which is hundreds of times larger than that of quartz fiber. POF is characterized by low cost, large variable range of RI and easy doping to meet different requirements. Nevertheless, the POF has some disadvantages, such as large transmission loss and poor stability under high temperatures. Infrared optical fiber is characterized by high transmittance in near-infrared (1~5 μm) and mid-infrared (~10 μm) waveband and the shortcoming is large transmission loss. Liquid core fiber is known as a special fiber structure with a liquid core that can meet special needs. Crystal fiber has a monocrystal core that can be used to manufacture various active and passive optical fiber devices. Photonic crystal fiber is a new type of fiber that has appeared in the past decade which has many special optical transmission characteristics.

1.2 Optical fibers assisted with graphene used for light modulation

1.2.1 The introduction of graphene material

In the past 20 years, carbon nanomaterials have been the frontier of scientific and technological innovation. The discovery of fullerenes in 1985 and carbon nanotubes in 1991 both caused a huge research boom [1, 2]. In 2004, British scientists discovered a new type of two-dimensional atomic crystal composed of hybrid connected monoatomic layers, namely graphene, which is constructed by basic structural units of benzene six-membered ring [3]. Graphene is seemed as the ideal two-dimensional nanomaterial and the discovery of graphene has enriched the family of carbon materials and formed a complete system of zero-dimensional fullerenes, one-dimensional carbon nanotubes, two-dimensional graphene and three-dimensional diamond and graphite. Since 2004, research results on graphene have been published in SCI indexed journals more than thousands of papers [4]. Graphene has shown great scientific significance and application values in both theoretical and experimental research. Through more extensive and in-depth research in the field of graphene functionalization, people have been aware of this new type of 2D material and gained more comprehensive and profound understanding of the intrinsic structure and properties of graphene. A series of new materials with superior performance based on graphene are produced and the practical applications of graphene are developed on the strength of the scientific and technological foundation.

Graphene is composed of a monolayer of carbon atoms wrapped in a honeycomb crystal lattice, as shown in Figure 1.2. It is the thinnest two-dimensional material with a thickness of only 0.35 nm and a carbon-carbon bond length of 0.142 nm [5]. The unit cell

is constructed by six carbon atoms and the angle between adjacent atoms is 120° . There are one s orbital and two in-plane p orbitals in each carbon atom which enables graphene to gain strong mechanical stability. The remaining p orbital, perpendicularly oriented to the molecular plane, hybridizes to form the p^* (conduction) and p (valence) bands, which dominate the planar conduction phenomena [4]. The special structure of graphene indicates the rich and novel physical phenomena, which makes graphene exhibit many excellent properties. For example, the strength of graphene reaches 130 GPa [6], which is more than 100 times larger than that of steel; the room-temperature carrier mobility is theoretically up to $10^5 \text{ cm}^2 \cdot \text{V}^{-1} \cdot \text{s}^{-1}$ [7], which is 50 times larger than that of the GaAs material and 60 times larger than that of commercial silicon wafers. Under certain conditions (such as low-temperature quenching, etc.), the carrier mobility of graphene can even reach $250000 \text{ cm}^2 \cdot \text{V}^{-1} \cdot \text{s}^{-1}$ [5]. The thermal conductivity of graphene can reach $5000 \text{ W} \cdot \text{mK}^{-1}$ [8], which is three times larger than that of the diamond. In addition, graphene also has special properties such as room-temperature quantum Hall effect [9] and room-temperature ferromagnetism [10].

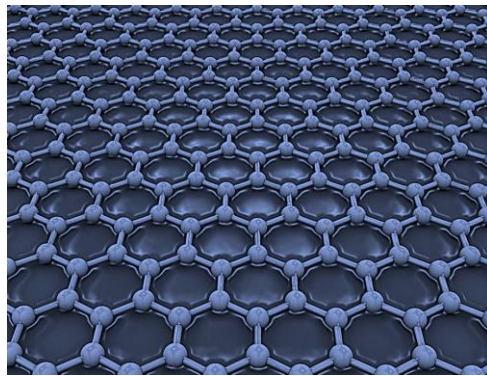


Figure 1.2. The schematic diagram of graphene

Graphene can be prepared for various flexible electronic devices and functional composite materials due to its excellent mechanical and optoelectronic properties, special single-atom layer with planar two-dimensional structure and high specific surface area. Benefiting from the unique advantages of excellent performance, low cost and good

processability, graphene has great application prospects in the fields of electronics, information, energy, materials, and biomedicine, and it is expected to set off a new technological revolution in the 21st century.

Benefiting from the excellent physical and electrical properties, graphene shows tremendous potential in the sensing field. Here we take gas sensing as an example. Because of the charge transfer within the molecule, the weak hybridization between the electron orbitals of the molecule (especially the small molecule) can lead to significant changes in its electronic properties. Since electrons on the graphene surface are mainly π electrons and are mainly distributed near the Fermi level, the weak coupling will result in the change of the Fermi level and disturb the π electron energy. Further, the adjustment of the Fermi level can give rise to the change of conductivity. Therefore, the conductivity of graphene is very sensitive to external disturbance which enables graphene to be applied on gas sensing. The adsorption of small molecules, such as NO_2 , H_2O , CO , NH_3 , etc., will significantly change the Fermi level of graphene which can further induce the variation of conductivity. Even the single-molecule adsorption can be detected through the current change.

Benefiting from the good optical and electrical properties, graphene can be applied on optical and optoelectronic devices [11, 12]. Graphene has been used as the transparent conductive layer due to the unique characteristics of low resistance and high light transmittance [11, 12]. For example, in inorganic, organic and dye-sensitized solar cells, graphene can serve as both the transparent conductive layer and the hole transport layer. Since the band gap of graphene is close to 0 eV, it can absorb electromagnetic waves from ultraviolet to terahertz which enables graphene-based photodetectors to immensely broaden the bandwidth of light detection [12]. In addition to the extension of bandwidth, graphene with high carrier concentration will enable the photodetector to have an ultra-fast response speed. Except for large-area graphene, the nanoscale graphene also exhibits good

mechanical, chemical and electrical properties. Thus, graphene can also be used to manufacture molecular-scale electronic devices. Graphene can serve as semiconductor layers in transistors, field-effect transistors (FETs), and integrated circuits. In addition, graphene is also used as capacitor material.

People have made positive progress in the preparation of graphene and developed various preparation methods such as mechanical exfoliation, crystal epitaxial growth, chemical oxidation, chemical vapor deposition (CVD), and organic synthesis [5]. The continuous improvement of preparation technology promotes the basic research and application development of graphene. In addition, to extend the application of graphene, controllable functionalization is also very important [5]. The structurally complete graphene is a two-dimensional crystal composed of benzene six-membered rings without any unstable bonds. Thus, it has an inert surface with high chemical stability which is hard to interact with other media (such as solvents). And also, there is strong van der Waals' force between the graphene sheets which are prone to aggregation, making it difficult to dissolve in water and common organic solvents. This has caused great difficulties for the further research and application of graphene. In order to take full advantage of its excellent properties and improve its molding processability (such as improving solubility and dispersibility), graphene must be effectively functionalized. By introducing specific functional groups, graphene can exhibit new properties which will further expand its application fields [5]. Functionalization is one of the most important approaches to realize the dispersion, dissolution and forming of graphene. The discovery of graphene with two-dimensional crystals has opened an exciting page for the study of condensed matter physics and provided new opportunities in the fields of chemistry and materials.

1.2.2 The mechanism of graphene-based light modulation

Various light-modulation methods based on graphene have been developed in recent years, including thermal, electrical and optical excitations, as shown in Figure 1.3. For different modulation approaches, the mechanisms are also different. Graphene is generally known as 0 bandgap which means that the electrons in the ground state of graphene can be easily excited to higher energy levels due to the effect of energy absorption (thermal, electrical and optical effect) and the Fermi level of graphene will accordingly be influenced [13]. Graphene with different Fermi levels will show various optical properties. The light absorption capability and effective RI of graphene can be modified, based on which graphene material can be integrated with optical fibers for light amplitude modulation and phase modulation. From Figure 1.3, the response time of light modulation using different modulation methods can be found. Generally, the thermal modulation has a modulation speed ranging from ms to μ s which is much slower than electrical modulation with a modulation speed of around ns. The optical modulation method demonstrates the highest modulation rate up to fs.

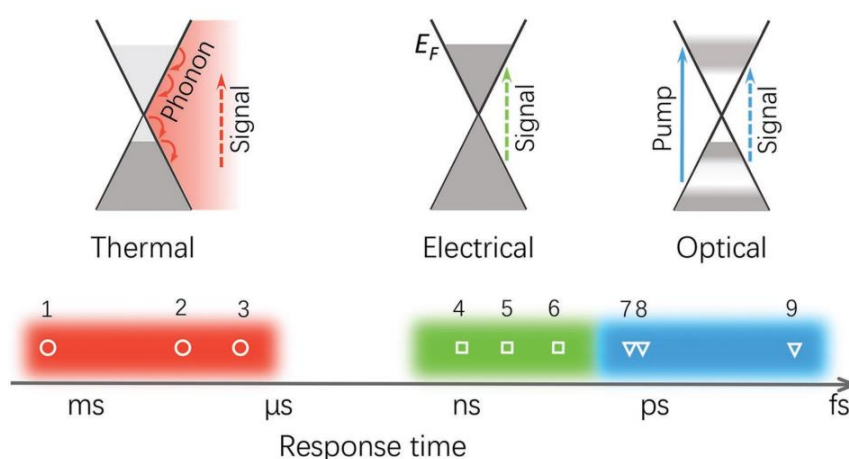


Figure 1.3. Overview of different light modulation methods with thermal (red), electrical (green) and optical (blue) excitations. The data are adapted from [14]

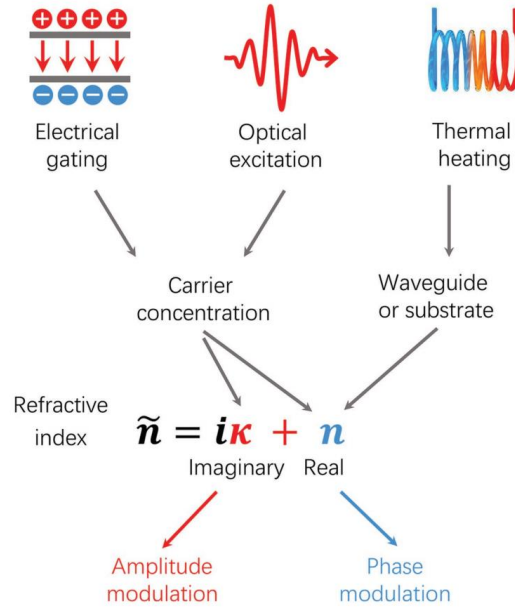


Figure 1.4. Typical approaches for 2D material-based optical modulation. The data are adapted from [14]

Figure 1.4 displays the mechanisms of light modulation (including amplitude modulation and phase modulation) with different approaches of electrical gating, optical excitation and thermal heating. The RI of graphene can be divided into two parts: imaginary part and real part. The imaginary part determines the coefficient of light absorption and the real part means the optical dispersion. It can be seen from Figure 1.4 that both electrical gating and optical excitation can give rise to the significant change of carrier concentration which will further result in the alteration of both the imaginary part and real part of RI. Thus, the electrical and optical methods can be applied for both amplitude modulation and phase modulation. Compared with the electrical and optical approaches, the thermal-optic coefficient of graphene is not large enough to induce the remarkable change of RI. Therefore, the thermal energy generated by graphene can be transferred to the fiber substrate which will result in the temperature and RI change of the whole structure.

In 2011, a graphene-based waveguide-integrated optical modulator was firstly developed by the research group of Liu et al [15]. By tuning the Fermi level of graphene

sheet with electrical method, the waveguide modulator with modulation frequency of 1.2 GHz and broad operation range from 1.35 to 1.6 μm was experimentally demonstrated. In 2014, Li et al. reported a silicon waveguide-based light modulator assisted with monolayer graphene which has the 3 dB bandwidth of 2.5 GHz for modulation [16]. In 2015, Lipson et al. demonstrated a graphene electro-optic modulator with 30 GHz bandwidth and modulation efficiency of 15 dB per 10 V [17]. The silicon waveguide-based light modulator presents combined advantages, such as compact footprint, low operation voltage, ultrafast modulation speed and broad operation range, etc. However, there are still some challenges. For example, the waveguide modulator relies on electro-absorption of graphene which means that the modulation speed can be limited by the charge-discharge frequency of capacitor. In addition, the large coupling loss between the silicon waveguide and fiber communication channel will be a big problem. Therefore, a fiber-based light modulator is proposed to solve the key issues. Firstly, by using the fiber tapering technology, different approaches can be developed for graphene-based light modulation, such as electrical gating, femtosecond laser pumping and thermal heating. Moreover, the fiber-based modulator can directly fusion splice with communication channel, giving rise to relatively low connection loss. Therefore, the all fiber-based light modulator assisted with graphene can be promising to realize ultrafast modulation speed and low coupling loss when it is applied in optical communication system.

1.2.3 Light modulators with different fiber structures

In 2009, the research group of Prof. Kian Ping Loh successfully fabricated a mode-locked fiber laser using atomic-layer graphene as the saturable absorber for the first time [18]. This makes it possible for a graphene-based high-frequency modulator. Three kinds of fiber-

based optical modulators are introduced below which include optical saturable absorption modulator, optical Kerr effect modulator and optical thermal effect modulator. The optical saturable absorption modulator, which is also known as amplitude modulator, is based on the good absorption coefficient of graphene. As mentioned above, graphene with one atom thickness can absorb 2.3% of vertically incident light which gives rise to the probability of light modulation with 2D materials [19]. When the energy density of the introduced laser is very high, the absorption spectrum of graphene will be significantly changed because of the sharp increase of excited carriers. Based on the principle of the Pauli blocking effect, no more photons can be absorbed to induce the transition of carriers from ground state to excited state which is known as saturable absorption. By inducing the saturable absorption of graphene, the capability of light absorption will be significantly influenced and thus the signal light can mostly go through or be absorbed controlled by the status of graphene. As reported by the research group of Prof. Limin Tong [19], an ultrafast light modulator based on graphene-coated microfiber (GCM) has been demonstrated. Two laser beams with different wavelengths (980 nm as pumping laser and 1550 nm as probe laser) and power densities (pumping laser with high energy density and probe laser with lower energy density) are coupled in a down-tapered single-mode fiber coated with graphene (Figure 1.5(a)). When the high-power pumping laser is on, the graphene can be induced in the status of saturated absorption and hence a part of the signal light will not be absorbed which gives rise to the observable signals on the receiving end. The signal light will be mostly absorbed by graphene when the pumping laser is cut off. By coding the pumping light, the signal modulation can be easily realized. The GCM-based all-optical modulation has a fast response time of ~ 2.2 ps which is equal to the bandwidth of ~ 200 GHz, as shown in Figure 1.5(b) [19].

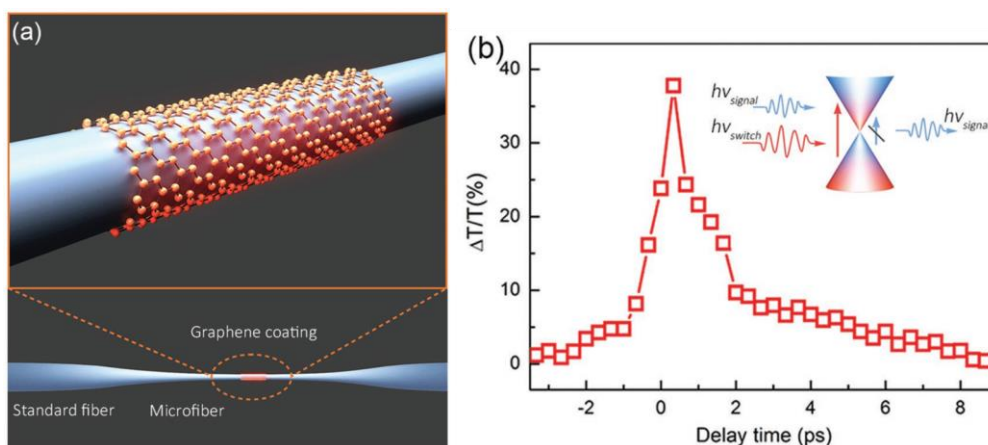


Figure 1.5: The schematic diagram of the optical amplitude modulator. (a) The diagram of graphene-coated down-tapered SMF, (b) Differential transmittance of the probe light through a $1.4\ \mu\text{m}$ GCM with $20\ \mu\text{m}$ long graphene cladding as a function of the pump-probe time delay with a pump power of 200 nW, showing a response time of ~ 2.2 ps. The data are adapted from [19]

The graphene-based optical Kerr effect phase modulator is based on the different mechanism from the amplitude modulator. On the strength of the strong nonlinearity of graphene, the refractive index can be tuned with the effect of a high-power laser which will further induce the phase shifting of the signal light. As reported by the research group of Prof. Jianlin Zhao, a Mach-Zender Interferometer is applied for the optical phase modulator [20]. Figure 1.6 displays the schematic diagram of the optical phase modulator based on the principle of Kerr effect. One of the two light paths is coated with graphene on the down-taper structure part and the other path uses no materials. Similar to the optical amplitude modulator, two beams of laser (980 nm as pumping laser and 1550 nm as probe laser) are coupled in the Mach-Zender Interferometer and the splitting ratio of the coupler is set to be 90/10 [20]. This is because that the down-tapered fiber will lead to a low transmission of light energy compared to normal SMF in the other path. The applied 90/10 coupler can to some extent balance the output signals from two paths and guarantee a relatively large extinction ratio. Because of the strong light-matter effect, the refractive index of coated graphene will be adjusted by modulation laser with high power density which can give rise

to phase shifting of the signal light compared with the condition that the modulation light is cutoff. The induced phase shift can lead to destructive or constructive interference and the signal modulation can be realized. The phase modulator has better optical transmittance and modulation depth compared to the amplitude modulator and the response time of both are similar. However, the application of the Mach-Zender interferometer results in a more complicated structure which can influence the design of the phase modulator and increase the cost. In addition, it should be known that the strong light absorption of graphene will be the disadvantage in the phase modulator as it can decrease the transmittance of the modulator.

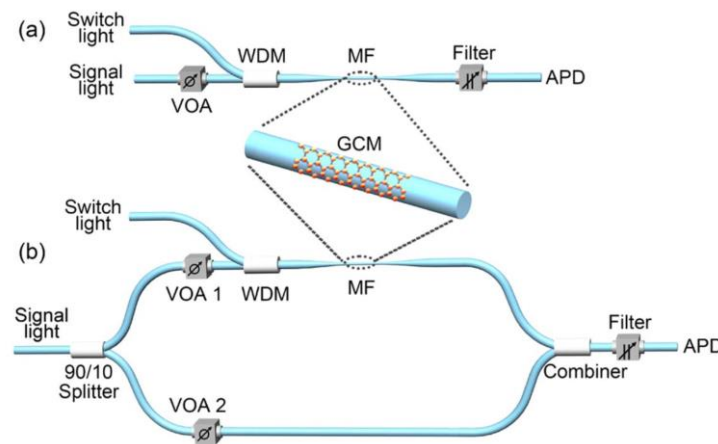


Figure 1.6: The schematic diagram of optical Kerr effect phase modulator based on (a) optical amplitude modulation in a GCM, and (b) optical phase modulation in a GCM in one arm of an all-fiber MZI. VOA, variable optical attenuator; WDM, wavelength division multiplexing; MF, microfiber; APD, avalanche photodetector. The data are adapted from [20].

The third modulator is the optical thermal effect modulator which is based on the excellent photothermal effect and thermal conductivity of graphene [21]. The large thermal energy will be generated when light with high energy density acts on graphene. It can easily transfer the thermal energy to the substrate (e.g., fiber or waveguide) and raise the refractive index of fiber (or waveguide) where light transmits in. And it will further result in the phase shift of signal light. As reported by the research group of Prof. Jianlin Zhao, a Mach-Zender

Interferometer is used in the optical thermal effect modulator and the structures are similar to that in the optical Kerr effect phase modulator, as shown in Figure 1.7. In this work, a 5-mm graphene-coated microfiber is used for thermal modulation and a phase change of more than 21π with the linear slope of $0.09 \pi/\text{mW}$ is obtained, which demonstrated an efficient all-optical switch. The optical thermal effect modulator has good optical transmittance and modulation depth because it can directly change the substrate's refractive index. However, the response time is quite large due to slow heat dispersion which restricts its application on the high-frequency device.

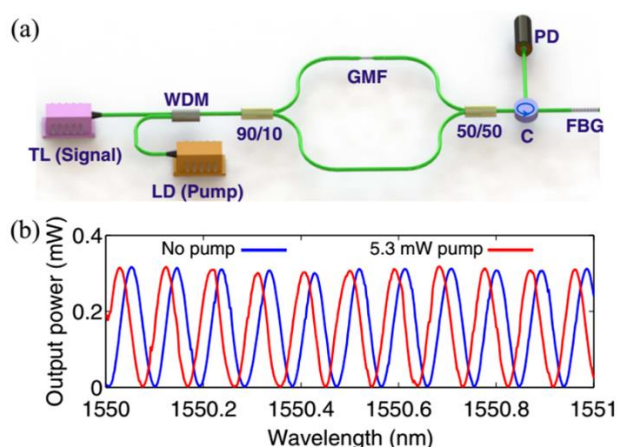


Figure 1.7: The schematic diagram of optical thermal effect modulator. (a) Schematic of the experimental setup for measuring the phase shift of light transmitting in graphene-coated microfiber, (b) measured interference patterns without (blue) and with (red) pumping laser. The data are adapted from [21].

The research on optical modulators based on graphene material is important for signal processing and optical communication system. Various all-optical modulators based on different mechanisms can be compatible with modern high-speed fiber communication networks and satisfy the urgent need for ultrafast signal processing.

1.3 Optical fibers used for sensing

Optical fiber was firstly designed for light transmission and image transmission in the

optical industry. The low-loss optical fiber was produced in the early 1970s, after that, optical fiber can be used in communication technology to transmit information over long distances. However, optical fibers can not only be used as the propagation medium of light waves but also be used for sensors. The characteristic parameters (amplitude, phase, polarization state, wavelength, etc.) of light waves propagating in optical fibers can be directly or indirectly influenced by external factors (such as temperature, pressure, magnetic field, electric field, displacement, rotation, concentration, material composition, etc.) so that the optical fiber can be used as the sensing element to detect various physical and chemical quantities and other parameters. This is the basic principle of fiber optic sensors. It should be noted that although the basic principle of optical fiber sensors is similar to that of photoelectric sensors, there are important differences. The main difference is that for optical fiber sensors, we need to consider the influence of various characteristics of optical fibers (including mechanics, optics, thermotics, acoustics, etc.) on the sensors. In addition, several new types of optical fiber sensors have been invented and experimentally demonstrated, such as distributed optical fiber sensors, optical fiber grating sensors, polymer optical fiber sensors, and photonic crystal optical fiber sensors, that provide unique sensing performances and extend the application scenarios.

Fiber sensors can be divided into two categories: functional type and light-transmitting type. The functional optical fiber sensor can realize the measurement and transmission of environmental parameters based on the influence of external physical factors on the characteristics (e.g., amplitude, phase, polarization state or wavelength) of the light transmitting in the optical fiber. This kind of fiber sensor enables the optical fiber to acquire and transmit information concurrently. For the light-transmitting fiber sensor, the fiber serves as the medium of data transmission. The sensing work and data acquisition are on the strength of other light-sensitive components. It is characterized by making full use of

the existing optical sensor, which is convenient for diverse applications. The optical fiber sensors can further be subdivided based on different sensing principles, such as amplitude modulation, phase modulation, polarization state modulation, wavelength modulation, etc.

1.3.1 The characteristics of fiber optic sensors

Compared with traditional sensors, the main features of fiber optic sensors are excellent performance, the wide range of objects, compatibility, ease to form a network, and low cost.

(1) Anti-electromagnetic interference, electrical insulation, corrosion resistance, and intrinsic safety. The optical sensor, which uses light waves to transmit information is an electrically insulating, corrosion-resistant transmission medium. Thus, it is insensitive to strong electromagnetic interference and can keep safe and reliable under the external electromagnetic field. This also makes fiber sensors convenient and effective for sensing in various application scenarios, such as large-scale electromechanical, petrochemical, metallurgical, flammable, explosive, and strong corrosive environments.

(2) The use of optical interference technology makes the sensitivity of many optical fiber sensors better than ordinary sensors. Some of them have been demonstrated theoretically and experimentally. For example, fiber sensors presented excellent performances on the measurement of many physical quantities including rotation angle, underwater sound, acceleration, radiation, temperature, and magnetic field.

(3) Small size, light weight and variable shapes. In addition to the characteristics of light weight and small size, the optical fiber also has the advantage of flexibility. The optical fiber can be made into various devices with different shapes and sizes which makes them conducive to aerospace and narrow space applications

(4) Optical fiber has specific applications in distributed sensing which is currently

irreplaceable in the sensor fields. Optical fiber distributed sensors can perform the distributed measurement in a large spatial range (tens of meters to hundreds of kilometers).

(5) Optical fiber sensors have currently been applied for the measurement of multiple physical and chemical parameters, such as temperature, pressure, displacement, speed, acceleration, liquid level, flow, vibration, underwater sound, current, electric field, magnetic field, voltage, impurity content, liquid concentration, nuclear radiation, etc.

(6) The fiber sensor has little influence on the measured medium, which is extremely beneficial for applications in the medical and biological fields.

(7) Fiber sensor is easy for multiple parameters multiplexing which is beneficial to facilitate multi-sensor networking and form a remote metering network with existing optical communication technology.

(8) The cost of many types of optical fiber sensors is much lower than the existing similar sensors.

1.3.2 The sensing principles of fiber sensors

Generally, three main physical dimensions are utilized on fiber sensing: wavelength, amplitude and polarization. The wavelength sensing can be used on fiber interferometer by detecting the interference dip shifting induced by the surrounding environment. Amplitude sensing is widely used on diverse fiber structures such as side-polished fiber, curved fiber, tapered fiber and core offset fiber. The structured optical fiber is sensitive to the refractive index (RI) of surrounding materials and the mismatched RI will give rise to varying degrees of loss and further induce the intensity change of output light. Polarization sensing is generally used on side-polished fiber assisted with metal or 2D materials. The coated materials can lead to the alteration of light polarization due to atomic resonance absorption.

(1) The fiber sensor based on amplitude modulation

The light transmitting in the fiber can be influenced by the external environment. By detecting the amplitude alteration, the environmental parameters can be demodulated. There are several ways to change the light intensity in the optical fiber: change the micro-bending state of the optical fiber; change the coupling condition of the optical fiber; change the absorption of light waves by the optical fiber and change the refractive index distribution in the optical fiber. We will take the microbend sensor as an example.

The microbend fiber sensor can be used to detect the change of external parameters by measuring the microbending loss in the optical fiber. In detail, when the multimode fiber is bent, part of the core mode energy will be converted into the cladding mode energy. By monitoring the energy change of core mode or cladding mode, the environmental parameters, such as displacement or vibration, can be demodulated. As can be seen from Figure 1.8, the laser emitted from the light source is transmitted and coupled into the multimode fiber. The unguided mode can be removed by the filter and the deformer is used to give rise to fiber bending. When the bending degree of fiber is tuned, the energy converted into the cladding mode also changes. After that, the optical signals can be collected by the PD and transferred to electrical signals. The PD is connected and controlled by the PC which can be used for data analysis. It should be noted that the sensitivity of the microbending sensor is determined by the mode distribution of the multimode fiber. As the high-order modes are easier to be transformed into cladding modes, more high-order modes will bring higher sensitivity,



Figure 1.8. The schematic diagram of microbend fiber sensor

The microbend fiber sensor has a relatively simple structure and the used optical components (e.g., fibers, PD, laser) are easy to obtain which will be beneficial for its practical application. For example, a fiber alarm has been developed based on microbend fiber sensor. The basic structure is that the optical fiber is curved and woven in the carpet. When a person stands on the carpet, the bending state of the optical fiber increases which will further result in the change of light intensity through the optical fiber. The key to the development of this type of sensor is to determine the best structure of the deformer.

(2) The fiber sensor based on phase modulation

Sensors that use the phase change of light waves to detect various parameters are called phase-modulation fiber sensors. There are many unique advantages of phase-modulation sensors compared to amplitude-modulation sensors because of different sensing principles. The main features of this type of optical fiber sensor are shown below.

■ High sensitivity

The fiber interferometer can be much more sensitive than ordinary optical interferometers due to the use of optical fibers with lengths of several meters or even hundreds of meters or more.

■ Flexible and diverse

Since the sensing part is the fiber itself, the geometry of the probe can be designed in different forms according to the requirements.

■ Wide range of application

The optical path of the fiber interferometer can easily be influenced by various parameters which conversely means that the fiber interferometer reveals its capacity for extensive applications. At present, plenty of types of optical fiber interferometers have been developed to measure various parameters, such as pressure, temperature, acceleration, current, magnetic field, liquid composition and refractive index, etc. Moreover, one fiber

interferometer can also be used for sensing multiple parameters. In Chapter 4 and Chapter 5, we propose the RCF-based MZI that can be applied for simultaneous measurement of temperature and RI (curvature).

■ Special requirements for optical fiber

In the fiber interferometer, the light of the same mode should be superimposed in order to obtain the interference effect. Thus, the performance of the single-mode fiber is much better than that of the multimode fiber. Indeed, the interference pattern can also be obtained by using multimode fiber, but the performance is greatly reduced and the signals are more difficult to be detected.

To achieve the desired interference effect, the vibration directions of the two coherent lights must be the same. Therefore, the "high birefringence" single-mode fiber is preferred in various fiber interferometers to reduce errors caused by polarization changes. Studies have shown that the material of the optical fiber, especially the material of the sheath and outer coating, has a great influence on the sensitivity of the fiber interferometer. Therefore, to meet the requirements of measuring different physical parameters, the applied fiber needs to be specially processed.

1.3.3 Various physical structures of fiber interferometers

According to the principles of traditional optical interferometers, Mach-Zehnder fiber interferometer, Michelson fiber interferometer, Sagnac fiber interferometer, Fabry-Pérot fiber interferometer have been developed. All of them have been widely investigated and practically applied in the sensing field. The detailed configurations and principles of the mentioned four kinds of interferometers are introduced below.

■ **Mach-Zehnder Interferometer (MZI)**

The schematic diagram of the M-Z fiber interferometer is displayed in Figure 1.9. The coherent light emitted from the laser source is respectively sent to two single-mode fibers (the two arms of the M-Z fiber interferometer) of basically the same length, one of which is the sensing arm and the other is the reference arm. The splitting and combining of the laser are realized by two fiber directional couplers. The superposition of the two laser beams output from the two optical fibers will produce interference effects. The all-fiber interferometer has the strong anti-interference ability.

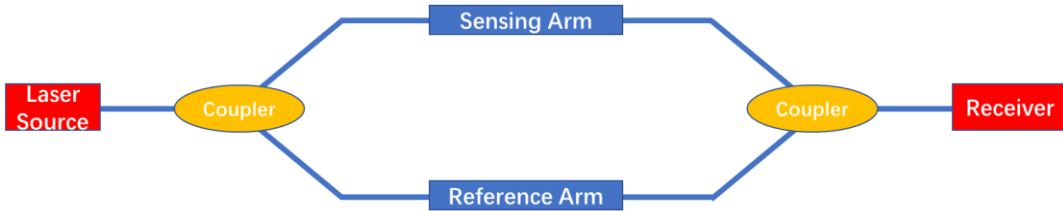


Figure 1.9. The schematic diagram of MZI

According to the principle of double-beam interference, the interference intensity of output light can be expressed as

$$I = I_1 + I_2 + 2 \cdot \sqrt{I_1 \cdot I_2} \cos \left[\frac{2\pi}{\lambda} \cdot n \cdot (L_1 - L_2) \right] \quad (1.17)$$

when the phase $\delta=2m\pi$, it is the maximum value of the interference field; when the phase $\delta=(2m+1)\pi$, it is the minimum value of the interference field, where m is the order of interference. Thus, wavelengths of the interference dips can be calculated by equations below

$$2\pi \cdot n \cdot (L_1 - L_2) / \lambda = (2m + 1)\pi \quad (1.18)$$

$$\lambda = \frac{2n\Delta L}{2m+1} \quad (1.19)$$

External factors can directly induce the change of the length (corresponding to the

elastic deformation of the fiber) and the refractive index n (corresponding to the elasto-optical effect of the fiber) of the sensing arm in the fiber interferometer. Therefore, when the relative optical path difference $n\Delta L$ is altered caused by external factors (it could also be the changes of light frequency or light wavelength), the shape of the interference fringe will change accordingly. Therefore, the environmental parameters, such as temperature, strain, vibration, etc., can be detected by monitoring the variation of the interference patterns.

■ Michelson fiber Interferometer

Figure 1.10 shows the schematic diagram of the Michelson fiber interferometer. A 2×2 fiber directional coupler is used for laser coupling-in and coupling-out. The end faces of two fibers are coated with high-reflectivity films to form a Michelson fiber interferometer. One of them is used as a reference arm, and the other is used as a sensing arm. The sensing principles of Michelson fiber interferometer are similar to that of MZI.

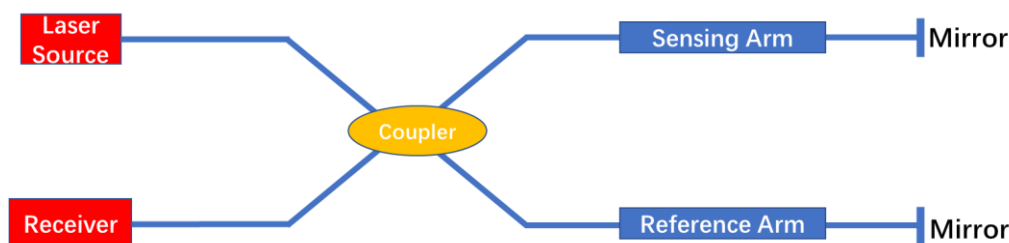


Figure 1.10. The schematic diagram of Michelson fiber interferometer

■ Sagnac Fiber Interferometer

Sagnac fiber interferometer is composed of a fiber loop formed by one single fiber. As can be seen from Figure 1.11, the schematic diagram of the Sagnac fiber interferometer is displayed. Two beams of light traveling in opposite directions are coupled in the fiber from two fiber ends. The laser emitted from the light source will be divided into two parts through coupler 1. One of the two light beams is introduced in optical circulator 1, transmitting through the fiber loop and collected by optical circulator 2. The other of the

two light beams is coupled in optical circulator 2 and then collected by optical circulator 1. Afterward, the two beams of the collected light will be superimposed to produce the interference effect, and the intensity of the interference light is detected by the receiver.

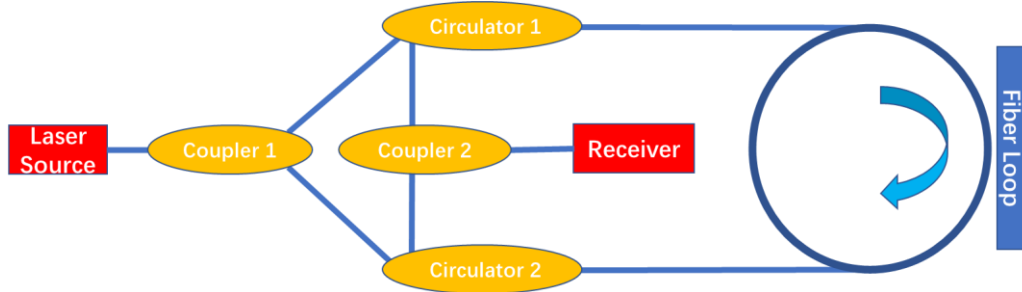


Figure 1.11. The schematic diagram of Sagnac fiber interferometer

The sensing principle of the Sagnac fiber interferometer is that the two light beams will show different phase shifts under the influence of the external environment and the interference patterns will present corresponding changes. The most typical application of the Sagnac fiber interferometer is rotation sensing, which is well known as fiber gyroscope. Benefiting from its unique advantages, such as no moving parts and no nonlinear effect, Sagnac fiber interferometer can be used for rotation sensor with high performance and low cost.

When the circular optical path has a rotation Ω , there will be an optical path difference between the two beams of light propagating in opposite directions

$$\Delta L = \frac{4A}{c} \cdot \Omega \quad (1.20)$$

where A means the area of the circular optical path, c is the light speed in vacuum.

When the circular optical path is composed of N-turn single-mode fiber, the phase difference between the two beams can be calculated by the equation below

$$\Delta \varphi = \frac{8\pi NA}{\lambda c} \cdot \Omega \quad (1.21)$$

where λ represents the light wavelength in vacuum.

The advantages of the Sagnac fiber interferometer are shown below:

(1) High sensitivity. For fiber gyroscope, the detection sensitivity of phase shift can be enhanced by simply increasing the number of fiber turns to increase the area enclosed by the loop (the area changes from A to AN , N is the number of fiber turns). In the meantime, the size of the instrument will keep the same.

(2) No rotating part. The fiber gyroscope can be fixed on the rotating part under test which will greatly broaden the scope of practical applications.

(3) Small size.

■ Fabry-Pérot Interferometer (FPI)

The optical fiber Fabry-Pérot sensor is known as an F-P interferometer composed of optical fibers. At present, the fiber Fabry-Pérot cavity in this kind of interferometer mainly has three representative structures: intrinsic type, non-intrinsic type, and linear composite cavity. The intrinsic Fabry-Pérot cavity means that the cavity is composed of optical fibers, while the non-intrinsic type uses the air gap between the two fiber end faces (both ends coated with highly reflective coating) to form an air microcavity. Currently, the non-intrinsic F-P interferometer shows better performance and more extensive applications.

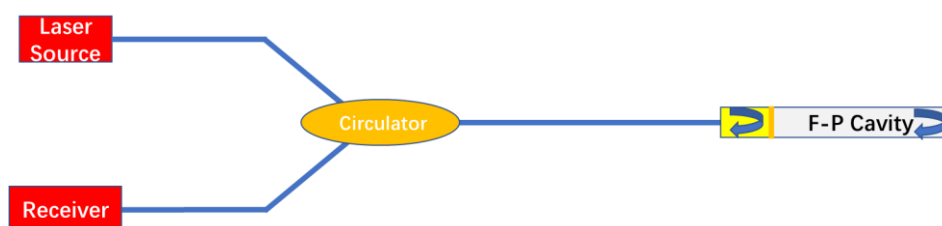


Figure 1.12. The schematic diagram of FPI

The schematic diagram of the Fabry-Pérot interferometer is shown in Figure 1.12. The laser is introduced to the F-P cavity through an optical circulator. The coherent light beam will be reflected on the two ends of the microcavity and return along the incident path. Then the two beams of reflected light meet and interfere to generate the output signals which are collected by the PD on the receiving end. The interference intensity is related to the length

of the microcavity. When external parameters (such as force, deformation, displacement, temperature, voltage, current, magnetic field, etc.) act on the F-P microcavity, the cavity length will change which will further give rise to the variation of the interference intensity of output signals. According to this principle, the length of the microcavity and the change of external environmental parameters can be derived from the variation of the interference signal so that the sensing of various parameters can be realized. For example, the Fabry-Pérot interferometer can be directly fixed on the sensing object. The slight deformation of the object will result in the length change of the Fabry-Pérot cavity and further induce the change of output lights. It should be noted that the deformation of an object could be induced by strain, stress, pressure, vibration, etc., which means that the F-P interferometer is capable of sensing on multiple parameters. In addition, the application of the F-P interferometer can be extended by combining it with functional materials. For instance, Fabry-Pérot cavity can be integrated with thermal expansion material for temperature sensing. The materials with good linearity of thermal expansion coefficient will enable the cavity length to change accompanied by the expansion (or contraction) of the thermally sensitive material to form the fiber Fabry-Pérot temperature sensor. In addition, as we know, fiber itself is magnetically insensitive which means that the fiber sensor is hard to be used for magnetic sensing. However, by combining the F-P interferometer with magnetostrictive materials, the fiber sensing of the magnetic field can be realized. It's also the same that Fabry-Pérot cavity can be applied as voltage sensor assisted with electrostrictive materials.

In the optical fiber Fabry-Pérot sensor system, the Fabry-Pérot cavity is the key component used as the sensing unit to obtain the information of measured parameters. In order to achieve the sensing of multiple parameters and different sensing characteristics, the Fabry-Pérot cavity can be fabricated with different structures. In addition, the signals obtained by the Fabry-Pérot sensor must be processed and demodulated to get the expected

results. The demodulation methods of Fabry-Pérot sensors mainly include intensity demodulation and phase demodulation. Among them, phase demodulation could be more difficult but with more advantages that make it the most widely used demodulation method.

We suggest that the reflectivity is R , the wavelength and intensity of incident light are λ and I_0 , then we can get the intensity of reflected light I_R and transmission light I_T :

$$I_R = \frac{2R(1-\cos \Phi)}{1+R^2-2R \cos \Phi} I_0 \quad (1.22)$$

$$I_T = \frac{(1-R)^2}{1+R^2-2R \cos \Phi} I_0 \quad (1.23)$$

where Φ is the light phase which can be calculated by the equation below

$$\Phi = \frac{4\pi}{\lambda} n_0 L \quad (1.24)$$

where n_0 represents the refractive index of the F-P cavity.

From the above equations, we can easily find that the output signals of the Fabry-Pérot interferometer can be influenced by reflectivity, the refractive index of the F-P cavity and cavity length. Thus, by using different sensor parameters and sensing principles, the Fabry-Pérot interferometer can be applied to broaden scope of sensing fields with diverse experimental setups and implementations.

1.4 Research objectives

The objectives of the research presented in this thesis are to develop the various applications of novel specialty fibers for optical communication and sensing devices, to enhance the communication and sensing performance of optical fibers with different novel configurations. More specifically, the thesis explores the following key research directions:

- Theoretically study the mechanism and experimentally demonstrate the prominent performance of light modulators assisted with graphene by using down-tapered SMF

- Develop a new fiber sensor with mismatched SMFs structure that can be applied for temperature and humidity sensing.
- Investigate and demonstrate an RCF-based sensor used for multiple parameters sensing, including temperature, RI and curvature.
- Propose and demonstrate a HCBF-based sensor used for human breath monitoring with temperature and curvature insensitivity.

1.5 Organization of the thesis

This thesis contains 7 chapters. Chapter 1 gives an overview of optical fiber, including fiber structure, fiber modes and fiber categories. Then the light modulators based on all-fiber structure assisted with 2D materials are introduced. After that, the fiber sensors with different structures and sensing principles are presented. Further, the research objectives and the thesis outlines are given. Finally, the publications during the period of the Ph.D. study are highlighted.

In chapter 2, an all-fiber modulator is experimentally demonstrated based on tapered SMF assisted with graphene nanoflakes.

In chapters 3 to 6, different novel structures are proposed which can be applied for fiber sensors, including the sensor of temperature, humidity, RI, curvature and human breath monitoring.

In the end, chapter 7 gives the conclusions of the works presented in this thesis and suggests possible future works of the research area.

1.6 Publications

A number of publications arose during the doctoral study period and most of which contribute to this thesis. My research publications are listed below.

Journal articles

- [1] **W. Yuan**, Q. Zhao, L. Li, Y. Wang, and C. Yu, "Simultaneous measurement of temperature and curvature using ring-core fiber-based Mach-Zehnder interferometer," *Optics Express*, vol. 29, no. 12, pp. 17915-17925, 2021,
- [2] **W. Yuan**, L. Li, Y. Wang, Z. Lian, D. Chen, C. Yu, and C. Lu, "Temperature and curvature insensitive all-fiber sensor used for human breath monitoring," *Optics Express* vol. 29, no. 17, pp. 26375-26384, 2021,
- [3] **W. Yuan** and C. Yu, "Dual Demodulation of Temperature and Refractive Index Using Ring Core Fiber Based Mach-Zehnder Interferometer," *Micromachines (Basel)*, vol. 12, no. 3, 2021,
- [4] **W. Yuan**, H. Qian, Y. Liu, Z. Wang, and C. Yu, "Highly Sensitive Temperature and Humidity Sensor Based on Carbon Nanotube-Assisted Mismatched Single-Mode Fiber Structure," *Micromachines (Basel)*, vol. 10, no. 8, 2019,
- [5] Y. Wang, J. Tao, **W. Yuan**, Z. Lian, Q. Ling, D. Chen, Z. Yu, and C. Lu, "Hollow Core Bragg Fiber Integrated with Regenerate Fiber Bragg Grating for Simultaneous High Temperature and Gas Pressure Sensing," *Journal of Lightwave Technology*, 39-17, 2021.
- [6] Z. Yang, **W. Yuan**, C. Yu, "Hollow Core Bragg Fiber-Based Sensor for Simultaneous Measurement of Curvature and Temperature," *Sensors*, 21 (23), 7956, 2021.

Conference papers

- [1] **W. Yuan**, H. Qian, Y. Liu, Z. Wang, and C. Yu, “Highly Sensitive Temperature Sensor based on Carbon Nanotube-assisted Mismatching Single-mode Fiber Structure,” in the 9th International Multidisciplinary Conference on Optofluidics, 2019

2 All-Optical Light Modulator with Down-Tapered SMF Assisted with Graphene

In chapter 2, the light modulator with the down-tapered SMF structure assisted with graphene is introduced. In the beginning, the overview of light modulators and graphene material is presented. Then, the experimental setups, including femtosecond laser, fiber tapering machine and optical paths, are introduced briefly. After that, the performances of the proposed and successfully fabricated light modulator are displayed, and the analysis of experimental results is included.

2.1 Overview of light modulators

Internet traffic is growing at a phenomenal rate over the years which is mainly driven by broadband services such as cloud computing and multimedia application. Optical communication system serves as the backbone of the modern Internet and provides ultra-wide bandwidth for data communication. Fiber is an indispensable transmission medium in optical communication systems because of its ultra-low loss. However, the loss of optical communication systems is large because the main functional components, such as lasers, modulators and photodetectors are still discrete components which gives rise to large coupling loss between these elements. Thus, if we can use fiber itself to realize all the functions which means that the fiber communication system can be integrated, the low loss and high-speed communication system can be built. Light modulators are key components in fiber optic communication systems. Various waveguide-based light modulators have been investigated and fabricated. Generally, in the fiber system, the communication light has to be coupled out to the modulators and then be coupled back to the fiber to realize signal modulation. Therefore, the demonstration of modulation function in the fiber itself will be a key point to achieve a high-speed all-fiber communication system. The modulation speed, modulation depth and optical transmittance are the key parameters of the light modulator. For a general electrical modulator, the light signal has to be coupled out and converted to the electrical signal. Then the modulated electrical signal is transformed to be optical signal and coupled again into the optical communication system. This process results in a complex system and reduces the modulation frequency. Thus, the all-fiber modulator makes it possible for direct modulation of the light signal. The optical modulator can be easily integrated into an optical communication system without signal conversion

and guarantee high-frequency light modulation.

Recently, various 2D materials, such as graphene, black phosphorus (BP), transition metal dichalcogenides (TMD), have been extensively investigated because of their characteristic optical and electrical properties [14, 22, 23]. It has drawn people's attention for wide application in optical, electronic and optoelectronic fields. Compared to bulk materials, 2D materials have many advantages based on their unique and diverse electronic structures. First, 2D materials can have a wide spectral response from ultra-violet to infrared. The diverse energy band structures can allow photon absorption with different energy. Second, despite the ultra-thin physical structure of 2D materials which is of one atom or a few layers of atoms thickness, there can be strong nonlinearities when light interacts with the material. For example, a single layer of graphene can absorb 2.3% of optical power with the vertical incidence in a large spectral range. In addition, the surface of 2D materials generally is robust and passive which leads to the easy integration of 2D materials and other devices, such as Si waveguides. Finally, the optical properties of 2D materials can be easily tuned with electric gating, chemical doping, optical excitation, or physical structures [22]. For example, the optical bandgap of black phosphorus (BP) can be easily adjusted by changing its layers with the mechanical method: energy gap of BP is 1.73 eV in monolayer, 1.15 eV in bilayer, 0.83 eV in trilayer and 0.35 eV in the bulk [24].

Graphene has been widely investigated as a kind of typical 2D materials because of its unique electrical and optical properties [12, 25, 26]. Graphene consists of one layer of carbon atoms which means the thickness is only one atom. However, it can absorb 2.3% of vertically incident light from ultra-violet to infrared light on account of its strong nonlinearity effect [26]. The electrical conductivity and thermal conductivity of graphene are excellent which makes sure its wide application in the electronic field. In addition, the surface of graphene is robust which gives rise to the easy integration with other materials

without lattice mismatching [12]. Due to its remarkable mechanical, electrical and optical properties, diverse optical modulators based on graphene have been investigated which can be categorized as intensity modulator and phase modulator. The intensity modulator generally is based on the light absorption with graphene. The output light intensity can be tuned by inducing the saturable absorption of graphene with optical excitation or electrical gating [17, 19, 27-33]. This structure can lead to a high-frequency optical modulation. However, the modulation depth and optical transmittance are relatively low which limits its application in reality [19]. The phase modulator can to some extent overcome the deficiencies of the intensity modulator by using Mach-Zehnder Interferometer. On the strength of the high non-linearity of graphene, the refractive index can be tuned by laser excitation or electrons injection [20, 31, 34-37]. And then it can transform the phase change to output intensity change. However, the usage of the Mach-Zehnder interferometer will result in a relatively complex structure. In this work, in order to realize the high-frequency, convenient optical modulation, the light modulator based on microfiber assisted with graphene has been researched and the fast, large-band and stable signal modulation is realized which satisfies the urgent need of high-frequency all-optical modulator.

2.2 The experimental setups

The tapered single-mode fiber assisted with graphene nanoflakes is studied for optical modulation research. As can be seen from Figure 2.1, the experimental setups are displayed for fiber tapering and light modulation. The femtosecond laser has the pulse width of ~ 500 fs and repetition frequency of 100 M with the center wavelength of 1580 nm. The continuous wave (CW) is generated by a tunable laser source with the wavelength of 1530 nm. The CW laser and femtosecond laser are coupled through a 50:50 coupler and

introduced into the tapered SMF which is coated with graphene nanoflakes. And then the output signals can go through a filter which is used to remove pumping laser energy and be received by a photodiode (PD). The PD can transfer the received optical signal to the electrical signal which can be displayed by the connected oscilloscope.

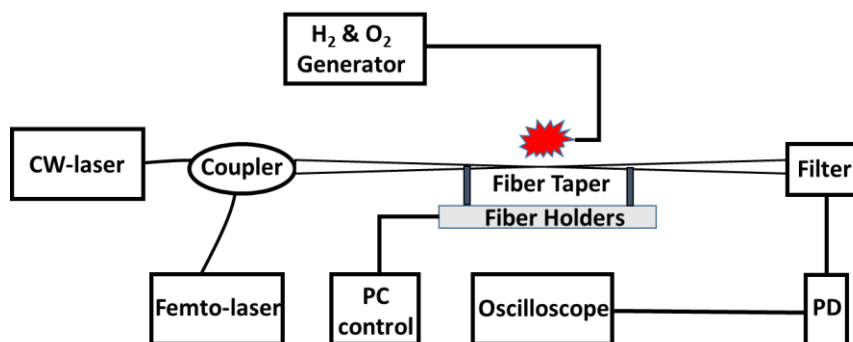


Figure 2.1. The experimental setups of the fiber tapering process and light modulation.

The fiber tapering can be realized by mechanical stretching under the circumstances of H₂ and O₂ heating. The thermal heating process will give rise to the melt of fiber structure and various fiber tapers can be achieved through mechanical stretching with different speeds. Firstly, the generator of H₂ and O₂ is turned on until the H₂ concentration reached a certain value (500 shown in the device). The H₂ and O₂ can be transferred to the fiber tapering machine through transporting pipeline for further utilization. The tapering machine is controlled by a personal computer (PC) which can regulate the parameters of the fiber tapering process, such as moving distance, moving speed, preheating time, etc. The tapering machine needs to be initialized before the start of the fiber tapering experiment to find the precise position of fiber holders. Then the single-mode fiber is pre-processed by removing the protection layer and then the processed fiber is located on the fiber holders of the fiber tapering machine. After the setting of tapering parameters on the PC, the fiber tapering process will be started. The heating tip will move towards the processed fiber and give the preheating around 5 s. Afterward, the two fiber holders will move slowly in opposite directions until reaching the setting position. The image of the fiber tapering machine (FTM)

is shown in Figure 2.2. From the user interface of the FTM software (shown in Figure 2.3), we can see that various parameters can be adjusted to control the shape of the produced fiber taper. Among these parameters, the preheating time, the moving speed and moving distance of the fiber holders (in red circles) are extremely important for shaping the tapered fiber. With repetitive trials and multiple tuning of the three parameters, the preheating time of 5 s, moving speed of 20 mm/min and the moving distance of 18 mm are selected to generate the fiber taper with proper diameter and cone shape.

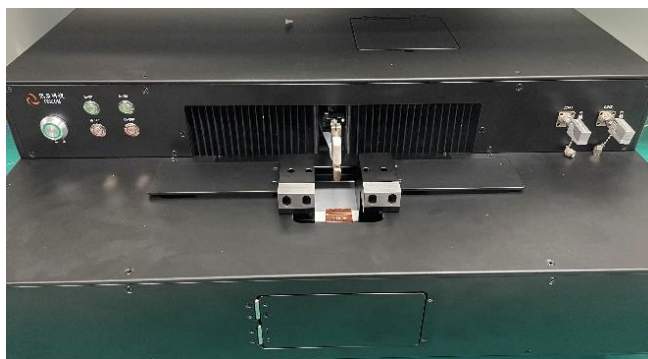


Figure 2.2. The image of the fiber tapering machine.

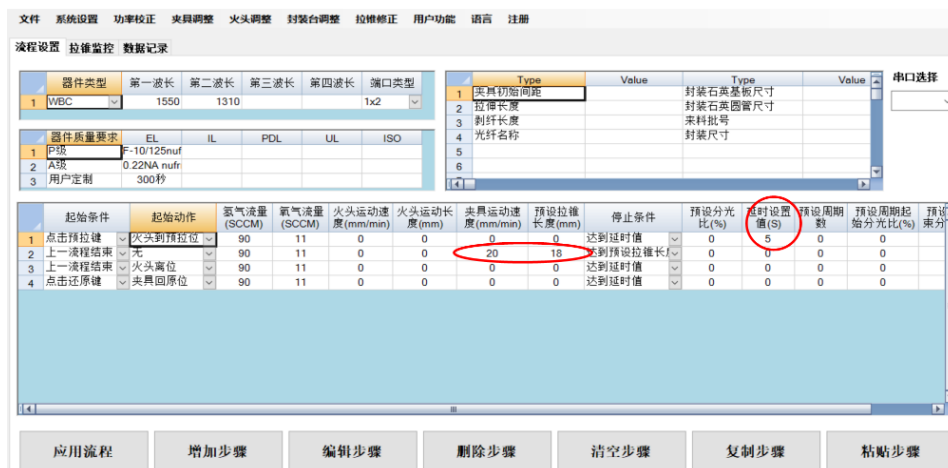


Figure 2.3. The user interface of the FTM software

The graphene nanoflakes are purchased from Yangtze Optical Fibre Company (YOFC). The diameter of the nanoflakes is around 5 μm and the average thickness is about 3 nm. The graphene nanoflakes are dispersed in ethanol and then the graphene solution is

processed by ultrasonic for 1 hour to disperse the nanoflakes as much as possible. After that, by using the drop-cast method, the graphene nanoflakes can be attached to the tapered fiber.

2.3 The experiment results and analysis

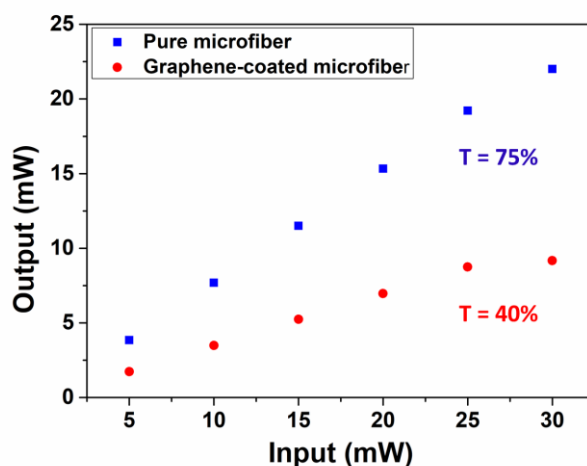


Figure 2.4. The relationship between input power and output power through the pure microfiber (blue points) and graphene-coated microfiber (red points).

The relationship between input power and output power through the pure microfiber (blue points) and graphene-coated microfiber (red points) is displayed in Figure 2.4. It can be found that with the increase of input power from 5 mW to 30 mW, the output power shows corresponding rising. The transmittance is measured to be around 75% before graphene coating and 40% after graphene coating. The difference can be attributed to the light absorption of graphene nanoflakes. It should be noted that with different tapering shapes of microfibers and graphene coating conditions, the light transmittance through the fiber taper will change accordingly. Based on our trials, the insert loss of the proposed light modulator can range from 4 dB to 20 dB. The transmission spectrum of the femtosecond laser is shown in Figure 2.5. The spectrum is recorded from 1500 nm to 1660 nm, and it

can be seen that the laser energy is mainly centralized in the range of 1540 nm to 1640 nm. Thus, based on the transmission spectrum, a filter of 1530 nm is utilized for filtering the femtosecond laser energy. In addition, the oscillogram of the femtosecond laser is also recorded which is shown in Figure 2.6. A strong signal peak can be found which is induced by the femtosecond laser pulse.

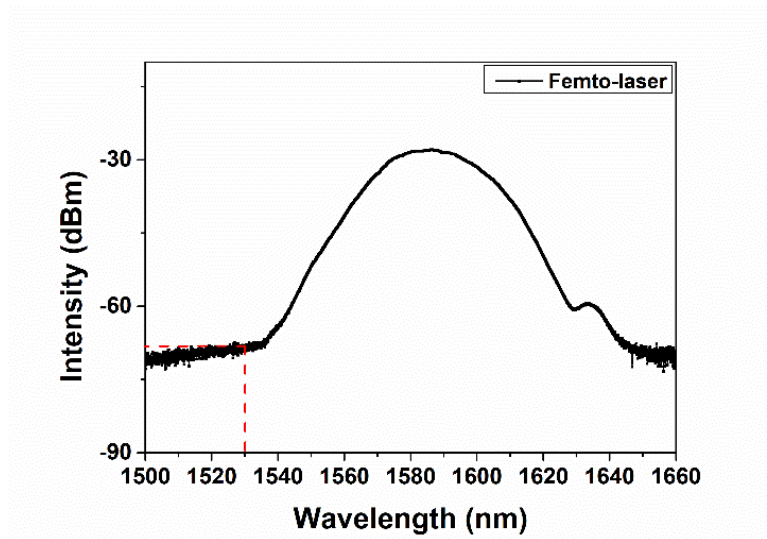


Figure 2.5. The transmission spectrum of femtosecond laser

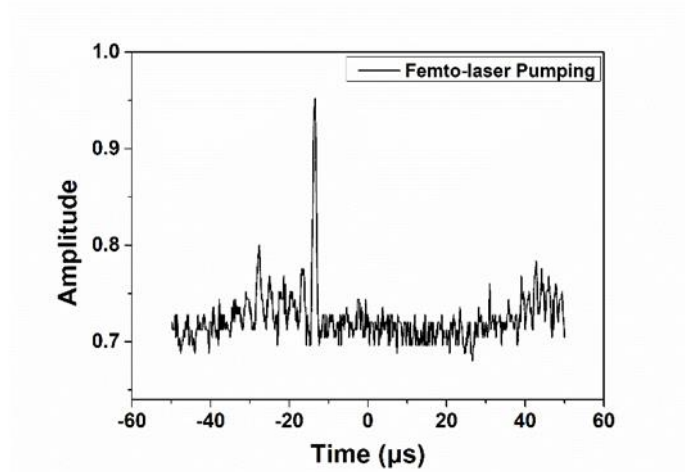


Figure 2.6. The oscillogram of the femtosecond laser used for pumping

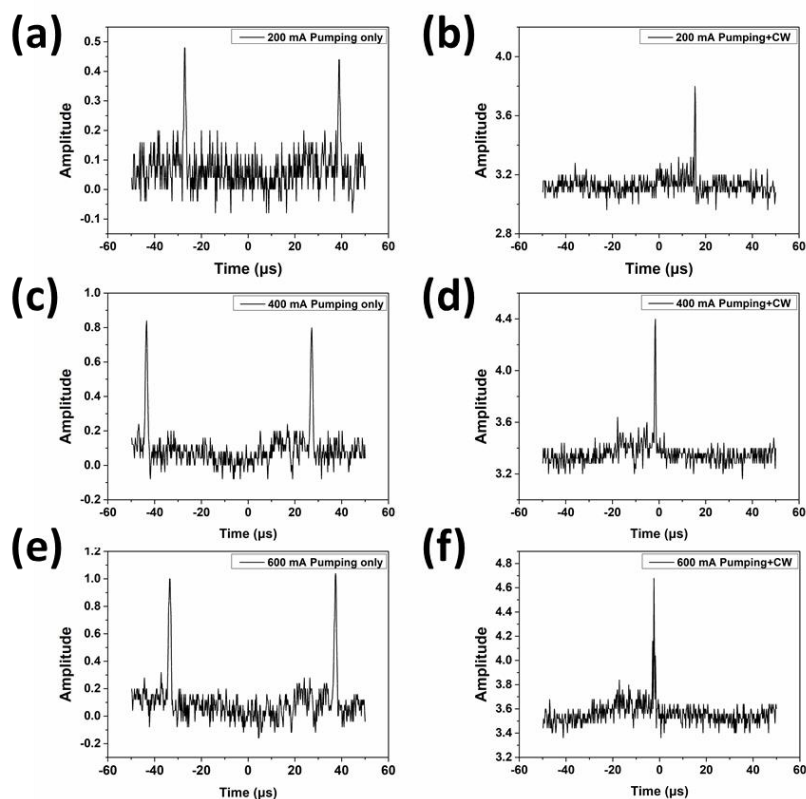


Figure 2.7. The oscillogram of the output signals with different input light of (a) 200 mA pumping laser only (b) 200 mA pumping laser and CW laser (c) 400 mA pumping laser only (d) 400 mA pumping laser and CW laser (e) 600 mA pumping laser only (f) 600 mA pumping laser and CW laser

As can be seen from Figure 2.7, we study the influence of input light on the output signals received from the oscilloscope. By tuning the amplifier current of femtosecond laser with values of 200 mA, 400 mA and 600 mA, the output light energy can reach 28.3 mW, 71.1 mW and 110.0 mW, respectively. Figure 2.7(a) presents the oscillogram with the input light of 200 mA pumping laser only. It can be found that the base energy is around 0.1 and the amplitude of the strong peak signal is around 0.5. The signal peak represents the laser pulse from the femtosecond laser and the base energy means the laser energy in the time interval between two femtosecond pulses. By comparing Figures 2.7(a), (c) and (e), it can be seen that the rising of pumping laser energy gives rise to a small change of the base energy, but only results in the enhancement of peak amplitude. In addition, from Figures 2.7(a) and (b), it is obvious that the introduction of CW laser has a great impact on the base

energy which is increased from 0.1 to 3.1. However, the amplitude of the peak signal shows a very slight change. This can also be demonstrated by experimental results shown in Figure 2.7(c), (d), (e) and (f). Thus, it can be concluded that the amplitude of peak signal can only be influenced by femtosecond laser and the base energy of the output signal completely depends on the CW laser.

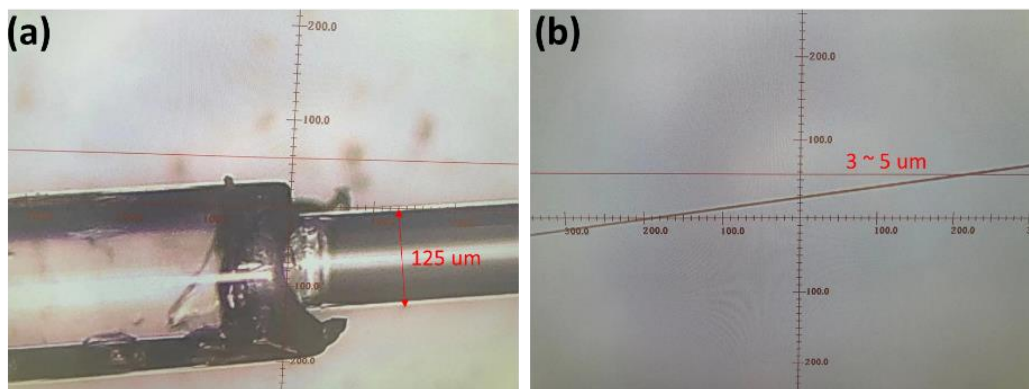


Figure 2.8. The microscope images of (a) normal fiber and (b) tapered fiber.

Figure 2.8 (a) and (b) give the microscope images of the fiber before and after the tapering process, respectively. For the normal SMF, the diameter is around 125 μm as shown in Figure 2.8(a). After the process of fiber tapering, the fiber diameter is decreased to about 3~5 μm . The energy density of light transmitting in the fiber can be immensely enlarged benefitting from the tapered fiber. And further, when the 2D materials are attached to such fiber structure, the interaction between transmitting light and materials will be strongly enhanced based on which the light modulation can be realized.

The optical filter is the indispensable optical component that is used to eliminate experimental errors by removing the pumping laser. As the bandwidth of the femtosecond laser is much wider than that of the CW laser applied in the experiment, the filtering of the femtosecond laser can be easily realized by choosing the proper bandpass filter. As can be seen from Figure 2.9, the bandpass filters of 1550 nm and 1530 nm are selected to compare both of the output signals. From Figure 2.9(a), it is distinct that the signal peak can be

observed which means that the 1550 nm filter cannot remove all of the pumping energy. However, when the 1530 nm filter is utilized shown in Figure 2.9(b), no obvious signal peak can be found, indicating that most of the pumping laser is successfully filtered from the output signals. Based on this, the transmitted signal emitted from CW laser source can be detected with slight disturbance of the femtosecond laser.

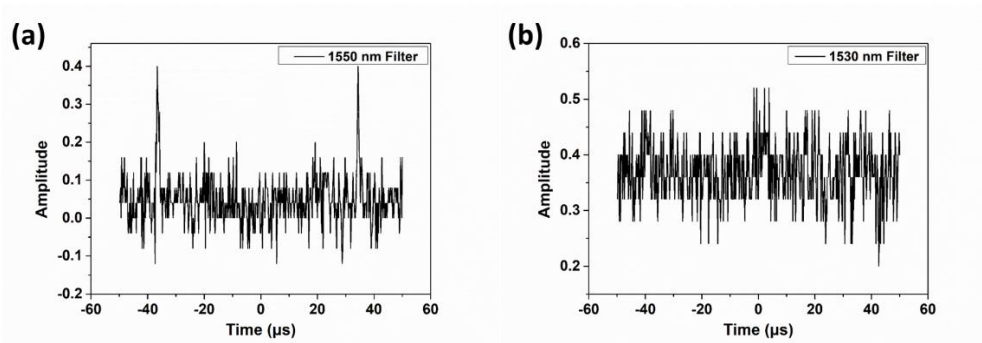


Figure 2.9. The oscillogram of femtosecond laser and continuous-wave laser with (a) 1550 nm filter and (b) 1530 nm filter

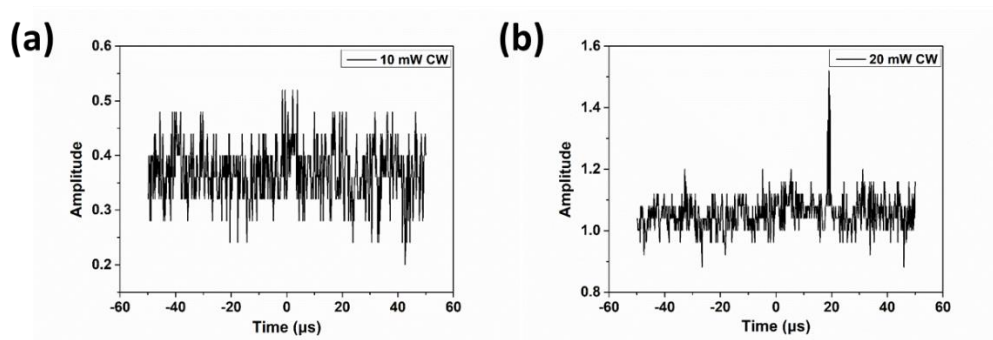


Figure 2.10. The oscillogram of femtosecond laser and CW laser with different CW laser energy of (a) 10 mW and (b) 20 mW

As can be seen from Figure 2.10, the oscillograms of the output signals with both femtosecond laser and CW laser are presented. The energy of the CW laser is set to be 10 mW and 20 mW, respectively. When the energy density of the introduced femtosecond laser is very high, the absorption spectrum of graphene will be significantly changed because of the sharp increase of excited carriers. Based on the principle of the Pauli blocking, limited photons can be further absorbed to induce the transition of carriers from ground state to

excited state which is known as saturable absorption. By inducing the saturable absorption of graphene, the capability of light absorption will be significantly influenced and thus the signal light can partly go through or be absorbed controlled by the status of graphene. From Figure 2.10(a), we can see that no obvious signal peak can be found which can be attributed to the light absorption of CW laser. The energy of the pumping laser cannot give rise to the completely saturated absorption of graphene nanoflakes, and thus the CW laser can still be absorbed. Further, when the energy of the CW laser is increased to 20 mW, a strong signal peak appears in the oscillogram shown in Figure 2.10(b). It is noted that the pumping energy is maintained the same only with the change of CW laser energy. As the experimental results shown in Figure 2.7, the larger energy of the CW laser will result in the rising of the base signal and the pumping laser will give rise to the signal peak occurring. Thus, the signal peak displayed in Figure 2.10(b) can be attributed to the femtosecond laser pumping. Benefitting from the saturable absorption effect of graphene, the femtosecond laser will pump the electrons from ground state to excited state so that part of the CW laser can transmit through the graphene-coated fiber taper and be collected by the PD at the receiving end.

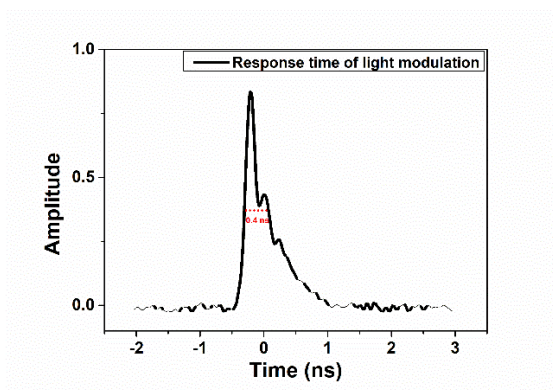


Figure 2.11. The response time of light modulation assisted with graphene nanoflakes

As shown in Figure 2.11, the single signal pulse of the light modulator is presented. The measured response time is up to 0.4 ns, indicating the potential for optical signal

processing with the bandwidth of up to 2.5 GHz. However, limited by our lab conditions, the experiments cannot be designed and conducted thoughtfully which we think needs to be further improved.

2.4 Conclusion

In this work, the light modulator with down-tapered SMFs structure assisted with graphene is proposed and demonstrated. The experimental setups and optical paths are built that consist of femtosecond laser, tunable laser, fiber tapering machine, PD, OSA and optical oscilloscope. The performances of the proposed and successfully fabricated light modulator are studied and improved, and the analysis of experimental results is included. The experimental results demonstrate a feasible method for all-optical light modulation with a down-tapered fiber structure assisted with graphene nanoflakes. The measured response time is up to 0.4 ns, indicating the potential for optical signal processing with the bandwidth of up to 2.5 GHz. The research will play a very important part in the optical communication system to simplify the optical components and realize all-fiber light modulation.

3 The Humidity and Temperature Sensor Constructed by Mismatched SMFs Assisted with CNT

This chapter is reproduced with some adaptations from the manuscript “W. Yuan, H. Qian, Y. Liu, Z. Wang, and C. Yu, “Highly Sensitive Temperature and Humidity Sensor Based on Carbon Nanotube-Assisted Mismatched Single-Mode Fiber Structure,” Micromachines (Basel) 10(2019).”

In this chapter, we report the fiber sensor used for the detection of temperature and humidity based on mismatched SMFs structure. The proposed all-fiber sensor exhibits stable temperature and humidity sensing performance. For a wide range of temperature sensing, from 40 to 100°C, the sensitivity is measured to be 0.24 dB/°C with the linearity of 0.99461. After the coating of CNT materials on the fiber surface, the temperature sensitivity presents a large enhancement from 0.24561 to 1.65282 dB/°C in a small region. In addition, the performance of humidity sensing is also studied. With the coating of CNT, the linearity of humidity sensing result shows a dramatic increase from 0.71731 to 0.92278 with the sensitivity of 25.71 pm/%RH.

3.1 Introduction

3.1.1 The importance of humidity sensor

The detection of environmental parameters, including physical and chemical changes, has become increasingly important for process control, security monitoring, and human protection. Temperature and humidity are the key parameters in these applications because of their great influence on food safety, manufacturing accuracy, and the service lives of precise instruments. Various methods have been used for temperature or humidity sensing, such as physical methods [38-42], chemical methods [43-46], and all-fiber devices [47, 48]. Among these techniques, the all-fiber structures have great advantages, such as compact size, easy fabrication, strong electromagnetic resistance, relatively low price, and ability for distributed sensing [49, 50]. On the strength of all-fiber configurations, diverse fiber sensors have been designed for various applications based on different mechanisms. Many fiber sensors have been reported, such as the Fiber Bragg Gratings sensor [51], long period fiber grating sensor [52], side polished fiber structure [53], hollow core fiber [54], single-mode–multimode–single-mode fiber structure [55], microcavity structure [56], Fabry–Perot fiber-optical sensor [57], up-tapered fiber [58], and mismatched fiber sensor [59, 60]. Among these fiber sensors, the optical interference mechanism is widely used due to its high sensitivity and easy fabrication [49]. Combined with other materials or electrical devices, the fiber interferometer can be extensively applied in diverse areas.

3.1.2 The introduction of CNT

Carbon nanotubes (CNTs), first discovered by Iijima in 1991, are known as one-dimensional nanostructures with sp^2 hybrid carbon atoms [1]. The structure of CNT can be treated as a seamless cylinder which is constituted of one or several graphene layers (known as single-wall or multiwall CNT) [61]. CNT material provides unique advantages in many areas, such as high electrical and thermal conductivity, chemical stability, strong

mechanical strength, and large surface-volume ratio [61, 62]. Benefitting from its good thermal, electrical, and optical performance, CNT plays a very important role in diverse fields, especially in sensing work. Many studies have been conducted for CNT-assisted sensors, such as strain sensors, gas sensors, humidity sensors, and temperature sensors [48, 63-67]. In this chapter, we report the sensing properties of temperature and humidity by combining CNT materials with structured fiber devices.

3.2 Experiments and simulation work

3.2.1 The fabrication of humidity sensor

The miniaturized optical fiber interferometer (MOFI) is successfully fabricated by using the mismatched SMFs structure. A commercial fusion splicing machine is utilized. The two SMFs are placed in the fusion device and spliced through manual operation. The offset of two SMFs is set to be 20 μm to make sure that the formed interferometer has a relatively large extinction ratio. The distance between two mismatched nodes is chosen as 2 cm. The multi-walled CNT are purchased from Xianfeng Nano. Company. The CNT is dispersed in ethanol solvent and then processed by ultrasonic. After that, the dispersed CNT-ethanol mixed liquor is attached to the surface of MOFI by the drop-casting method. In order to make sure CNT adhere to the fiber firmly, the fiber structure is located in a heating oven under 100 °C and then cooling down to RT. In this process, the CNT can be tightly attached to fiber surface due to van der Waals force.

3.2.2 The experimental design

To test the performance of the achieved mismatched fiber, and to explore the diverse potential applications based on light modulation by environmental change, the experiments and comparison between the bare mismatched fiber and the CNT-assisted mismatched fiber are conducted on temperature and humidity sensing. The range of the temperature is controlled between 40 and 125 °C at an interval of 5 °C. The relative humidity (RH) sensing

experiment is conducted by tuning RH between 45% and 95% at an interval of 10% at room temperature (24 °C). For each testing step of temperature and RH, an extra observation time of 25 min is guaranteed to make sure that the results are stable and reliable. A wideband laser device (1300–1650 nm) is utilized as the light source, and the optical spectrum analyzer is used for spectra capture. Figure 3.1(a) is the schematic diagram of the mismatched single-mode fiber. Figures 3.1(b) and (c) display the microscope image of the mismatched node and carbon nanotube coated part.

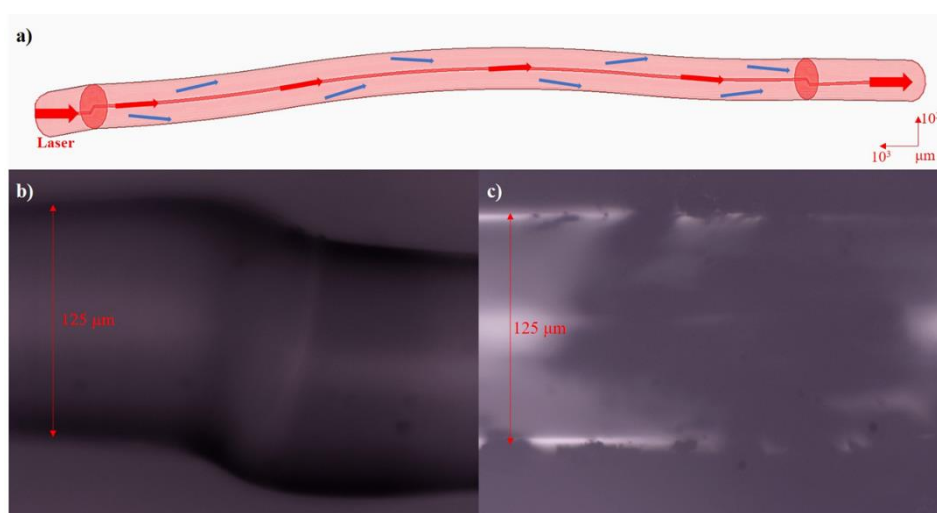


Figure 3.1. (a) The schematic diagram of the mismatched SMF, (b) the microscope images of the mismatched node and (c) the CNT coated part [68].

3.2.3 The simulation works

The simulation work of the mismatched fiber structure is conducted, and the results are shown in Figure 3.2. BeamPROP is applied as the simulation tool, and the index profile type is set as STEP. The refractive index of core and cladding are 1.4504 and 1.4447, respectively, which are the exact values of commercial single-mode fiber. The offset value of the two fibers is 20 μm , and the distance between the two mismatched nodes is 2 cm. The results show that the mismatched structure can successfully excite both core mode and cladding mode between the two mismatched nodes, which means that the MOFI has been achieved in one single fiber. As can be seen from Figure 3.2(a–c), the core mode and multi-cladding modes are excited at the first node, and then the interference takes effect at the

second node. The constructive or destructive interference determines the optical intensity of the output light. Then the fiber structure with a thick cladding is simulated to compare with the normal cladding modes, which is shown in Figure 3.2(d–f). It is found that the intensity of output light becomes very weak, which means that cladding modes dominate this mismatched structure. With the change of external environment, the phase and intensity of the cladding mode can be tuned, which further gives rise to the change of output light intensity. Thus, this mismatched fiber structure can easily be used as a temperature and humidity sensor because of the high sensitivity of cladding modes to the surrounding conditions. Due to the dominant cladding modes, the slight alteration of external parameters can be detected due to the optical modulation of cladding modes. The output signal will then be influenced because of the intensity change or phase alteration of cladding modes which will give rise to differently constructive or destructive interference.

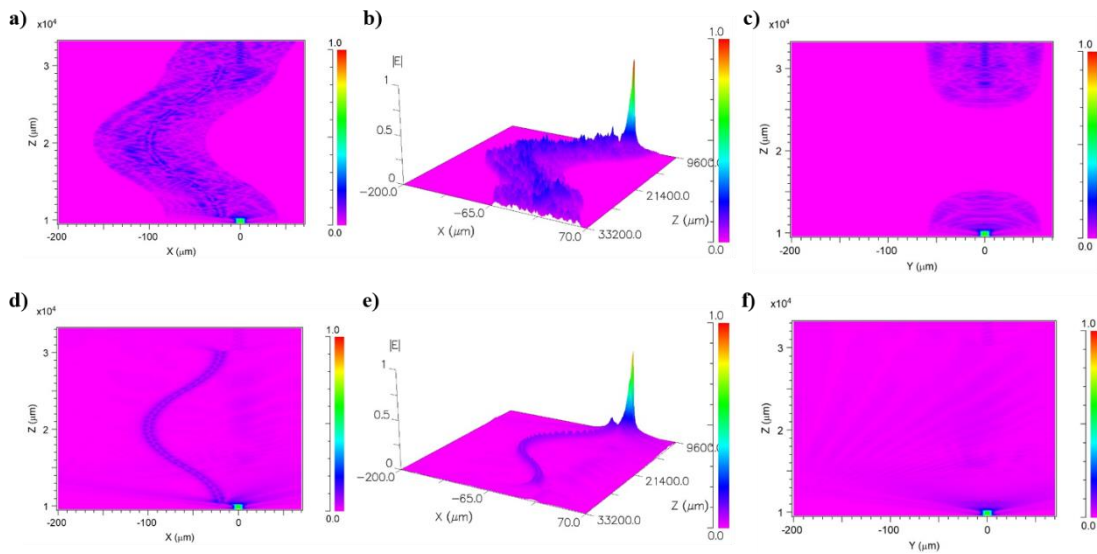


Figure 3.2. The Rsoft simulation results of the proposed sensor with (a–c) normal cladding and (d–f) thick cladding [68].

3.3 The sensing mechanism

Based on the MOFI structure, we can realize sensing performance through tuning light interference between the core mode and cladding modes which can be stably excited in the mismatched fiber structure.

Figure 3.3 elaborates on the interference dip shifting with the continuous temperature change from 40 to 125 °C. The dip shift can be attributed to the length change of the fiber structure and the effective refractive index (RI) change of core and cladding areas which are caused by external thermal energy. The interference equation is shown below [69]:

$$I = I_{core} + \sum_k I_{cladding}^k + \sum_k 2 \cdot \sqrt{I_{core} \cdot I_{cladding}^k} \cos \left[\frac{2\pi}{\lambda} \cdot (n_{eff}^{core} - n_{eff}^{cladding,k}) \cdot L \right] \quad (3.1)$$

I , I_{core} , $I_{cladding}^k$ mean the intensity of output light, core mode, and cladding modes. n_{eff}^{core} and $n_{eff}^{cladding,k}$ mean the effective RI of core mode and cladding modes. L is the interference length.

The destructive interference condition is shown in the following equations [69]:

$$2\pi \cdot (n_{eff}^{core} - n_{eff}^{cladding,k}) \cdot L/\lambda = (2m + 1)\pi \quad (3.2)$$

$$\lambda = \frac{2\Delta n_{eff}L}{2m+1} \quad (3.3)$$

Δn_{eff} means the difference of effective RI between core and cladding, and λ in Equation (3) means the wavelength of the interference dip. It is known that the effective RI of cladding has a relatively faster response to the temperature change compared to that of the core, which means that the RI of cladding will increase firstly while the RI of the core area will be unchanged at the start of temperature rising [70]. However, with time elapsing, the thermal energy around the fiber can finally give rise to the rising of the core's RI which can be larger than that of cladding's RI [70]. This means that the RI difference between core and cladding will firstly decrease because of the RI rising on cladding and the unchanged RI on the core. Moreover, it will then increase over a relatively long time in which the core's RI can also be influenced by temperature change. Thus, except for the interference length change (L in Equation (3.3)), the wavelength shifting can also be attributed to alteration of the RI difference between core mode and cladding modes. The interference intensity will also be influenced by energy redistribution of core mode and cladding modes which is induced by RI change of fiber core and cladding.

3.4 Experimental results and discussions

3.4.1 The performance of temperature sensing

Based on the observation in the experiment process, the fiber condition can be stabilized within 90 s following the external environment change, which means that the response time of temperature sensing can be estimated to be 90 s. The sensitivity is calculated to be 0.2165 nm/°C which is almost four times higher than 0.0575 nm/°C reported by Dong et al. [71]. It is also found that in certain small temperature ranges, the interference intensity displays stable variation with the temperature change. This makes it possible for temperature sensing simply using a power meter without the need of an optical spectral analyzer. The wavelength of 1593 nm is chosen for measuring the relationship between the temperature and transmittance intensity. As can be seen from Figure 3.4, the relationship between temperature and interference intensity displays good linearity with the sensitivity of around 0.24 dB/°C. The adjusted R-squared value reaches 0.99461 which demonstrates the good linearity between temperature and output optical intensity.

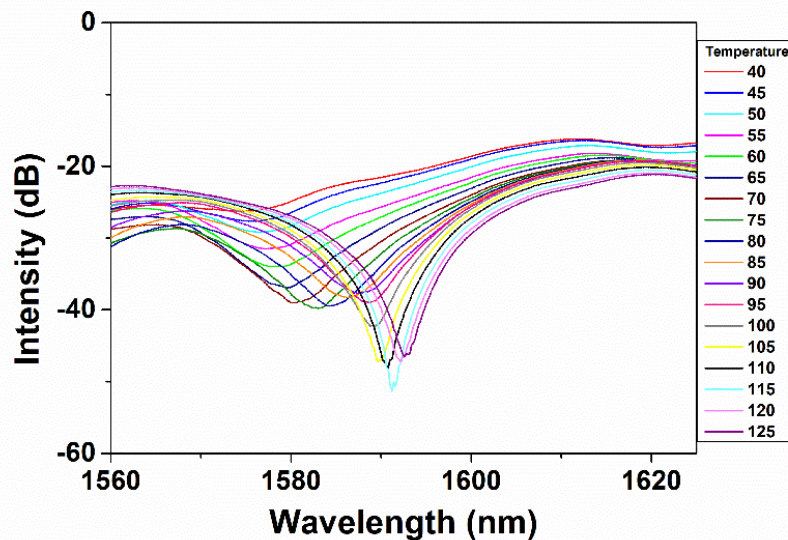


Figure 3.3. The relationship between the wavelength shift of the interference dip and the temperature variation from 40 to 125 °C with the step of 5 °C [68].

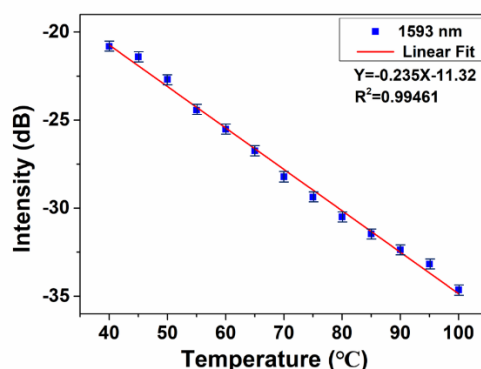


Figure 3.4. The relationship between the temperature and the intensity of interference dips at the wavelength of 1593 nm [68].

To increase the sensitivity of temperature sensing performance, the CNT material is utilized to alter the cladding modes modulation of the MOFI structure. As can be seen from Figures 3.5 (a) and (b), without CNT coating, the intensity shows a small shift with the temperature altering from 40 to 34 °C. The alteration can be attributed to the deformation of the mismatched node that results in energy redistribution between core and cladding. With decreasing temperature, the mismatched node will shrink which can induce more energy to be coupled into the core area. Based on the simulation result in Figure 3.2, the cladding mode's energy is dominant. This means that temperature change can result in relatively equal intensity between the core mode and cladding modes. The sensitivity increased dramatically when CNT material is attached to the fiber sensor. The enhancement can be attributed to the cladding mode modulation by CNT. The linear fitting results between temperature and intensity of interference dip are displayed in Figure 3.6. The blue line shows the change of transmittance intensity along with the alteration of temperature without CNT, and the red line indicates that CNT coating is present. It is obvious that the slope of the fitting line increases after CNT coating, which means that attaching CNT can achieve the enhancement of temperature sensing sensitivity. The sensitivity is enhanced from 0.24561 dB/°C without CNT to 1.65282 dB/°C with CNT, and this value is almost four times higher than the 0.437 dB/°C that was reported by Yin et al. [72]. The adjusted R-squared value also shows slight augmentation from 0.92636 to 0.9738, demonstrating stronger reliability of the sensing result.

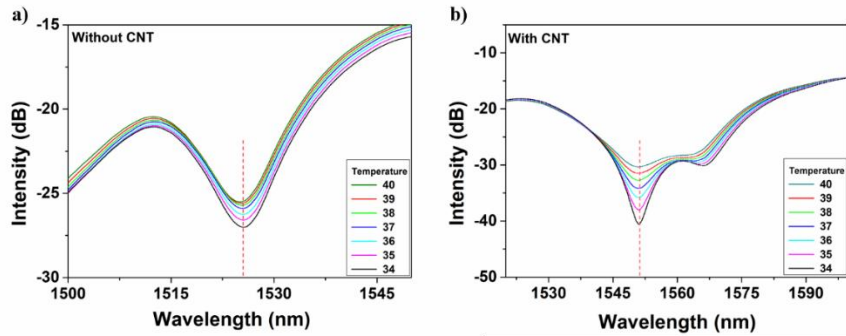


Figure 3.5. The spectra of temperature sensing (a) without and (b) with CNT coating [68].

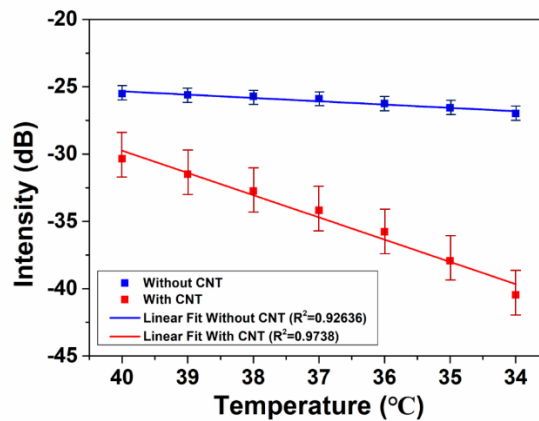


Figure 3.6. The relationship and linear fit between temperature variation and the intensity change of interference dips without (blue line) and with (red line) CNT coating [68].

3.4.2 The performance of humidity sensing

Based on cladding modes modulation, this mismatched fiber structure can also be used for humidity sensing, as shown in Figure 3.7. The experiment is conducted by changing RH from 45% to 95% at an interval of 10% at room temperature (24 °C). As we can see from Figure 3.7(a), with the increase of RH, the interference dip shows a redshift with the range of 5 nm. This can be attributed to the phase change of cladding modes induced by humidity alteration. The increasing humidity can lead to more sufficient contact between water molecules and the fiber surface which results in the effective RI change of cladding modes. As can be found from Equation (3.3), the change of Δn_{eff} will give rise to the interference dip shifting. Although the dip wavelength presents a relatively large shift of 5 nm following

the humidity changes, the result is not linear enough to show the difference from 45% to 95%. In order to increase the linearity between the wavelength shifting and humidity change, the drop-cast method was applied to attach the CNT onto the fiber structure between the two mismatched nodes. Benefiting from the tubular structure of CNT, the 1D material can absorb water molecules which will induce the RI change of CNT. The result is displayed in Figure 3.7(b). It shows that the relationship between humidity change and wavelength shifting becomes more linear. This can be explained that the RI change of CNT is smaller and more stable following the change of humidity which can further give rise to a more stable change of effective RI of cladding modes, and thus, the wavelength shifting displays good stability. Figure 3.8 gives the linear fitting results between the RH and wavelength shifting of interference dip. Without CNT attached (blue line), the adjusted R-squared value of the fitting line is only 0.71731, which means that the wavelength shifting cannot accurately present humidity change. This value is dramatically enhanced to 0.92278 after CNT coating is applied, as depicted by the red line in Figure 3.8. The fit result reveals that the CNT-assisted fiber sensor can strengthen the accuracy rating of humidity sensing. The CNT-assisted humidity sensor presents the sensitivity of 0.02571 nm/%RH, which is slightly higher than 0.0235 nm/%RH in the RH range 40–70% that was reported by Ma et al. [73]. In addition, when considering the continuous alteration of RH from 40% to 90%, the linearity of humidity response in our work is relatively enhanced compared to that of two pseudo linear regions, which indicates the more applicable and practical sensing performance of our sensor [73].

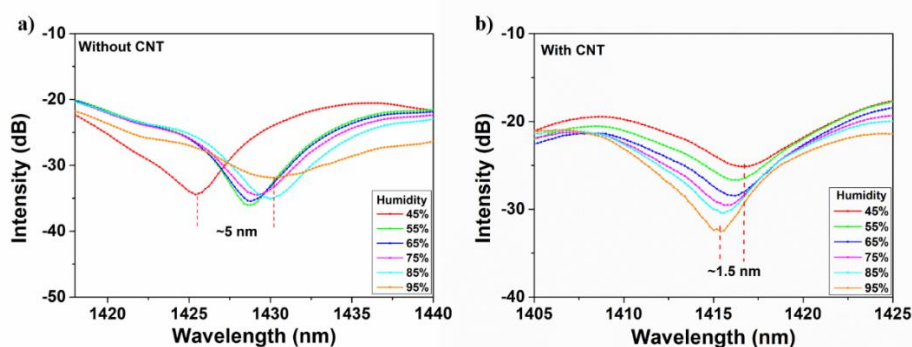


Figure 3.7. The spectra of relative humidity (RH) and interference wavelength (a) without and (b) with CNT attached [68].

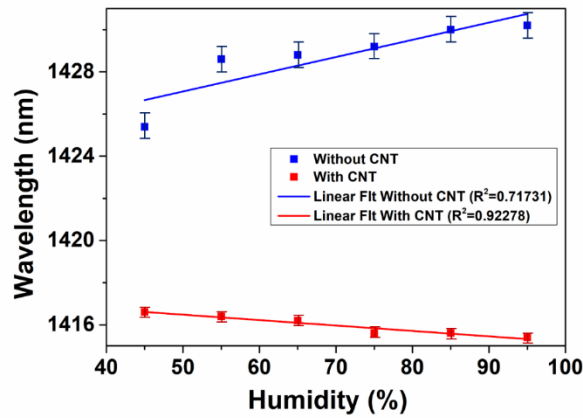


Figure 3.8. The relationship and linear fit between RH and interference dip wavelength without (blue line) and with (red line) CNT attached [68].

Based on the above results, it is manifested that both the core mode and cladding modes can be excited in the mismatched fiber structure. This structure shows good and stable sensing performance of temperature and humidity which is due to the modulation of cladding modes by the external environment. Due to the dominant cladding modes, the all-fiber sensor shows good sensing reliability and sensitivity.

3.5 Conclusion

In conclusion, an MZI sensor based on mismatched fiber structure is successfully created and simulated that demonstrates its application for sensing temperature and humidity based on cladding modes modulation. The sensing experiments are conducted with the structured fiber, and it displays good temperature and humidity sensing performance. With CNT attached to the fiber, the sensitivity of temperature detection in small ranges is enhanced from 0.24561 to 1.65282 dB/°C, and the humidity sensing becomes more reliable for real application. The combination of the manufactured MOFI structure and CNT achieves cost-effective, sensitive, and reliable sensing for both temperature and humidity.

4 The Fiber Sensor Based on RCF for Dual Demodulation of Temperature and RI

This chapter is reproduced with some adaptations from the manuscript “W. Yuan and C. Yu, “Dual Demodulation of Temperature and Refractive Index Using Ring Core Fiber Based Mach-Zehnder Interferometer,” Micromachines (Basel) 12(2021).”

In this chapter, an RCF-based fiber sensor is proposed and experimentally demonstrated that can be used for simultaneous measurement of temperature and RI. The proposed sensor is based on MZI structure, which is constructed by RCF, NCF and SMFs. The RCF is firstly fusion spliced with NCF to form the N-R fiber structure which is then sandwiched by two segments of SMFs. The maximum extinction ratio of the interference spectra reaches 27 dB with the free spectra range of 12 nm. The temperature sensitivity of the proposed sensor reaches 69 pm/°C and 0.051 dB/°C. The RI sensitivity is recorded as 182.07 dB/RIU and -31.44 nm/RIU with the sensing ranging from 1.33 to 1.38. It is noted that the interference is insensitive to temperature change which indicates that the RI value can be directly achieved by detecting the variation of dip intensity. And then, temperature sensing can also be realized by analyzing the wavelength shift of the interference dips.

4.1 Introduction

Optical fiber sensors have got widespread attention recently due to their low cost, easy manufacturing, small size, resistance to electromagnetic interference and chemical corrosion. Fiber optic sensors have been researched and developed in a variety of applications, such as the sensing of temperature [74-77], humidity [78-80], RI [81-83], strain [84-88], curvature [89-93], pH [94, 95], gas [96-100], and so on. Temperature and RI are considered important parameters because they both are of great significance in environmental monitoring, liquid quality testing and food safety testing. Researched different fiber structures, including fiber Bragg grating (FBG) [101], Mach-Zehnder interferometer (MZI) [70, 102, 103], Fabry-Pérot interferometer (FPI) [104, 105], side-polished fiber [106] and hybrid fiber structure [72, 102, 107] for simultaneous temperature measurement and refractive index. The MZI fiber optic sensor is considered to be one of the most effective structures. The temperature sensing principle of the MZI sensor is mainly based on the change of the effective RI difference and the interference length between the magnetic core and the cladding caused by the thermal effect. The effective RI difference and the change of the interference length will cause the wavelength shift of the interference spectrum, which can be used for temperature demodulation. RI sensing can be realized by exciting the evanescent field on the surface of the fiber, and the surrounding materials on the evanescent field have an effect on the fiber cladding mode. This will cause changes in the amplitude and phase of the light, leading to changes in the interference spectrum.

In this chapter, the ring core fiber (RCF) based MZI fiber sensor is proposed and experimentally demonstrated for dual demodulation of temperature and RI. The MZI sensor is fabricated by direct fusion splicing a piece of no core fiber (NCF) to a segment of RCF.

Then the formed N-R fiber structure is connected to two pieces of single-mode fibers (SMFs). The built SMF-NCF-RCF-SMF structure can be seemed as the miniaturized MZI. Multiple fiber modes are stimulated in the RCF and combined into the SMF. The experimental results demonstrate the good interference effect of the MZI structure with the maximum extinction ratio of 27 dB and the free spectra range of 12 nm. The temperature sensing is realized by monitoring the wavelength shift of interference dip induced by heating and cooling effect and the RI sensing can be implemented due to the adjustment of cladding modes' amplitude and phase induced by surrounding RI change. The RI value is expressed by the refractive index unit (RIU). The interference dip intensity and dip wavelength shift display different responses to temperature and RI changes which makes it possible for dual demodulation of these two parameters. The variation of temperature can result in the wavelength shift with the slope of 69 pm/°C and negligible change of dip intensity in limited temperature ranges. The alteration of RI values gives rise to simultaneous wavelength shift of -31.44 nm/RIU and dip intensity change of 182.07 dB/RIU. Thus, the RI can be demodulated by the change of interference intensity and temperature sensing can be achieved through the linear relationship between dip wavelength with the value of temperature and RI.

4.2 Experimental setups

The MZI is fabricated with four segments which consisted of double commercial single-mode fibers (SMF-28), no core fiber and ring core fiber. The NCF and RCF are purchased from YOFC and the diameters of SMF, NCF and RCF are the same at 125 μm which enables the direct fusion splicing without diameter mismatching. The lengths of applied NCF and RCF are 1mm and 20 mm, respectively. As can be seen from Figure 4.1(a), the cross-section

of RCF can be divided into three parts: fiber center (FC), ring core (RC) and cladding area. The radii of FC, RC and cladding are 5.45 μm , 9.35 μm and 62.5 μm , separately. Figure 4.1(b) displays the RI distribution along the fiber diameter (yellow dash line) and the RI of RC is 0.0134 larger than that of FC and cladding with the value of 1.44402.

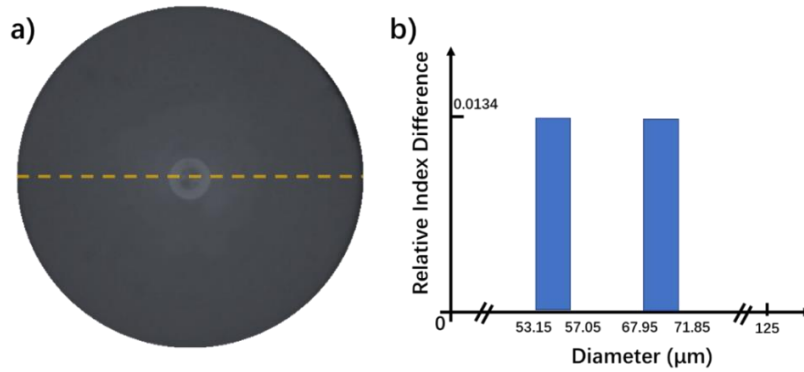


Figure 4.1. (a) The microscope images of RCF and (b) the RI distribution along the diameter (dash line) [108].

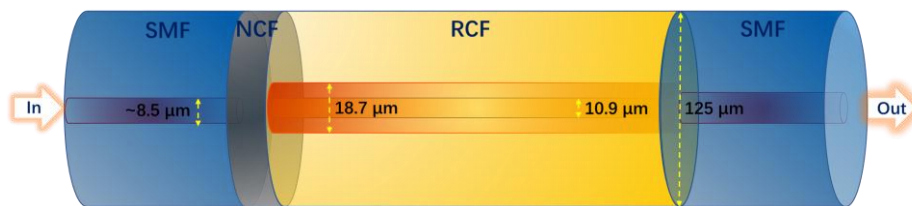


Figure 4.2. The schematic diagram of the MZI with the SMF-NCF-RCF-SMF structure [108].

Figure 4.2 depicts the schematic diagram of the MZI with the SMF-NCF-RCF-SMF structure. The blue parts show the SMFs with the diameter of 125 μm and core diameter of $\sim 8.5 \mu\text{m}$. The grey part represents the NCF with the diameter of 125 μm , which has the same RI value as that of SMF cladding. The yellow part depicts the RCF and the details are shown in Figure 4.1. The lengths of applied NCF and RCF are 1 mm and 20 mm, respectively. Broadband Source (BBS) with the bandwidth from 1470 nm to 1670 nm is used as the light source. The light transmitted in SMF will firstly be coupled into NCF and

then be transmitted to RCF in which multiple fiber modes will be excited including FC mode, RC mode and cladding modes. Different fiber modes will interfere and be coupled in SMF again at the splicing node of RCF and SMF. Generally, the miniaturized MZI structure can be formed in one single fiber to simplify the structure. By using mismatching, tapering or other specific methods, both core mode and cladding modes can be excited, and the core and cladding will serve as two paths of MZI. For ring core fiber, it can be physically divided into three parts. The ring core can be seemed as one path and the other parts can be seemed as the other path. That's why we claim it as the MZI structure. The MZI sensor is placed in the heating oven for temperature sensing and the liquids with different sugar concentrations are applied for RI sensing. The RI values of different liquids are measured and labeled using a commercial saccharimeter. The optical spectrum analyzer (OSA, YOKOGAWA, AQ6370D) with the measuring range of 600-1700 nm is utilized for spectra recording.

4.3 The sensing mechanism

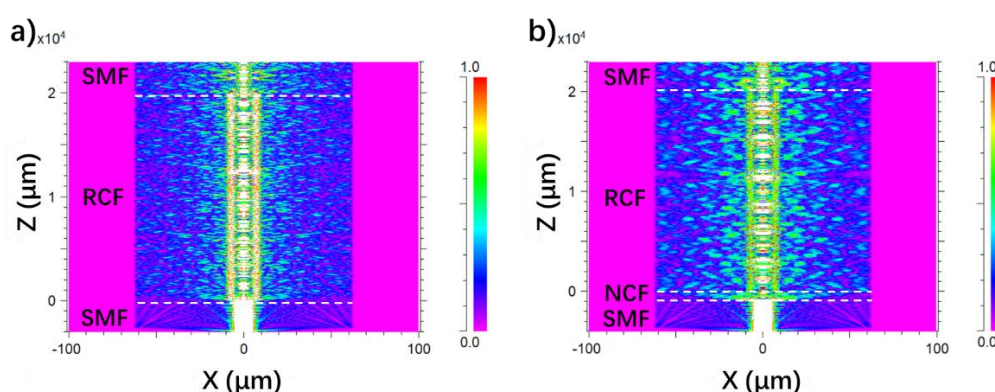


Figure 4.3. The Rsoft simulation results of (a) SMF-RCF-SMF structure and (b) SMF-NCF-RCF-SMF structure [108].

To study the effect of NCF on the MZI structure, the Rsoft simulation work is done

and the results are shown in Figure 4.3. The modeling of fiber structures with SMF-RCF-SMF and SMF-NCF-RCF-SMF is conducted with the simulation tool of BeamPROP. For SMF, the diameters of core and cladding are set to be $8.5\ \mu\text{m}$ and $125\ \mu\text{m}$ with the RI values of 1.4504 and 1.4447, respectively. The lengths of NCF and RCF are built as 1 mm and 20 mm. The RCF is modeled under the measurement results shown in Figure 4.1. The wavelength of 1550 nm is chosen as the free-space wavelength and the grid sizes on different axes of X, Y and Z are set to be $0.2\ \mu\text{m}$. Actually, we have done the simulation with different grid sizes and we find that the results are almost the same. If the grid size is set to be much smaller, the one-time simulation could be very expensive. For example, the one-time simulation would take more than 24 hours when $0.1\ \mu\text{m}$ is chosen as grid size. Considering both relatively precise grid size and simulation time consumption, we change and choose the grid size of $0.2\ \mu\text{m}$ in the X, Y and Z directions. As can be seen from Figure 4.3(a), the light is coupled from SMF to RCF and the mismatched interface between SMF and RCF gives rise to the energy redistribution which excites multiple modes in RCF including the FC mode, RC mode and cladding modes. The light energy is mainly coupled in FC mode and RC mode which induces the relatively weak cladding modes. By applying the NCF, as shown in Figure 4.3(b), the cladding modes are enhanced and RC mode becomes weaker which means that the NCF results in the redistribution of light energy among FC mode, RC mode and cladding modes. More cladding modes are excited in RCF which can significantly enhance RI sensitivity due to the strong interaction of cladding modes and surrounding materials. The Rsoft simulation results indicate that the MZI based on SMF-NCF-RCF-SMF can potentially serve as a preferable sensor structure on RI sensing compared to that based on SMF-RCF-SMF structure.

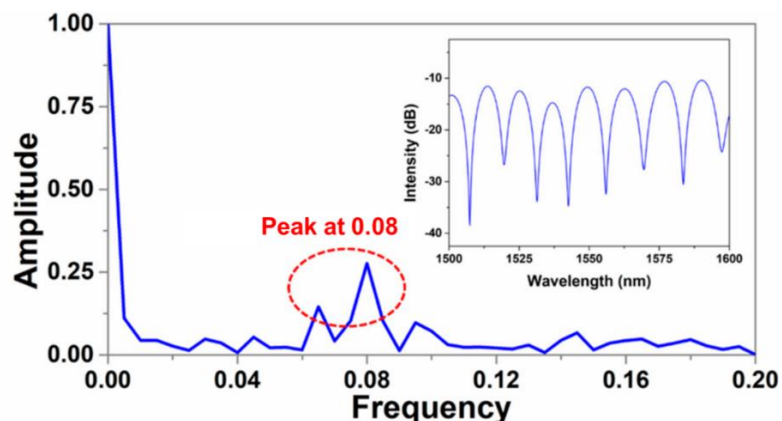


Figure 4.4. The interference spectrum of the MZI (inset) and the FFT spectrum [108].

The interference spectrum of the MZI sensor based on SMF-NCF-RCF-SMF structure is displayed in Figure 4.4 (inset). No distinct interference pattern can be recorded if the NCF is removed from the fiber structure. Actually, without the introduction of NCF, there was no obvious interference occurring which means that the temperature sensing cannot be realized. The NCF provides an interface to excite different fiber modes which will interfere in the RCF and then be coupled back to SMF. And thus, the interference spectra, which are the base for fiber sensing, can be recorded by OSA.

The spectrum is recorded from 1500 nm to 1600 nm using OSA with the resolution of 0.02 nm. In our experiment, the BBS with the bandwidth from 1470-1670 is used as the light source. However, in the maximum wavelength range of around 200 nm, the light energy distribution is not the same stable which means that the light power at the wavelength of around 1470 nm and around 1630 nm shows an obvious decrease compared to that at the wavelength ranging from 1500-1610 nm. That's why we recorded the spectra ranging from 1500-1600 nm which contains 8 interference dips that we think could be reliable for sensing results. The maximum extinction ratio (ER) is measured to be 27 dB and the free spectral range (FSR) is 12 nm. The large ER and FSR enable the demodulation of environmental parameters by utilizing both dip wavelength and intensity. The fast

Fourier transform (FFT) is conducted and the FFT spectrum is shown in Figure 4.4. Except for the fundamental mode, multiple high-order modes are also excited which is in correspondence with the simulation results depicted in Figure 4.3(b). The relationship between interference spectra variation and the external environment change can be explained by the interference equations below:

$$I = I_1 + \sum_k I_2^k + \sum_m 2 \cdot \sqrt{I_1 \cdot I_2^k} \cos \left[\frac{2\pi}{\lambda} \cdot (n_{eff}^1 - n_{eff}^{2,k}) \cdot L \right] \quad (4.1)$$

I , I_1 represent the intensity of output light and RC mode. I_2^k means the intensity of FC mode and multiple cladding modes. n_{eff}^1 represents the effective RI of the RC mode and $n_{eff}^{2,k}$ shows that of the FC mode and cladding modes. L is the interference length which can be seemed as the length of the RCF. The condition of destructive interference can be explained with the following equations:

$$2\pi \cdot (n_{eff}^1 - n_{eff}^{2,k}) \cdot L/\lambda = (2m + 1)\pi \quad (4.2)$$

$$\lambda = \frac{2\Delta n_{eff}L}{2m+1} \quad (4.3)$$

Δn_{eff} means the RI difference between the RC with the FC and the cladding. λ in Equation (3) means the wavelength of the interference dips.

4.4 Experimental results and analysis

4.4.1 The performance of temperature sensing

Figure 4.5 depicts the sensing performance of the RCF based MZI at different temperatures ranging from 35 °C to 70 °C with the interval of 5 °C. The experiment is conducted in the air with the surrounding RI of 1.0. As displayed in Figure 4.5(a), the wavelength of the interference dip shows continuous shift with temperature change which can be attributed to the alteration of effective RI difference (Δn_{eff}) and the interference

length (L) induced by the thermal effect. The thermal-optic coefficient of Ge-doped silica core is larger than that of fused silica cladding which means that Δn_{eff} will increase with the rising of the temperature and the redshift of dip wavelength can be observed [70]. In addition, the rising and declining of temperature will give rise to the expansion and shrink of the fiber length and further lead to the red and blue shift of the dip wavelength. This can be explained by Equation (4.3). The mathematical statistics between the temperature and the dip wavelength are implemented and the result is displayed in Figure 4.5(b). The red line represents the linear fit in the case of temperature increasing and the blue line shows that of temperature decreasing. The relationship of temperature and dip wavelength shows good linearity in the process of both temperatures rising and declining and the adjusted R square values (R^2) are both 0.99. The slope of temperature increasing is calculated to be 68 pm/°C and the 69 pm/°C slope is achieved when temperature decreases. The results are better than that reported in [109] which can be attributed to the different ring core sizes of the applied fiber. It should be noted that to make sure the temperature can be technically stable and measured reliably, a large heating oven was used in the experiment which means that we have to put not only the fiber part but also the fiber holders into the heating oven. The temperature change will inevitably give rise to the small change of fiber holding status which may further lead to very slight bending of fiber sensor and that's why the dips wavelength of "Temperature Decreasing" shows total shift compared to that of "Temperature Increasing". And also, it can be found that the slopes of linear fit in the processes of both "Temperature Increasing" and "Temperature Decreasing" are the same which means that no uncertain influence occurs. We think proper packaging of the fiber sensor can eliminate the differences.

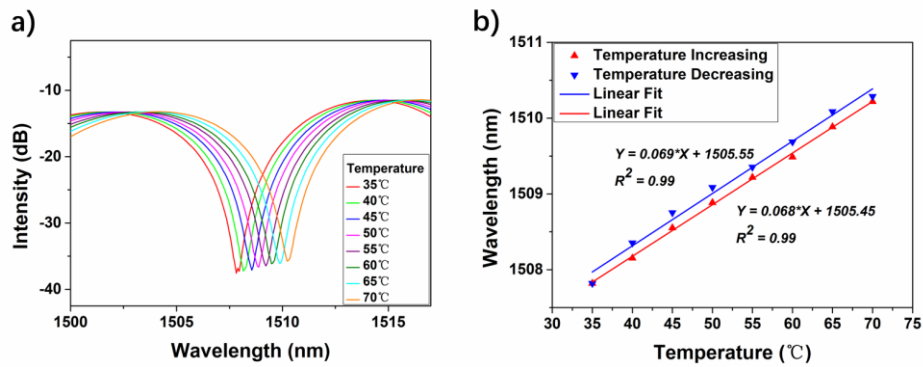


Figure 4.5. (a) The interference spectra of the proposed MZI sensor at different temperatures from 35 °C to 70 °C with the interval of 5 °C and (b) the relationship between temperature and dip wavelength with temperature increasing and decreasing [108].

The statistics of temperature and interference intensity are also conducted which is depicted in Figure 4.6. The dip intensity shows very slight alteration as the temperature changes. The linear fit gives the slope of 0.051 dB/°C which means that the intensity of the interference dip at around 1508 nm is insensitive to thermal effect.

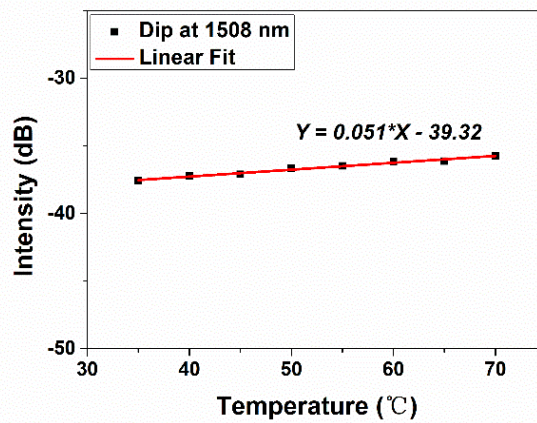


Figure 4.6. The relationship between temperature and intensity of interference dips at the dip wavelength around 1508 nm [108].

4.4.2 The performance of RI sensing

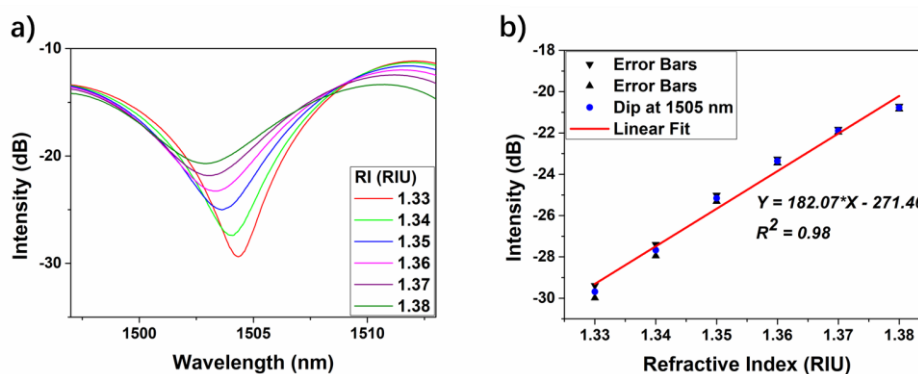


Figure 4.7. (a) The MZI interference spectra with different RIs ranging from 1.33 to 1.38 with the interval of 0.01 and (b) the relationship between RI and the intensity of interference dips [108].

The MZI can also be used for RI sensing because the excited cladding modes induced by NCF are sensitive to surrounding RI and the results are shown in Figure 4.7. Unlike the FC mode and RC mode which transmit around the center of RCF, cladding modes will be reflected on the interface of fiber cladding and air. Thus, cladding modes can be sensitive to the variation of surrounding materials which can easily tune both the amplitude and phase of the cladding modes. The interference spectra will display the corresponding alteration according to the change of the external environment. Figure 4.7(a) presents the sensing results with different values of RI ranging from 1.33 to 1.38 with the interval of 0.01 at room temperature (~ 25 °C). With the step increasing of surrounding RI, the interference spectra show a blue shift which can be explained by Equation (4.3). In addition, the change of external RI values can also lead to the amplitude change of cladding modes which gives rise to the alteration of interference intensity as shown in Equation (4.1). It also can be noticed that the dip shapes show slight changes. As we know, the intensity of the interference dips can be influenced by the light intensity transmitting in different paths (including core path and cladding path). The equal energy distribution of two paths can lead to large intensity of interference dips. Thus, the intensity of cladding modes will be strongly

affected by the surrounding RI which can result in the “leak” of light energy and that’s why the dip intensity can be further influenced. The dip shape is formed due to the interference between the core mode and cladding modes. The shape of interference dips we suppose is influenced by the excited multiple cladding modes which will be tuned with the variation of RI.

Figure 4.7(b) displays the relationship between RI and the dip intensity. The experiment is repeated and the error bars are signed as black triangles. The RI sensitivity is calculated to be 182.07 dB/RIU with the linearity of 0.98. Compared to the dip intensity change induced by the thermal effect, which is 0.051 dB/°C shown in Figure 4.6, that influenced by RI is obviously much more remarkable. This makes it possible for direct demodulation of RI with the dip intensity by ignoring the weak influence generated by the thermal effect.

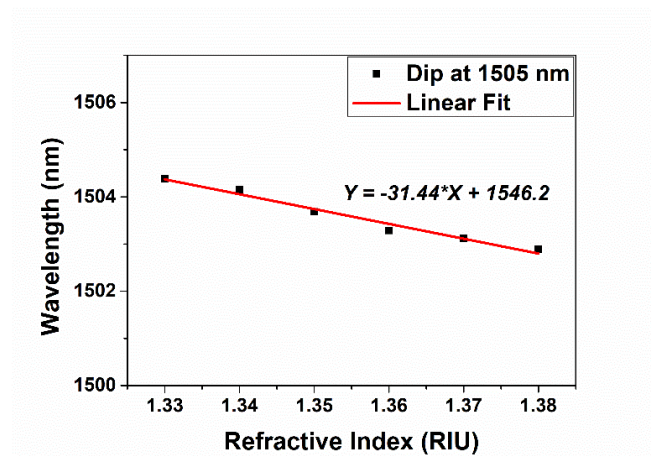


Figure 4.8. The mathematical statistics of RI and wavelength shift at the dip of around 1505 nm [108].

Figure 4.8 depicts the linear relation between RI and dip wavelength and the slope is calculated to be -31.44 nm/RIU. The temperature hence can also be demodulated by using the linear equations between wavelength shift with the variation of RI and temperature:

$$\Delta\lambda = 0.069 \times \Delta T + (-31.44) \times \Delta RI \quad (4.4)$$

$$\Delta T = \frac{1}{0.069} (\Delta\lambda + 31.44 \times \Delta RI) \quad (4.5)$$

where $\Delta\lambda$ means the wavelength shift, ΔT is the change of temperature and ΔRI represents that of RI.

4.5 Discussion

It should be noted that the liquid with different RI used in the experiment is measured at room temperature using a commercial saccharimeter so that we can make sure the RI values are accurate. However, the liquid RI will be changed when the temperature is varied. Thus, if we simultaneously tuned the temperature and RI, the precise value of RI cannot be recorded well which will result in the measurement error. In our lab, the real-time measurement of liquid RI cannot be realized and that's why we cannot get the output while the temperature and index were simultaneously being varied.

In addition, we have mentioned the limited ranges while dual-mode operation can be conducted. It is true that 1 dB/20°C is a big change and that's why we claim that the dual-mode operation must be controlled in the range of 35°C. The RI sensitivity is 182.07 dB/RIU which means that 0.01 RIU change will result in 1.82 dB variation which is larger than 1.75 dB variation induced by 35°C temperature change. By proper demodulation method, we think the error can be controlled in small ranges. However, considering the existing measurement error, we think the temperature range should be narrowed and the RI range needs to be specified. Thus, although the influence of thermal effect on interference dip intensity is slight (0.051 dB/°C) in the temperature range from 35 °C to 70 °C based on our measurement, large temperature variation can still result in a nonnegligible impact on dip intensity which will lead to a relatively large error on the demodulation of RI.

Therefore, in our experiment, the dual demodulation of temperature and RI will be confined in a finite temperature range (within 20 °C variations) to make sure the measurement error be controlled within reasonable limits. Future work can be done to seek the solution of such demodulation method that enables sensor application within a large measurement range, such as optimizing fiber structure or utilizing material assistance.

The bending will also be the non-negligible factor for the fiber sensor. In our experiment, the bending of the fiber sensor will truly affect the results. We did some research on this and found that the bending will lead to a blue shift of the dip wavelength with the sensitivity of around -3.68 nm/m^{-1} . That's why we have to make sure the fiber structure being straight when we are measuring the temperature and RI. We believe proper packaging can eliminate the influence of curvature and realize reliable sensing of temperature and RI.

4.6 Conclusion

In conclusion, the MZI fiber sensor based on SMF-NCF-RCF-SMF structure is successfully achieved. The experiments on temperature and RI sensing are conducted and dual demodulation of temperature and RI can be realized with the temperature variation under 20 °C and RI resolution of 0.01 ranging from 1.33 to 1.38. The maximum sensitivity of temperature sensing is 69 pm/°C and that of RI sensing reaches 182.07 dB/RIU and -31.44 nm/RIU with the intensity and wavelength demodulation methods, respectively. The proposed MZI sensor has advantages of cost-effective source, ease of fabrication and high sensitivity for both temperature and RI sensing. In addition, based on the cladding modes modulation, the MZI sensor reveals good potential for diverse applications, such as relative humidity sensing and pH sensing assisted with chemical materials. Future works will be conducted to extend its applications on various environmental monitoring.

5 The RCF-Based Sensor Used for Simultaneous Measurement of Temperature and Curvature

This chapter is reproduced with some adaptations from the manuscript “W. Yuan, Q. Zhao, L. Li, Y. Wang, and C. Yu, "Simultaneous measurement of temperature and curvature using ring-core fiber-based Mach-Zehnder interferometer," Optics Express 29, 17915-17925 (2021).”

In this chapter, an MZI fiber sensor based on RCF is proposed and successfully fabricated for the detection of temperature and curvature. The MZI fiber sensor can be applied for the detection of both temperature and curvature base on different sensing mechanisms. The experimental results indicate that the proposed sensor has a maximum temperature sensitivity of $72 \text{ pm}/^\circ\text{C}$ and the linearity reaches 0.9975. The experiments on curvature sensing were also conducted. The measurement range for curvature sensing is recorded from 1.3856 m^{-1} to 3.6661 m^{-1} with the sensitivity up to $-3.68 \text{ nm}/\text{m}^{-1}$. Meanwhile, the linearity is calculated to be 0.9959 which presents the remarkable and reliable sensing performance. By using the 2×2 matrix, the simultaneous measurement of temperature and curvature can be realized.

5.1 Introduction

In modern society, the status of optical fiber sensors is becoming more and more important. Fiber optic sensors have unique advantages, such as low price, easy preparation, excellent electromagnetic resistance, high sensitivity and so on. Fiber optic sensors have many applications, such as temperature [75-77, 110, 111], RI [112-117], strain [85, 118-122], bending [90, 123-126], gas [96, 99, 127-130] and humidity [131-135] detection. Among these parameters, the curvature is very important because it's significant in various applications including aircraft, large buildings, road and bridge engineering, precise instruments, etc.

Diverse fiber structures have been studied for curvature sensing. For instance, Tian et al. reported the twisted single-mode-multimode-single-mode hybrid fiber structure offering the curvature sensitivity of -2.42 nm/m^{-1} over a curvature measurement range of $0 - 1.7390 \text{ m}^{-1}$ [89]. Dong et al. proposed the cascaded fiber interferometer with the sensitivity of 4.362 nm/m^{-1} in the measurement range of $0 - 1.134 \text{ m}^{-1}$ [91]. Jiang et al. reported the Mach-Zehnder interferometer (MZI) based on D-Shaped Fiber Grating and achieved the sensitivity up to 87.7 nm/m^{-1} to the low sensing range from 0 to 0.3 m^{-1} [92]. Barrera et al. used the Long Period Gratings (LPG) in multicore fibers and realized the linear sensing from 0 to 1.77 m^{-1} with the sensitivity up to -4.85 nm/m^{-1} [90]. Gong et al. presented the fiber interferometer with two peanut-shaped structures and got the -21.87 nm/m^{-1} with the sensing ranges from 2.5 m^{-1} to 4.2 m^{-1} [136]. Generally, the fiber sensors can be sensitive to the surrounding environment, especially to temperature. The variation of temperature can give rise to the change of interference patterns which will further result in the inevitable measurement error of curvature sensing. Thus, the simultaneous

monitoring of temperature and curvature will be the practical solution for measurement error reduction and also be of great importance for the widespread applications of multiparametric fiber-optic sensors with high-precision experimental results.

In this chapter, we report an MZI fiber sensor constituted by RCF, NCF and SMFs for the detection of temperature and curvature. Due to the identical diameters of the three kinds of fibers, the sensor can be prepared through the method of direct fusion splicing. The fiber sensor can be formed by two steps: firstly, the NCF is spliced with the RCF to generate the N-R structure; secondly, the N-R structure is connected to two segments of SMFs which serve as the lead-in and lead-out fibers. The fabrication process of direct fusion splicing makes sure that the fiber sensor can have a sturdy structure compared to other fiber structures, such as thin-tapered fiber or side-polished fiber. In addition, the easy preparation method can also guarantee the repeatability of the sensor configurations. The MZI fiber sensor can be applied for the detection of both temperature and curvature base on different sensing mechanisms. The experimental results indicate that the proposed sensor has a maximum temperature sensitivity of $72 \text{ pm}/^\circ\text{C}$ and the linearity reaches 0.9975. The experiments on curvature sensing are also conducted. The measurement range for curvature sensing is recorded from 1.3856 m^{-1} to 3.6661 m^{-1} with the sensitivity up to $-3.68 \text{ nm}/\text{m}^{-1}$. Meanwhile, the linearity is calculated to be 0.9959 which presents the remarkable and reliable sensing performance.

The advantages of the proposed sensor in this work are listed below:

1. **The novelty of the sensor structure.** We firstly proposed the SMF-NCF-RCF-SMF structure that is used for curvature sensing. The theoretical analysis, simulation and experiments are all conducted to elaborate the mechanism and performance of the MZI sensor. The specific RCF is studied in detail to illustrate the light transmission and interference occurring.

2. **Good repeatability of structure and data, and reliable sensing performance.** By using NCF, the multiple cladding modes can be excited at the interface of NCF and RCF. Unlike the mismatched fiber structure and multi-core structure which may need precise mismatched distance or core-to-core splicing that leads to the difficulty of repeatability, our structure with a simple and effective fabrication method enables good repeatability of fabrication. The linearity of curvature sensing reaches 0.9961 and 0.9969 for curvature increasing and decreasing which demonstrates good repeatability and reliable sensing performance. It has been manifested that the experimental data obtained from the proposed structure is reliable and highly repeatable, which in turn proves the effectiveness of our homemade structure of MZI-based fiber sensor with the unique easy-to-fabricate feature.
3. **The cost-effective, tiny and portable sensor structure.** The commercial RCF (YOFC) has the cost of 10 RMB/m and the 2-cm RCF used in the MZI sensor makes its cost even lower. The direct splicing method also provides a convenient and cost-effective fabrication process. The interference occurring in a single fiber enables a miniaturized MZI structure which gives rise to a tiny and portable sensor.
4. **Acceptable sensitivity of both curvature and temperature.** It is admitted that the sensitivity of the proposed sensor is not top-level. The temperature sensitivity of 72 pm/°C and curvature sensitivity of -3.68 nm/m⁻¹ are better compared to many kinds of fiber sensors. In addition, the advantages mentioned above enable the proposed fiber sensor to monitor curvature and temperature reliably in a relatively large sensing range with low cost.

5.2 Experimental setups

5.2.1 The structure of the curvature sensor

The NCF and RCF are purchased from Yangtze Optical Fiber Company (YOFC). As can be seen from Figure 5.1, the microscope image of NCF is shown on the left and that of RCF is displayed on the right. The diameters of NCF and RCF have the same value of $125\ \mu\text{m}$ which is identical to that of SMFs. Thus, the fiber sensor can be prepared by direct fusion splicing without structural mismatch. The NCF is the uniform SiO_2 material while the RCF can be divided into three parts: fiber center (FC), ring core (RC) and cladding area. From the microscope image of RCF in Figure 5.1 (right), it can be clearly found that the diameter of RC is $18.7\ \mu\text{m}$ and that of FC is $10.9\ \mu\text{m}$. In addition, according to the information provided by YOFC, it is known that the RI of FC and cladding is 1.44402 and that of RC is 0.93% higher which is 1.45745.

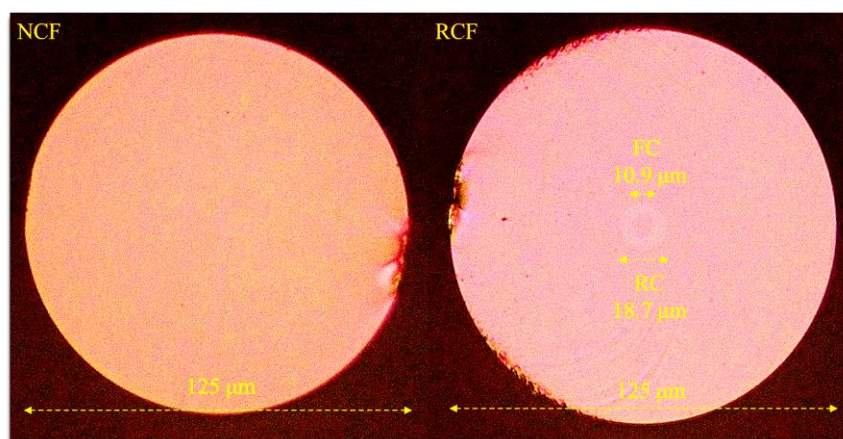


Figure 5.1. The microscope images of section views of NCF and RCF [137].

5.2.2 The experimental setups for curvature sensing

The experimental setup is shown in Figure 5.2(a) and Figure 5.2(b) displays the schematic diagram of the MZI fiber structure. The MZI sensor is primarily formed by fusion splicing

1-mm NCF with 20-mm RCF. Then the N-R fiber structure is connected with two segments of SMFs. The fiber sensor is held by two fiber holders which are fixed on the translation stations. One of the stations is immobilized and the other one can be tuned by rotating the controller. The distance between two fiber holders (L_0) is set to be 50 mm to enable a relatively large sensing range with the moving step of 10 μm . The SMF fusion spliced with the NCF is connected to a broadband light source (BBS) with the bandwidth from 1470 nm to 1670 nm. The output light of BBS can be coupled into the optical spectrum analyzer (OSA, YOKOGAWA, AQ6370D) with the resolution of 0.02 nm through the SMF connected with the RCF.

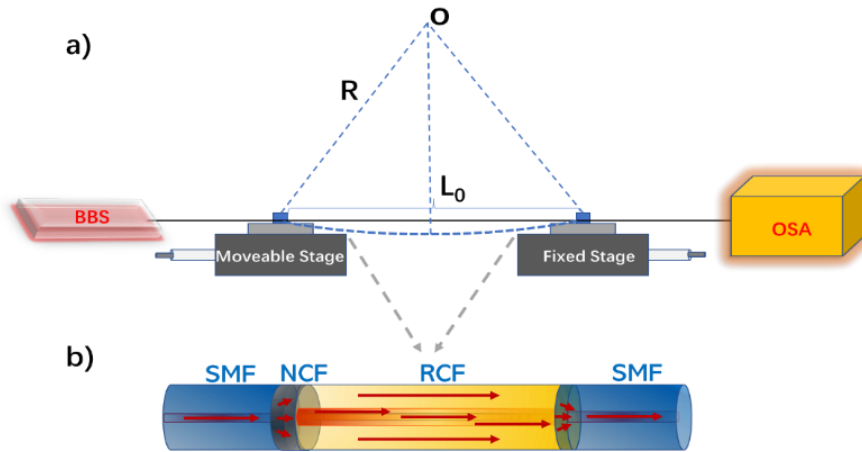


Figure 5.2. The schematic diagrams of (a) the experimental setup for curvature sensing and (b) the MZI sensor based on the RCF [137].

Different curvature values are achieved by tuning the movable station with the step of 10 μm . The curvature can be calculated by the equation below [138]:

$$C = \frac{1}{R} \cong \sqrt{\frac{24x}{L_0^3}} \quad (5.1)$$

where C refers to the curvature value, R represents the bending radius, x is the displacement of the moveable stage, and L_0 is the fiber length between two fiber holders when the fiber is straight.

5.3 The sensing mechanism

5.3.1 The principles of temperature and curvature detection

As well known, the interference of MZI structure depends on the differences of different arms. The interference patterns are determined by the discrepancy of arm's length and effective RIs. For the proposed MZI sensor in this chapter, the physical lengths of the core arm and cladding arm are exactly the same due to the miniaturized MZI structure based on one single RCF. Thus, this means that the interference occurs due to the effective RI difference between fiber core and cladding. The intensity of the output light can be expressed by the equation below:

$$I = I_1 + \sum_k I_2^k + \sum_m 2 \cdot \sqrt{I_1 \cdot I_2^k} \cos \left[\frac{2\pi}{\lambda} \cdot (n_{eff}^1 - n_{eff}^{2,k}) \cdot L \right] \quad (5.2)$$

I means the intensity of output light and I_1 is that of RC mode. I_2^k represents the intensity of FC mode and multiple cladding modes. The effective RI of the RC mode is expressed as n_{eff}^1 and $n_{eff}^{2,k}$ means that of the FC mode and cladding modes. L represents the interference length of the MZI structure.

Referring to [139], the relationship between the wavelength of interference dip and bending curvature can be written as:

$$\lambda_{dip} = \frac{\Delta n_{eff} L}{2m+1} + \frac{k \cdot L \cdot s}{2m+1} \times C \quad (5.3)$$

where m is an integer, k is the constant of the strain RI coefficient. L is the interference length. s is the distance between the core mode and cladding modes, C is the bending curvature and Δn_{eff} is the effective RI difference between the core and cladding modes.

According to equation (5.3), the dip wavelength is linearly proportional to the bending curvature with a slope coefficient described as $\frac{kLs}{2m+1}$. Because of the negative strain RI coefficient [140], the wavelength of interference dip will induce blueshift with the increase

of bending curvature.

In addition to the bending curvature, it should be noted that the temperature variation can also give rise to the shift of interference dip. The dip wavelength of the destructive interference can be calculated by the following equations [68]:

$$2\pi \cdot (n_{eff}^1 - n_{eff}^{2,k}) \cdot L/\lambda = (2m + 1)\pi \quad (5.4)$$

$$\lambda_{dip} = \frac{2\Delta n_{eff}L}{2m+1} = \frac{2(\Delta n_{eff} + \vartheta \Delta T)(L_0 + k_0 \Delta T)}{2m+1} \quad (5.5)$$

Δn_{eff} means the effective RI difference between the RC mode with the FC mode and the cladding modes. λ_{dip} means the wavelength of the interference dip. L_0 is the initial interference length of the MZI at room temperature (25°C). ϑ represents the difference of thermo-optic coefficient between core and cladding. k_0 represents the thermal expansion coefficient of the RCF and ΔT is the temperature variation. The change of temperature will result in two main changes of the fiber MZI. One of the influencing factors is the thermo-optic coefficient which determines the variation of the effective RI difference between core and cladding and the other is the thermal expansion coefficient that is related to alteration of MZI interference length. Because the change of L induced by thermal effect can be very slight which will bring the negligible influence on interference spectra, the thermal response on the MZI sensor can be mainly attributed to the thermo-optic coefficient which leads to the change of Δn_{eff} . According to (5.5), the relationship of dip wavelength and temperature depends on the factor $\frac{2L\vartheta}{2m+1}$ which can be seemed as a constant. Thus, the theoretical analysis indicates the linear response of dip wavelength to temperature change.

5.3.2 The Rsoft simulation results

The simulation work is conducted to exhibit the light transmission in the RCF and bent RCF with the curvature of around 1.3856 m^{-1} which are shown in Figures 5.3(a) and 5.3(b).

The modeling of MZI structure and curved structure with SMF-NCF-RCF-SMF is conducted using Rsoft with the simulation tool of BeamPROP. For SMF, the diameters of core and cladding are set to be $9\ \mu\text{m}$ and $125\ \mu\text{m}$ with the RI values of 1.4504 and 1.4447, respectively. The lengths of NCF and RCF are built as 1 mm and 20 mm. The RCF is modeled under the measurement results shown in Figure 5.1. The wavelength of 1550 nm is chosen as the free-space wavelength.

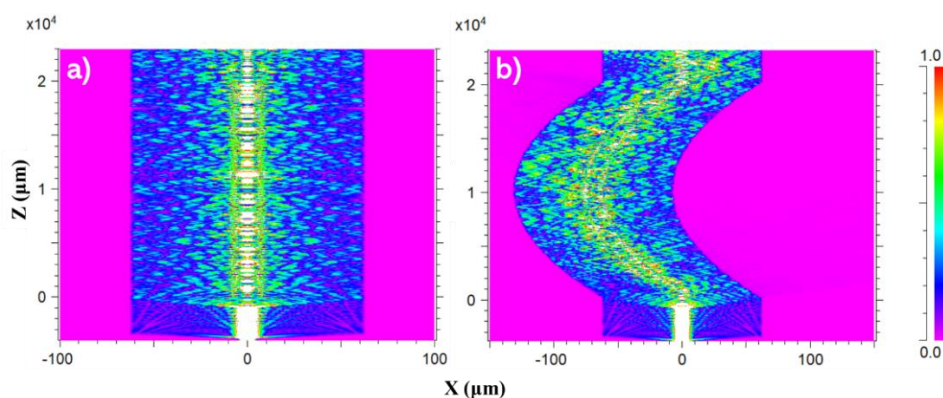


Figure 5.3. The Rsoft simulation results of light transmission in (a) straight RCF and (b) curved RCF [137].

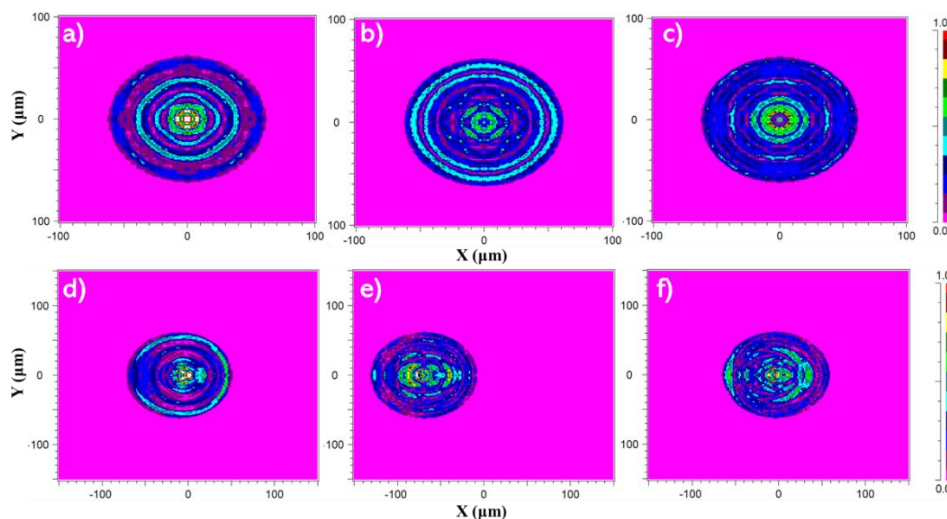


Figure 5.4. The simulated mode distribution of the cross-section region of the straight RCF with the transmission distance of (a) 1 mm, (b) 10 mm, (c) 20 mm, and that of the curved RCF with the transmission distances of (d) 1 mm, (e) 10 mm, and (f) 20 mm [137].

Further to the light transmission properties of the RCF in different statuses, the mode distributions of the cross-section region of the RCF are also simulated and shown in Figure 5.4. Figures 5.4(a-c) display the mode profiles of the cross-section region of the straight RCF at different transmission distances of 1 mm, 10 mm and 20 mm, respectively. It can be clearly seen that different fiber modes, including RC mode, FC mode and cladding modes, are excited and interfered in RCF and then coupled into the SMF. Benefitting from the specific layout of the ring core structure, the fiber modes can be intensely sensitive to curvature which means that a slight curvature value will give rise to significant variation of fiber modes. Accordingly, the mode profiles of the bent RCF at different transmission distances are also simulated which can be found in Figure 5.4(d-f). The curvature-induced change in fiber modes will directly result in the change of interference patterns.

5.4 Experiments and discussions

5.4.1 The influence of NCF and RCF

The influence of the length of NCF and RCF on the MZI interference patterns is firstly studied and the results are shown in Figure 5.5. In Figure 5.5(a), 1-mm NCF is chosen in the MZI structure and fusion spliced with RCF of different lengths of 10 cm, 6.7 cm, 4.3 cm, 2.5 cm, 2 cm, 1.5 cm, 1 cm and 0.5 cm, respectively. It can be found that the extinction ratio (ER) is small when 10 cm RCF is used which can be attributed to the dispersion of excited cladding modes. With the decrease of RCF length, the ER is increased and the free spectral range (FSR) is widened. Thus, the 2-cm length of RCF is chosen for a relatively large FSR and long interference distance for curvature sensing. Figure 5.5(b) displays the interference spectra of 2-cm RCF based MZI with different lengths of NCF at 10 mm, 7

mm, 5 mm, 3 mm, 1 mm and 0, respectively. The longest NCF ($L \sim 10$ cm) used in our experiments results in a small ER due to the large transmitting loss in NCF. With the decline of NCF length, the ER is increased accordingly. However, it is noticed that the ER of the interference pattern becomes tiny without the NCF (0-mm NCF). This is because no adequate cladding mode can be excited. On the basis of all the collected results, 1-mm NCF and 2-cm RCF are selected to construct the MZI sensor with the proposed all-fiber structure of SMF-NCF-RCF-SMF.

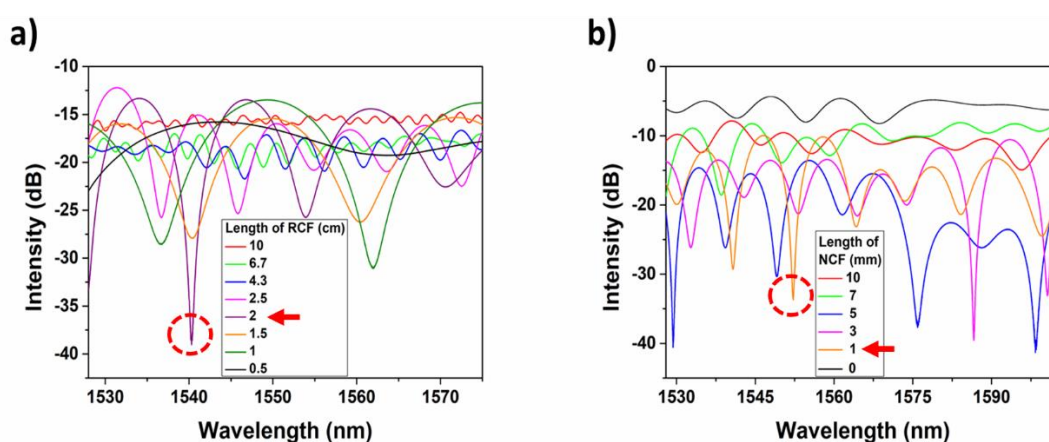


Figure 5.5. (a) The interference spectra of 1-mm NCF MZI sensor with different lengths of RCF at 10 cm, 6.7 cm, 4.3 cm, 2.5 cm, 2 cm, 1.5 cm, 1 cm, and 0.5 cm and (b) that of 2-cm RCF MZI sensor with different lengths of NCF at 10 mm, 7 mm, 5 mm, 3 mm, 1 mm and 0 [137].

5.4.2 The performance of curvature sensing

The research on curvature sensing using the RCF based MZI fiber structure is conducted and the result is shown in Figure 5.6. The optical spectra are recorded from around 1575 nm to 1645 nm and five interference dips can be observed in the measurement range. The curvature is altered by turning the rotator controlling the movable stage with the step of 10 μm and the interference spectrum is preserved by the OSA at different steps. Different curvature values are recorded as 1.3856 m^{-1} , 1.9596 m^{-1} , 2.4 m^{-1} , 2.7713 m^{-1} , 3.0984 m^{-1} , 3.3941 m^{-1} , 3.6661 m^{-1} . As can be seen from Figure 5.6, with the increase of the curvature value, the wavelength of the interference dip presents a continuous blue-shift which is

coincident with the theoretical analysis. To realize the dual demodulation of temperature and curvature, two characteristic interference dips are chosen for analysis. The interference dip around 1587 nm is named dip 1 and that around 1642 nm is denominated as dip 2.

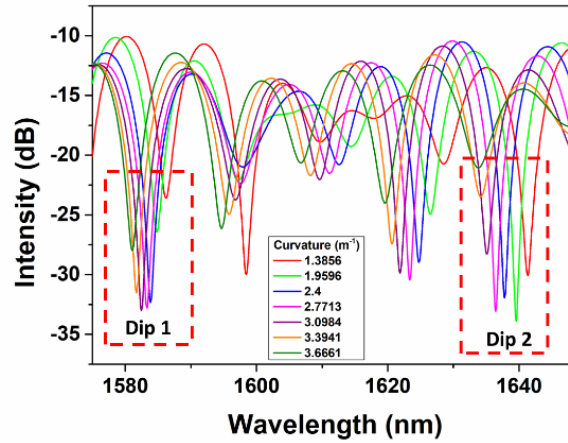


Figure 5.6. The interference spectra of the MZI fiber sensor with different bending curvatures [137].

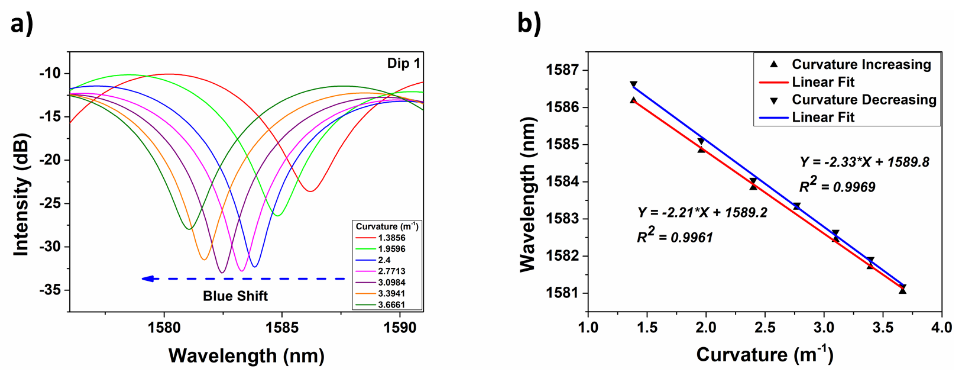


Figure 5.7. (a) The interference spectra of dip 1 with different curvatures. (b) the relationship between curvature and dip wavelength with curvature increasing and decreasing [137].

The detailed interference spectra of dip 1 are displayed in Figure 5.7(a) and the mathematical statistics of curvature and wavelength are conducted which is shown in Figure 5.7(b). The experiments of curvature increasing and decreasing are done by turning the rotator that controlled the movable translation station. For dip 1, with the raise of the curvature value, the dip wavelength presents a linear blue shift. The sensitivity is calculated to be -2.21 nm/m^{-1} and the linearity reaches 0.9961. The curvature decreasing gives rise to the redshift of dip wavelength and the linear fit is shown as the blue line in Figure 5.7 (b).

The slope is -2.33 nm/m^{-1} with the adjusted R-square value of 0.9969 which shows the good linearity of dip wavelength and curvature value. The wavelength of dip 2 also displays linear blue shift when the curvature is increased and the experimental results are displayed in Figure 5.8. In the case of curvature rising, the sensitivity of -3.48 nm/m^{-1} is achieved with the correlation coefficient square of 0.9924. In the process of curvature declining, the sensitivity is -3.68 nm/m^{-1} with the correlation coefficient square of 0.9959. The maximum curvature sensitivity of -3.68 nm/m^{-1} is around 1.5 times larger than that reported in [89, 141].

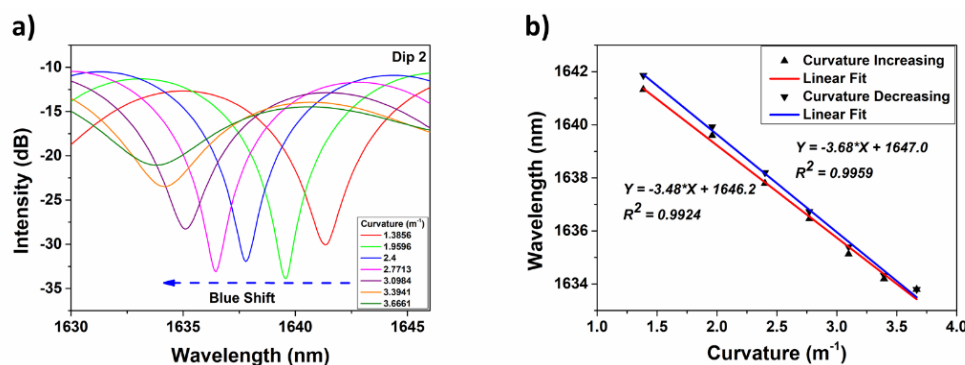


Figure 5.8. (a) The interference spectra of dip 2 with different curvatures and (b) the relationship between curvature and dip wavelength with curvature increasing and decreasing [137].

5.4.3 The performance of temperature sensing

The experiments on temperature sensing are also conducted and the results are shown in Figure 5.9. The interference spectra of dip 1 are displayed in Figure 5.9(a) and Figure 5.9(b) presents that of dip 2. According to Equation (5.5), the relationship of dip wavelength and temperature depends on the factor $\frac{2L\theta}{2m+1}$ which is a positive constant. Thus, with the increase of temperature, the dip wavelength tends to show a red shift. As can be seen from Figure 5.9(a), the wavelength of interference dip 1 presents a linear redshift when the temperature increases from $25 \text{ }^\circ\text{C}$ to $55 \text{ }^\circ\text{C}$ with the step of $5 \text{ }^\circ\text{C}$ which is corresponding to the theoretical analysis. Dip 2 gives similar interference patterns compared to dip 1 with

temperature change which is displayed in Figure 5.9(b).

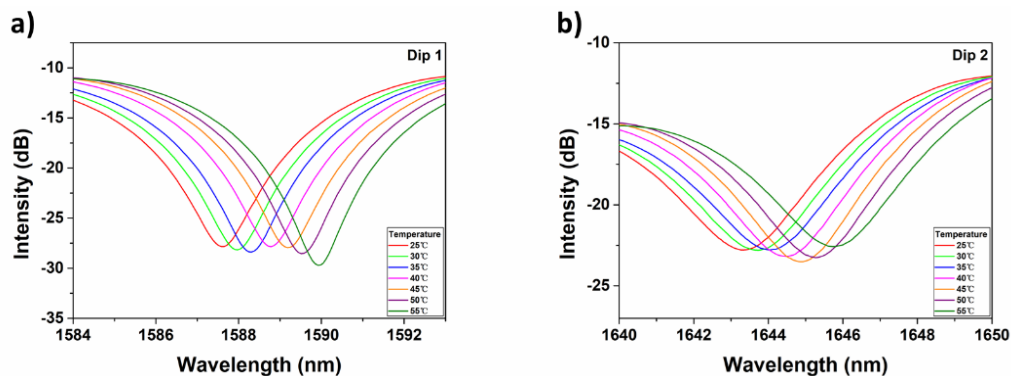


Figure 5.9. The interference spectra of (a) dip 1 and (b) dip 2 with different temperatures from 25 °C to 55 °C with an interval of 5 °C [137].

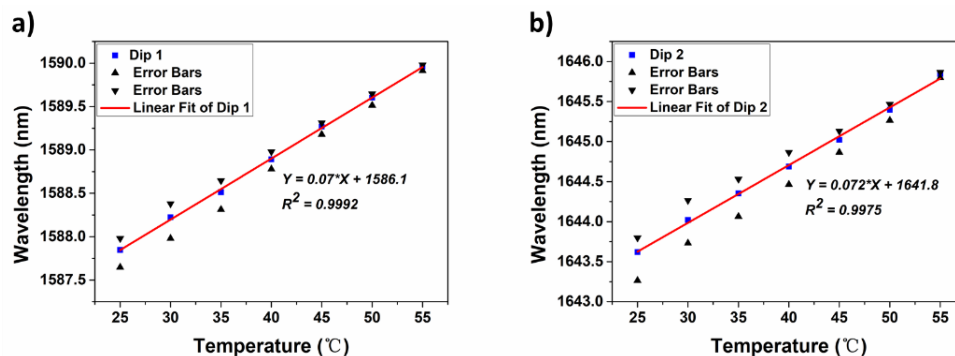


Figure 5.10. The mathematical statistics of temperature and wavelength shift of (a) dip 1 and (b) dip 2 [137].

The mathematical statistics of temperature and wavelength shifting are displayed in Figure 5.10. The values of dip wavelength are recorded and calculated by repeating the experiments four times with the temperature increase and decrease. The error bars are represented by the triangles and the inverted triangles. For dip 1, the sensitivity is calculated to be 70 pm/°C and the linearity reaches 0.9992. As shown in Figure 5.10(b), the sensitivity of dip 2 is measured to be 72 pm/°C with the linearity of 0.9975. The experimental results indicate the good linearity of temperature sensing with the relatively high temperature sensitivity which is 6 times larger than that reported in [125] and 1.8 times larger than that reported in [142].

5.4.4 The method for simultaneous measurement of temperature and curvature

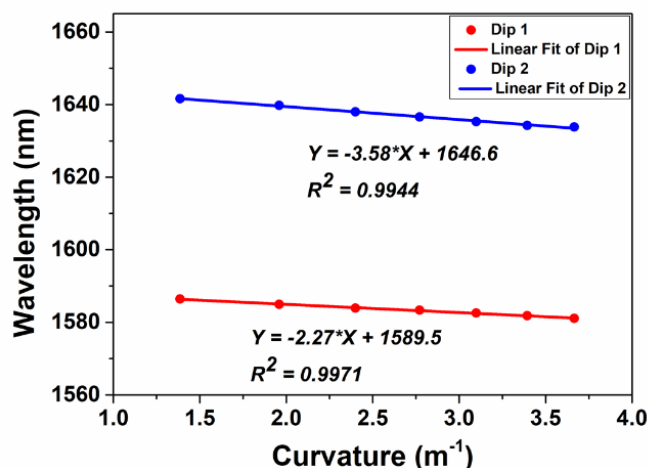


Figure 5.11. The linear relationship between curvature and wavelength of dip 1 (red line) and dip 2 (blue line) [137].

In this work, not only the theoretical analysis but also the experiments have been done in our work which can be found in Figures 5.6, 5.7, 5.8, 5.9, 5.10. In addition, due to the temperature-induced uncertain changes, such as fiber holding status and expansion of metal-base, the precise value of curvature cannot be measured in real-time with the tuning of temperature. However, based on the measurement principles, temperature sensing is mainly based on the factor $\frac{2L\theta}{2m+1}$ and curvature sensing is mainly based on the factor $\frac{kLs}{2m+1}$. The two factors won't be influenced by the alteration of temperature and curvature. Thus, we can use the 2×2 matrix to simultaneously demodulate temperature and curvature which has been fully demonstrated in literatures [91, 143].

Figure 5.11 presents the linear equations of curvature and dip wavelength of dip 1 and dip 2 by taking the average values of dip wavelengths with the process of curvature increasing and decreasing. The curvature sensitivity for dip 1 and dip 2 reaches -2.27 nm/m^{-1} and -3.58 nm/m^{-1} , respectively.

The simultaneous measurement of temperature and curvature can be realized by using the 2×2 matrix based on the linear relationship between wavelength shift with the variation of temperature and curvature:

$$\begin{bmatrix} \Delta\lambda_1 \\ \Delta\lambda_2 \end{bmatrix} = \begin{bmatrix} 0.07 & -2.27 \\ 0.072 & -3.58 \end{bmatrix} \begin{bmatrix} \Delta T \\ \Delta C \end{bmatrix} \quad (5.6)$$

where $\Delta\lambda_1$ means the wavelength shifting of dip 1 and $\Delta\lambda_2$ means that of dip 2.

By rearranging the matrix provided in Equation (5.6), the temperature and curvature values can be demodulated with the transformed matrix below:

$$\begin{bmatrix} \Delta T \\ \Delta C \end{bmatrix} = \frac{1}{-0.08716} \begin{bmatrix} -3.58 & 2.27 \\ -0.072 & 0.07 \end{bmatrix} \begin{bmatrix} \Delta\lambda_1 \\ \Delta\lambda_2 \end{bmatrix} \quad (5.7)$$

Evidently, with the convenient collection of the wavelength shift of the featured interference dips, the temperature and the curvature change can be easily deduced with our homemade and specially designed MZI sensor. However, it should be noted that the curvature sensing of the MZI fiber sensor is realized in the axis direction of the translation stage. In the near future, multi-dimensional curvature sensing is expected by improving the structure of RCF-based MZI sensors, such as side-polishing or chemical etching, to meet the requirements of practical applications. In addition, benefiting from the all-fiber structure of the proposed sensor, high stability can be guaranteed due to optical fiber properties of structural stability and chemical resistance.

5.5 Conclusion

In conclusion, the MZI fiber sensor based on RCF has been successfully achieved for simultaneous measurement of temperature and curvature. The theoretical and experimental analyses have been done to elaborate on the sensing principle and performance. The temperature sensitivity reaches up to 72 pm/°C with the linearity of 0.9975 in the range from 25 °C to 55 °C. The maximum sensitivity of curvature sensing is -3.68 nm/m⁻¹ and the

adjusted R square value reaches 0.9959 within the measurement range of 1.3856 to 3.6661 m^{-1} . Two interference dips around 1587 nm and 1642 nm are selected for data analysis. Based on the linear relationship between dip wavelength shift with the variation of temperature and curvature, these two parameters can be simultaneously demodulated by using the 2×2 matrix. The proposed curvature sensor based on the MZI fiber structure has the advantages of compact size, low cost and high sensitivity with a large sensing range. It also shows good potential for extensive applications such as pH sensing and humidity sensing.

6 The HCBF-Based Sensor for Human Breath Monitoring

This chapter is reproduced with some adaptations from the manuscript “W. Yuan, L. Li, Y. Wang, Z. Lian, D. Chen, C. Yu, and C. Lu, “Temperature and curvature insensitive all-fiber sensor used for human breath monitoring,” Optics Express 29, 26375-26384 (2021).”

In this chapter, an all-fiber sensor based on hollow core Bragg fiber (HCBF) is proposed and successfully manufactured, which can be used for human breath monitoring. Benefiting from the identical outer diameters of HCBF and single-mode fibers (SMFs), the sensor can be directly constructed by sandwiching a segment of HCBF between two SMFs. Based on optical propagation properties of HCBF, the transmission light is sensitive to specific environmental changes induced by human breath. Thus, the breath signals can be explicitly recorded by measuring the intensity of the transmitted laser. The sensor presents a rapid response time of ~ 0.15 s and a recovery time of ~ 0.65 s. In addition, the HCBF-based sensor shows good insensitivity to the variation of temperature and curvature, which enables its reliable sensing performance in the dynamic and changeful environment.

6.1 Introduction

Optical fiber sensors have attracted wide attention because of advantages such as cost-efficient manufacture, ease of fabrication, outstanding electromagnetic and chemical resistance, etc. Various fiber sensors have been investigated for widespread applications, including temperature [74, 110, 111, 144, 145], humidity [132, 146-148], curvature [92, 140, 141, 149], refractive index (RI) [82, 83, 115, 150, 151], gas [99, 100, 152, 153], pH value [94, 95] and vital signs monitoring [154-162]. The vital signs monitoring, including human breath and heartbeat detection, is a promising research direction for fiber sensors [155]. Human breath plays an important role in the noninvasive diagnosis of diseases. The health status of people can be evaluated by breath frequency and depth which entails the sensor with the capability of continuous monitoring and fast response time. To date, a variety of specialized optical fiber structures have been developed for human breath monitoring. In 2010, Akita et al. developed a hetero-core optical fiber structure coated with hygroscopic polymer layers, which can be used for human breath monitoring, and the response time reached 400 ms [163]. After that, in 2017, Li et al. reported the side polished optical fiber coated by molybdenum disulfide with the response time of 0.85 s and the recovery time of 0.85 s [164]. In 2018, Aldaba et al. proposed the sensor based on SnO₂ sputtering deposition on a microstructured optical fiber Fabry-Pérot (FP) sensing head that shows a response time of 370 ms and a recovery time of 380 ms [165]. Afterward, Jiang et al. demonstrated a fiber sensor by depositing graphene oxide onto tilted fiber grating, exhibiting an ultrafast response within ~42 ms [166]. In 2020, Yi et al. proposed a gelatin film-assisted fiber breath sensor consisting of a microknot resonator superimposed on a Mach-Zehnder interferometer with an ultrafast response of 84 ms and recovery time of 29

ms [167]. However, all the fiber sensors used for human breath monitoring are combined with materials that may limit their applications in various ambient.

In view of this, to overcome the inconvenience brought by materials, we firstly propose and experimentally demonstrate an all-fiber sensor based on hollow core Bragg fiber (HCBF) used for human breath monitoring. Many HCBF-based sensors have been investigated before which demonstrates the excellent performances in sensing applications [168-170]. The sensor presented in this work is composed of 2.5 cm-length HCBF, which is directly spliced between two pieces of single-mode fibers (SMFs). Due to human breath-induced cladding modes' dissipation of HCBF, the breath signals can be demodulated by the variation of light transmission intensity. Unlike the materials-assisted fiber sensors, the fiber sensor proposed in this work is of all-fiber structure. It should be noted that materials-assisted fiber sensors may have a severe problem with sensor instability which can be caused by materials alteration or loose combination due to temperature change or chemical corrosion. Herein, we propose an all-fiber sensor to solve the aforementioned problems. The HCBF-based sensor shows a fast response time of 0.15 s and recovery time of 0.65 s. In addition, the test of the proposed sensor at different temperature and curvature values is conducted. The experimental results demonstrate that the sensor is insensitive to the variation of temperature and curvature. Moreover, benefiting from the all-fiber structure, the stability of the sensor can be guaranteed due to the properties of optical fibers with intensely structural stability and chemical resistance.

6.2 Fiber design and sensor fabrication

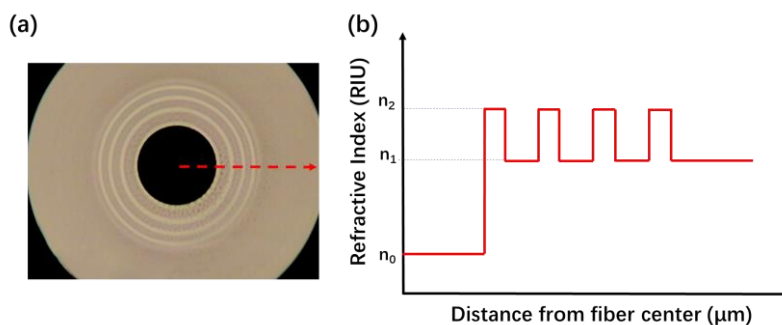


Figure 6.1. (a) The cross-section view of HCBF and (b) refractive index distribution along the radial direction [171].

The hollow core Bragg fiber is a kind of hollow core photonic crystal fibers (HC-PCFs) in which light is guided in the air core confined by the photonic bandgap cladding. In most of the proposed works, the cladding of the HC-PCFs is a periodic arrangement of air holes running along the entire length of the fiber. Different from these fibers, HCBF confines light in the air core surrounded by one-dimensional rings with low and high refractive index functions as Bragg reflectors but not two-dimensional lattice holes. With the increase of the pairs of bilayers, the transmission loss decreases, and most of the guided energy will be confined and guided in the air core, which is beneficial to high-power light delivery. However, in some sensing applications, part of the guided light is expected to spread out of the cladding and interact with the external environment to detect specific parameters with high sensitivity effectively. According to our previous simulation result and fiber drawing experience [172], four pairs of bilayers and a large air core with the diameter of $32\ \mu\text{m}$ is an optimized tradeoff. In order to match with link fiber, the $125\ \mu\text{m}$ outer diameter of the HCBF is the same as the outer diameter of an SMF. The cross-section view of the proposed HCBF is photographed by scanning electron microscope (SEM) and the refractive index distribution is shown in Figure 6.1. We have done the simulation work of the proposed HCBF to get the optimal parameters of the core diameter and one-dimensional Bragg rings. To meet our experimental requirements, the energy distribution between guide mode and

leakage mode should be well designed so that the light will not be completely bound into the core (which will lead to a very low sensitivity) and also will not leak out completely (which will cause very large transmission loss). Actually, the four bi-layers HCBF structure is not the only optimal design in the simulation results. However, considering the errors (deformation, asymmetry, etc.) in the drawing process, the prepared four bi-layers structure can achieve a better transmission spectrum compared to others. Thus, based on fiber drawing experience, four pairs of bilayers and a large air core with a diameter of 32 μm is an optimized tradeoff.

The preform of the Bragg fiber is deposited in the inner side of a commercial silica tube by using modified chemical vapor deposition (MCVD) equipment and drawn into expected fiber via a modified drawing tower [173]. The high and low refractive index (RI) at 1550nm and the thickness of each layer are 1.454, 1.444, 1.06 μm , and 3.07 μm , respectively. It is noted that the fiber is fabricated through optical fiber preform melting at high temperature (1900 $^{\circ}\text{C}$). The Ge ions doped in the core area are hard to diffuse to cladding area even at 1900 $^{\circ}\text{C}$. After the annealing process, the produced fiber structure can have extreme stability.

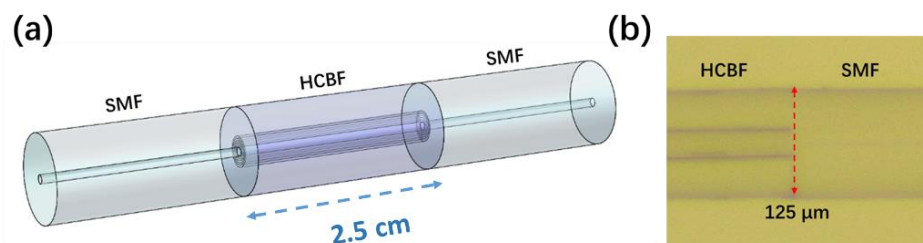


Figure 6.2. (a) The schematic diagram of HCBF based sensor and (b) the microscope image of splicing point between HCBF and SMF [171].

The schematic diagram of the HCBF-based sensor and the microscope image of the splicing point between HCBF and SMF are shown in Figures 6.2(a) and (b). Due to the

identical diameters of HCBF and SMF, the HCBF can be manually spliced with SMF without size mismatch. A commercial fusion splicer (FITEL, S178A, FURUKAWA) is used in the experiment. The discharge amount is chosen as the value of 20 shown in the device and the arc duration is 200 ms. The arc power and duration time have been optimized to minimize the deformation of the air core and ensure the mechanical strength of the splicing points. As can be seen from Figure 6.2(a), the HCBF-based sensor is composed of HCBF sandwiched between two pieces of SMFs. Based on the results of our previous studies [172], the applied length of HCBF is chosen as 2.5 cm, which can ensure a relatively large transmission intensity and the coverage of human breath area. The light can be coupled into HCBF through lead-in SMF and collected by the other for data recording and analysis.

6.3 The sensing mechanism

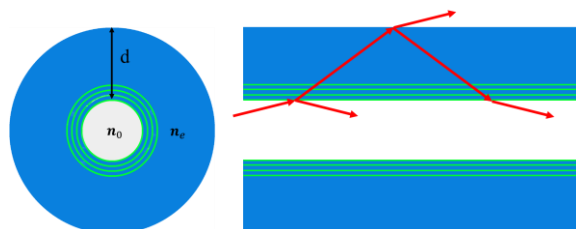


Figure 6.3. The schematic diagram of the guiding mechanism of the HCBF [171].

The guiding mechanism of the HCBF is presented in Figure 6.3. Referring to Figure 6.1(b), the effective refractive index of the air and the cladding are n_0 and n_e (approximately equals to n_1), respectively. With the limited light confining ability of the only four bilayers, the light guided in the core can partially leak out of the Bragg rings and be reflected from the outer surface of the cladding back into the fiber core. This can be explained using the anti-resonant reflecting optical waveguide (ARROW) theory, and the cladding of the HCBF can be regarded as an FP etalon. According to the ARROW model, the light at the anti-resonant wavelength tends to spread out of the cladding that will result

in a loss dip in the transmission spectrum. The anti-resonant wavelength can be expressed as

$$\lambda_m = \frac{2d}{m} \sqrt{n_e^2 - n_0^2} \quad (6.1)$$

where m is an integer, n_e represents the effective refractive index of the cladding and d is the thickness of the cladding. The wavelength far away from the anti-resonant wavelength is called the guided band of HCBF, where the transmission loss is much lower. It is noted that the light intensity guided through the fiber at the guided band depends on the photonic bandgap effect of the Bragg bilayers and the reflectivity of the outer surface. When the reflectivity of the outer surface decreased under specific conditions, the transmission loss in the guided band will become higher. It could be a little confusing between the guiding mechanism and the sensing mechanism. Actually, the sensing mechanism is on the strength of the guiding mechanism. For the proposed HCBF-based sensor, the sensing mechanism is that the amplitude of the guiding mode transmitting in the hollow core can be easily influenced by human breath. Therefore, the guiding mechanism presented is intended to illustrate how the light from lead-in SMF can transmit through the HCBF and thus we can know why the proposed sensor can be used for sensing.

Human breath contains a certain amount of water. When it reaches the HCBF-based sensor, this moisture condenses on the outer surface will form an uneven water film, which will destroy the uniform silica reflecting surface and increase the transmission loss at the guided band. Thus, based on the mechanism, the HCBF sensor can be applied for human breath monitoring by detecting the variation of the transmission intensity in the guided band. In the human breath monitoring experiment, a single frequency laser within the guided band is launched into the fiber, and the transmission light intensity will rise and fall as the breathing progresses.

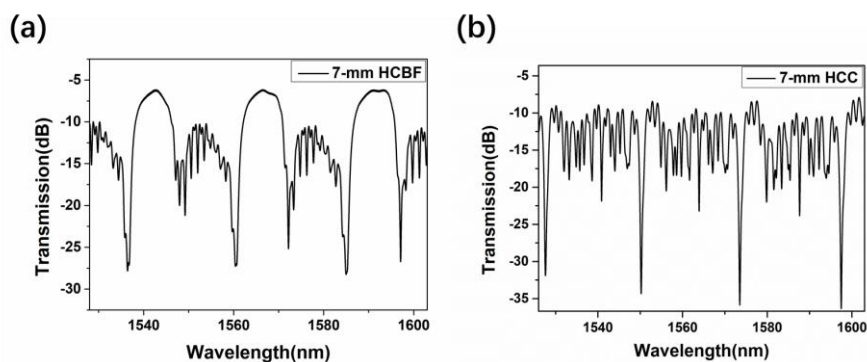


Figure 6.4. The transmission spectra of the (a) HCBF and (b) HCC with both lengths of 7 mm [171].

We have tested the transmission spectrum of the HCBF with the length of 7 mm to study the characteristics of the HCBF, as shown in Figure 6.4(a). Several loss dips in the spectrum are consistent with theoretical analysis based on the ARROW theory. Some ripples in the transmission spectra are caused by the multiple reflections of the guiding light on the inner and outer surfaces of the fiber cladding and the multiple-mode interference. At the wavelength far away from the anti-resonant dips, the loss is obviously lower, which is beneficial from the ARROW mechanism of the cylindrical HCBF and the photonic bandgap effect of the four Bragg bilayers. According to our previous work [172], the minimum loss of the HCBF in the guided band is much lower than that of the hollow core capillary (HCC) with the same size as our fiber. In order to testify the advantages of the Bragg structure, the contrast experiment is carried out. The HCC with inner/outer diameters of 25/125 μm is chosen to form the same structure, and the transmission spectra are illustrated in Figure 6.4(b). The ripples in the transmission spectra of the HCBF are much slighter than those in HCC because more light is confined in the core and less involved in the multiple reflections in the guided band. The flat and smooth guided band in our human breath monitoring experiment is highly advantageous because it can maintain the stability of the transmission light intensity even if the transmission spectrum redshifts/blueshifts with temperature or curvature fluctuation.

6.4 Experimental results and analysis

6.4.1 Experimental setups

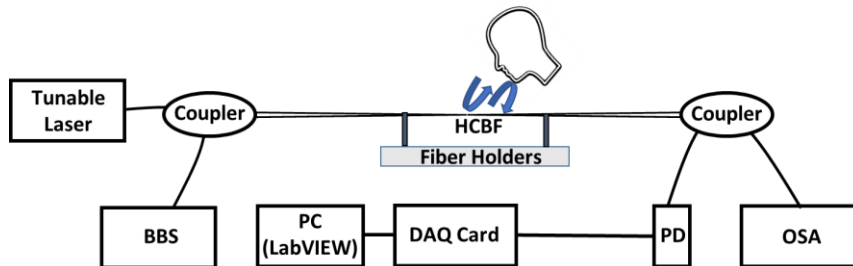


Figure 6.5. The schematic diagram of experimental setups [171].

The schematic diagram of experimental setups is displayed in Figure 6.5. The broadband light source (BBS) has a bandwidth from 1528 nm to 1603 nm with fixed optical power of 10 mW. The tunable laser (TL) can be tuned from 1480 nm to 1640 nm with a power range of 0 – 50 mW. The optical spectrum analyzer (OSA, YOKOGAWA, AQ6374) with the bandwidth of 350 – 1750 nm and resolution of 0.05 nm is used for recording transmission spectra. The photodiode (PD) with 3 dB bandwidth of 3 GHz and Data Acquisition (DAQ) Card with the data acquisition rate of 100 K is employed for electrical signal collection. The optical paths can be divided into two parts: BBS and OSA are applied to analyze optical spectra; TL and PD are used for electrical signal acquisition. The light emitted from BBS and TL can be coupled into the HCBF sensor and received by OSA and PD, respectively. The electrical signals from PD are collected by the DAQ card, which is controlled by LabVIEW on Personal Computer (PC). The collection rate of 1000 Hz and sampling points of 50176 are applied for human breath data collection.

6.4.2 Test on human breath monitoring

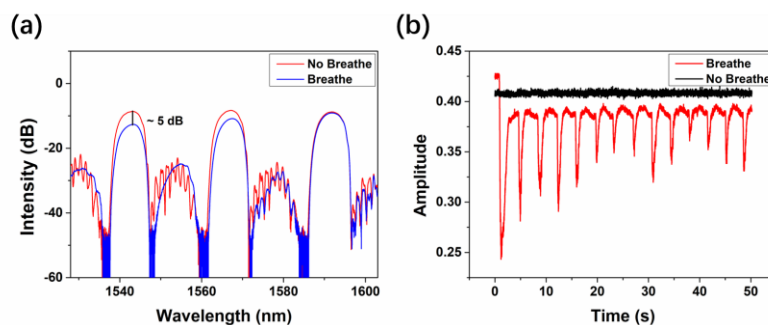


Figure 6.6. (a) The transmission spectra of fiber sensor without breath (red line) and with breath (blue line) and (b) electrical signals without breath (black line) and with breath (red line) [171].

The transmission spectra of the HCBF-based sensor are displayed in Figure 6.6(a). The optical spectrum is collected from 1528 nm to 1603 nm with the resolution of 0.05 nm, and it is seen that three peaks are observed in the measurement range. The red line in Figure 6.6(a) represents the transmission spectrum under the status of no breath at room temperature (RT, 23 – 25 °C), and the blue line shows that in the status of breathing. Obviously, the decrease of peak value at around 1543 nm can be observed when human breathe towards the fiber sensor, which can be attributed to the cladding modes depletion caused by fiber-surface moisture-content change. Thus, the HCBF-based all-fiber sensor can be applied for human breath monitoring based on optical amplitude detection. In addition, it can be observed that there is a slight difference of transmission intensity at the third peak in Figure 6.6(a) between breath and no breath, which is due to the recovery of moisture-content condition on the fiber surface. As seen from Figure 6.6(b), the electrical signals of experimental results on human breath monitoring are presented that the black line indicates the collected signals without breath and the red line represents that with human breath. The TL at 1543 nm with a power of 1 mW is utilized as the light source. The laser will transmit through the HCBF and be collected by the PD and DAQ card controlled by LabVIEW. It can be observed that breath signals are explicitly revealed with 14 times breathing in 50 s and breath interval of around 3.5 s, according with results recorded

through human-eye observation.

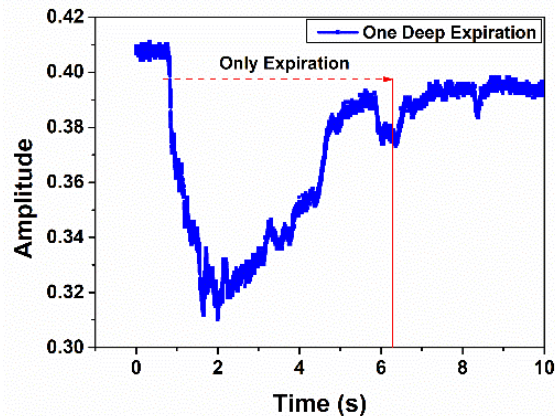


Figure 6.7. Breath signal with one deep expiration [171].

To analyze the relationship between breath and electrical signals, the experiment of one deep expiration was conducted, which is shown in Figure 6.7. As generally known, a breathing process can be split into inspiration and expiration, and it is readily comprehensible that inspiration makes a slight impact on moisture change. As the human breath monitoring in this work is based on moisture-content detection, inspiration can be seemed as the recovery process of breath sensing. Expiration has a powerful influence on moisture around the fiber sensor so that the experimenter kept one deep expiration (lasting for around 6 s) towards the sensor for the signal catch. As can be seen from Figure 6.7, the signal declines rapidly in the first 2 s, which can be explained by the decrease of light transmission due to moisture rising induced cladding modes dissipation. In this process, the moisture increasing caused by expiration is stronger than moisture decreasing caused by evaporation of water molecules. In 2 – 6 s, although the experimenter continues expiration, the signal is reversely enhanced, which can be interpreted that the evaporation process becomes dominant.

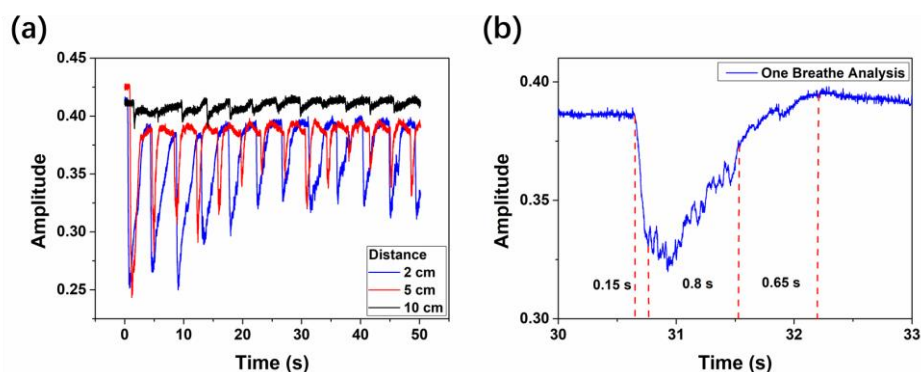


Figure 6.8. (a) Electrical signals with different distances between the human face and fiber sensor at 2 cm, 5 cm, and 10 cm and (b) response time of human breath monitoring [171].

In addition, the distance between the human face and fiber sensor is studied to investigate its influence on sensing performance. As can be seen from Figure 6.8(a), different distances of 2 cm, 5 cm, 10 cm are set for data recording. The blue line represents the breath signals detected at the distance of 2 cm, and the red line shows the sensing results at 5-cm distance. It is clear that there are slight differences between the two sets of signals. However, as the distance is increased to 10 cm, the amplitude of breath signals decline remarkably, which is shown as the black line. Although the 10-cm breath signals can still be distinguished, the weak amplitude will lead to measurement errors with a high probability. Considering this, the effective distance of the HCBF-based sensor used for human breath monitoring is less than 10 cm. Figure 6.8(b) shows the response time of the fiber sensor. Based on the data analysis in Fig 6.7, the one breath signal can be divided into three parts. The ~ 0.15 s time slot represents the rapid-declining process of signal amplitude induced by human expiration. Then the amplitude of the signal fluctuates and recovers in the next ~ 0.8 s until the end of the expiration process. After that, the sensor is completely recovered in the next ~ 0.65 s within the process of human inspiration. Thus, the response time of the fiber sensor is measured to be around 0.15 s.

6.4.3 Test on temperature and curvature sensitivity

For all-fiber sensors used for human breath monitoring, the temperature and curvature will be the nonnegligible factors that may lead to significant measurement errors on sensing results. In view of this, further experiments are conducted to investigate the potential impacts of temperature and curvature on the proposed sensor structure. The fiber sensor was located in the temperature chamber with a resolution of 0.1 °C for temperature sensing. The BBS and OSA served as the light source and spectra recorder, respectively.

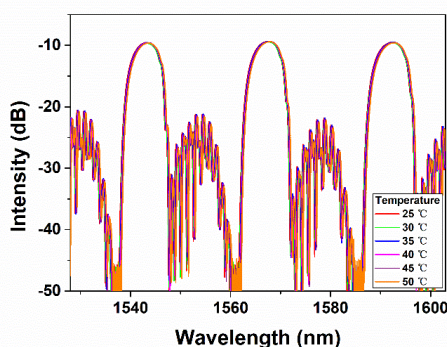


Figure 6.9. The transmission spectra of fiber sensor at different temperatures of 25 °C, 30 °C, 35 °C, 40 °C, 45 °C, 50 °C [171].

Figure 6.9 displays the transmission spectra of HCBF based sensor at different temperatures of 25 °C, 30 °C, 35 °C, 40 °C, 45 °C, 50 °C. Evidently, the transmission spectra at different temperatures approximately maintain the same waveshapes but with a slight redshift. The details of the transmission peak at 1543 nm are shown in Figure 6.10(a). It is distinct that the light intensity at 1543 nm, which is the applied wavelength of TL for breath signal recording, is almost unchanged. The fluctuation of peak values keeps within 0.17 dB in the temperature range of 25 – 50 °C, as shown in Figure 6.10(b), which is negligible compared to the 5 dB variation induced by human breath. Hence, the proposed all-fiber sensor used for human breath monitoring can be considered temperature insensitive. In

addition, the sensor can also be used for temperature sensing based on the wavelength shift, which is induced by the difference of RI change between Ge-doped high-index layers and low-index layers. Figure 6.10(c) presents the relationship between temperature change and wavelength variation at the interference dip of 1550 nm. The sensitivity is measured to be 16.5 pm/°C with the adjusted R-square value of 0.9983.

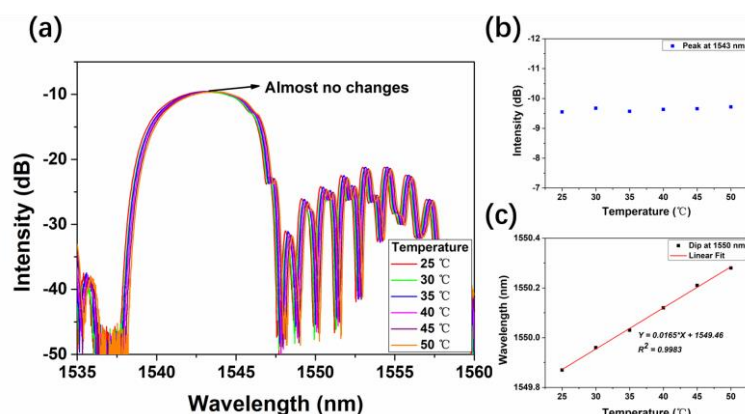


Figure 6.10. (a) The details of transmission spectra at different temperatures of 25 °C, 30 °C, 35 °C, 40 °C, 45 °C, 50 °C, (b) the peak intensities statistics at different temperatures and (c) the relationship between temperature and dip (1550 nm) wavelength [171].

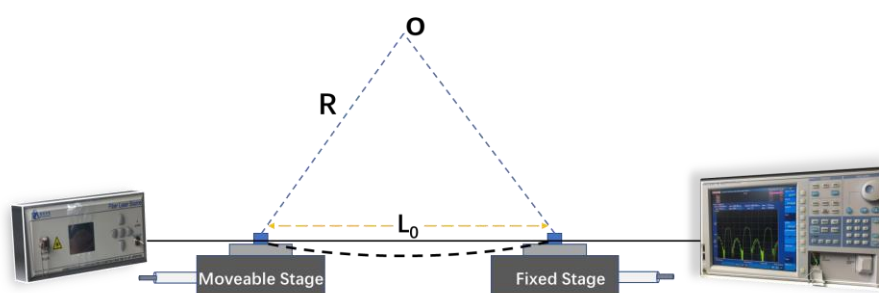


Figure 6.11. The schematic diagram of the experimental setup for curvature sensing [171].

As shown in Figure 6.11, the experiment on curvature sensing can be conducted by fixing the fiber sensor on two translation stages (one is fixed, and the other one is moveable). By tuning the moveable translation station with a step of 20 μm , different curvature values can be achieved. In general, the curvature can be calculated by the equation shown below [138]:

$$C = \frac{1}{R} \cong \sqrt{\frac{24x}{L_0^3}} \quad (6.2)$$

where C represents the curvature value, R refers to the bending radius, x is the displacement of the moveable stage, and L_0 (8.5 cm) is the fiber length between two fiber holders when the fiber is straight.

The experimental results of curvature sensing are presented in Figure 6.12(a) that the transmission spectra are monitored and saved for comparison at different steps. The curvature values are set as 0, 0.8841, 1.5313, 1.9769, 2.7957, 3.4240, 3.9537, 4.4204 m^{-1} , respectively. It is evident that the transmission spectra show slight variations at different bending degrees. To reveal transmission intensity change induced by the bending, the relationship between curvature values and peak intensity at 1543 nm is displayed in Figure 6.12(b). Compared to the 5 dB variation caused by human breath, the curvature-induced fluctuation of transmission intensity at 1543 nm is much smaller with a value less than 0.353 dB. Thus, the all-fiber sensor based on HCBF can be considered as a curvature-insensitive device for human breath monitoring. The comparisons of overall sensing performances between our sensor and previously reported sensors are shown in Table 6.1.

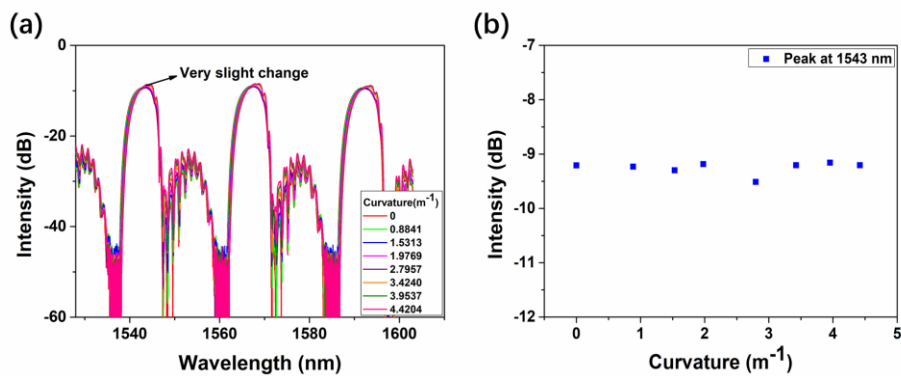


Figure 6.12. (a) The transmission spectra of fiber sensor with different curvature values of 0, 0.8841, 1.5313, 1.9769, 2.7957, 3.4240, 3.9537, 4.4204 m^{-1} and (b) the peak intensities statistics at different curvature values [171].

Table 6.1. Comparison of the key parameters between the proposed all-fiber sensor and other recent-developed fiber-optic sensors in literatures for human breath monitoring [171]

Sensor Structure	Response Time (s)	Recovery Time (s)	Temperature Insensitivity	Curvature Insensitivity
Fiber + hygroscopic polymer [163]	0.5	0.4	Not mentioned	Not mentioned
Fiber + PEO [79]	0.785	Not mentioned	Not mentioned	No
Fiber + MoS ₂ [164]	0.85	0.85	Not mentioned	Not mentioned
Fiber + MoS ₂ [174]	0.066	2.395	Not mentioned	Not mentioned
Fiber + SnO ₂ [165]	0.37	0.37	No	Not mentioned
Fiber + GO [166]	0.042	0.115	No	Not mentioned
Fiber + gelatin [167]	0.084	0.029	Yes	Not mentioned
All-fiber (This work)	0.15	0.65	Yes	Yes

6.5 Discussion

It should be noted that the proposed sensor is not entirely based on the explanation of humidity, but the moisture content brought by breath. The human breath is accompanied by temperature change and irregular airflow so that the water vapor brought by human breath will show an irregular process of increasing or decreasing. The sensor based on humidity is very sensitive, which will in reverse lead to a larger cross response to temperature and humidity. To a certain extent, our sensor is not as extremely sensitive as other works mentioned before. However, combining with the test results, the sensitivity of the sensor for breath monitoring is sufficient to detect and analyze the breathing process. In addition,

this makes our sensor more stable in different environments.

We also do the comparison experiment by controlling variables. It is supposed that the possible influence factors of human breath on fiber sensors could be temperature, curvature, vibration and moisture content. We have done the tests of temperature and curvature and the experimental results indicate that the sensor is insensitive to temperature and curvature. Vibration is also one of the very important factors that need to be considered. In the experiment, we actually utilize a rubber air blower to simulate the vibration induced by human breath and no changes are observed from the optical spectrum and electrical signals. The difference between human breath and rubber air blower can be moisture and temperature and further experiments on temperature sensing demonstrate that the proposed sensor is insensitive to temperature change. Thus, we can make sure that the variation of output signals is induced by moisture change brought by human breath but not temperature, curvature, or vibration.

In addition, we think that the experiment of close human breath is different from the humidity test in the chamber. Firstly, the human breath is accompanied by temperature change and irregular airflow so that the water vapor brought by human breath will show an irregular process of increasing or decreasing. Combining the experimental results and observation, we conclude that the moisture content will increase dramatically, reach saturation and then decrease rapidly because of the airflow. The human breath is a dynamic process that will result in a much higher concentration of water vapor compared to that in the humidity chamber.

We also do the humidity experiment in a humidity chamber, which can provide the normal ranges of humidity but found that the effect was much smaller compared to that induced by human breath. Actually, the sensor designed to monitor the human breath is immobilized in the inner surface of a face mask, so the distance between the sensor and the

mouth is set as several centimeters. It is noted that, in our experiment, the concentration of water vapor brought by close breathing is far greater than the influence of air humidity, which is easy to understand by putting your palms in front of your mouth and breathing. By analyzing the experimental result, we believe the condensation of water vapor in the dynamic process of human breath is more suitable to explain the principle of our sensor but not the simple humidity change.

6.6 Conclusion

An all-fiber sensor based on HCBF has been successfully created in this work which displays excellent performance on human breath monitoring. The response time of the proposed sensor is around 0.15 s which enables the rapid and precise recording of breath signals. The applied distance between the fiber sensor and the human face is also investigated to reveal its influences on sensing results. Moreover, the HCBF sensor proves substantial insensitivity to temperature and curvature variation, which demonstrates its reliable sensing performance in different application environments. The proposed all-fiber sensor has advantages of low price, ease of fabrication, and insensitivity to the change of temperature and curvature, which provides a creative and reliable approach to human breath monitoring.

7 Conclusions and Suggestions for Future Research

In this chapter, the conclusions of the aforementioned research results are given. And also, the extension of the previous works and more potential applications of the aforementioned fiber sensors are presented.

7.1 Conclusions

In the thesis, we study the various applications of novel structured fibers for optical communication and sensing devices. The light modulators assisted with 2D materials are introduced. The mechanism of 2D materials-based light modulation and modulators with different fiber structures are presented. The performances of the proposed and successfully fabricated light modulator are studied and improved, and the analysis of experimental results is included. The experimental results demonstrate a feasible method for all-optical light modulation with a down-tapered fiber structure assisted with graphene nanoflakes. The measured response time is about 0.4 ns, indicating the potential for optical signal processing with the bandwidth of up to 2.5 GHz.

Then, the fiber sensors are introduced including characteristics of fiber sensors, different sensing principles and various physical structures. The fiber sensors are constructed by different structures, including mismatched single-mode fibers, ring-core fiber and hollow core Bragg fiber. The proposed sensors can be applied in various fields of sensing including temperature, humidity, refractive index, curvature and human breath. Firstly, a fiber sensor based on mismatched SMFs is proposed and experimentally demonstrated which indicates good application on sensing of temperature and humidity based on cladding modes modulation. With CNT attached to the fiber, the sensitivity of temperature detection in small ranges is enhanced from 0.24561 to 1.65282 dB/°C, and the humidity sensing becomes more reliable for real application. Secondly, the fiber sensor based on MZI composed of SMF-NCF-RCF-SMF structure is successfully achieved. The experiments on temperature, RI and curvature sensing are conducted. Dual demodulation of temperature and RI can be realized with the temperature variation under 20 °C and RI resolution of 0.01 ranging from 1.33 to 1.38. The maximum sensitivity of temperature

sensing is 69 pm/°C and that of RI sensing reaches 182.07 dB/RIU and -31.44 nm/RIU with the intensity and wavelength demodulation methods, respectively. The maximum sensitivity of curvature sensing is -3.68 nm/m⁻¹ and the adjusted R square value reaches 0.9959 within the measurement range of 1.3856 to 3.6661 m⁻¹. Two interference dips around 1587 nm and 1642 nm are selected for data analysis. Based on the linear relationship between dip wavelength shift with the variation of temperature and curvature, these two parameters can be simultaneously demodulated by using the 2 × 2 matrix. Thirdly, an all-fiber sensor based on HCBF has been successfully created which displays excellent performance on human breath monitoring. The response time of the proposed sensor is around 0.15 s which enables the rapid and precise recording of breath signals. The applied distance between the fiber sensor and the human face is also investigated to reveal its influences on sensing results. Moreover, the HCBF sensor proves substantial insensitivity to temperature and curvature variation, which demonstrates its reliable sensing performance in different application environments.

The all-fiber-based light modulator and fiber sensors are investigated and the research will play a very important part in optical communication networks and sensing systems to simplify the structures and enrich the functionality of optical components. The works presented in the thesis will also be beneficial to explore the novel applications of fibers with different configurations.

7.2 Suggestions for future research

Based on the current research outcomes, it is planned to do the extensive investigation on light modulators and fiber sensors.

For light modulators, we currently focused on the all-optical modulation method

assisted with graphene materials which can theoretically provide a high modulation speed. However, there are still some defects that will have a great impact on its practical applications. The all-optical modulation method is mostly based on the tapered SMF ($\sim 1 \mu\text{m}$ diameter) which is very fragile compared to traditional fiber structures. The structure of the light modulator can easily be broken down by external environment changes, such as temperature (that will lead to structural expansion and contraction), vibration and so on. Thus, the fragile construction of such light modulator will bring large difficulty to its real application. The electro-optical modulation method could be the solution to this kind of problem.

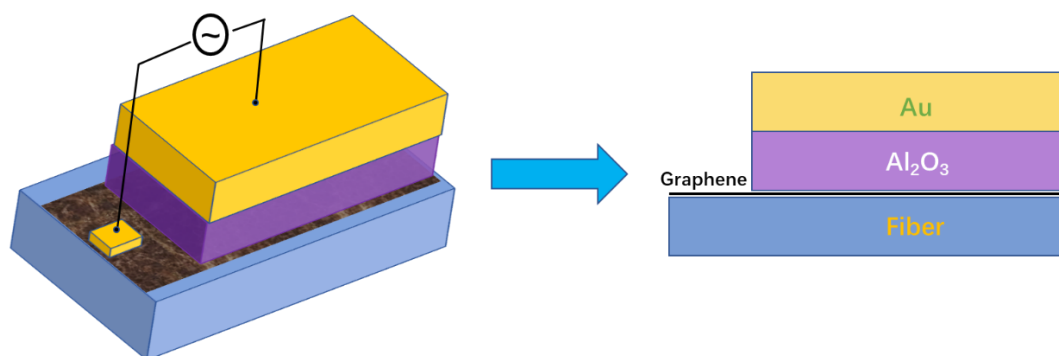


Figure 7.1. Schematic diagram of electrically controlled graphene-based electro-optical modulator.

A capacitor is designed for the electro-optical modulator in order to actively control the RI of graphene, which is shown in Figure 7.1. The capacitor is of the sandwich structure which includes three parts: graphene layer, Al_2O_3 dielectric layer and the electrode layer (Au) [30, 31, 175-177]. The gold electrode can be fabricated by a thermal evaporation device and the Al_2O_3 dielectric layer can be achieved by using the atomic layer deposition (ALD) system. The thickness of the dielectric layer is designed to be 30 nm to make sure of the large capacity so that small voltage can be used to accumulate a mass of electrons on graphene layer. The free carriers on the graphene layer will give rise to the change of graphene's chemical potential, which is also known as Fermi Level. The Fermi Level will determine the optical conductivity of graphene which can further influence the RI of

graphene. The functions are shown in Equation (7.1) (7.2) (7.3) [178]:

$$n_s = \frac{2}{\pi \hbar^2 v_F^2} \int_0^\infty \varepsilon [f_d(\varepsilon) - f_d(\varepsilon + 2\mu_c)] d\varepsilon \quad (7.1)$$

$$\sigma(\omega, \mu_c, \Gamma, T) = \frac{-je^2(\omega + j2\Gamma)}{\pi \hbar^2} \left[\int_0^\infty \varepsilon \left(\frac{\partial f_d(\varepsilon)}{\partial \varepsilon} - \frac{\partial f_d(-\varepsilon)}{\partial \varepsilon} \right) d\varepsilon - \int_0^\infty \left(\frac{f_d(-\varepsilon) - f_d(\varepsilon)}{(\omega + j2\Gamma)^2 - 4(\varepsilon/\hbar)^2} \right) d\varepsilon \right] \quad (7.2)$$

$$n_g = (\varepsilon_g)^{1/2} = \left(1 + \frac{j\sigma}{\varepsilon_0 \omega t_g} \right)^{1/2} \quad (7.3)$$

where n_s means the carrier density, v_F is the Fermi velocity, \hbar is the reduced Plank's constant, ε represents energy, $f_d(\varepsilon)$ is the Fermi-Dirac distribution, ω is the radian frequency, μ_c is the chemical potential, Γ means the scattering rate, T is the temperature, n_g is the refractive index of graphene, ε_g is the relative permittivity of graphene, t_g is the thickness of graphene, ε_0 is the permittivity of free space. Thus, the usage of alternating current can realize the fast carriers' accumulation and dispersion on the graphene layer which will implement the alteration of graphene's RI. Based on this mechanism, the Mach-Zehnder interferometer can transform phase change to intensity change and ultimately achieve light modulation.

For fiber sensors, we have introduced a number of fibers (such as FMF, MMF, capillary, RCF, HCBF) and fiber structures (such as MZI, FPI, Michelson interferometer, Sagnac interferometer) used for multiple parameters sensing. In our works, most of the experiments on fiber sensing are conducted by utilizing the properties of the fiber itself (SiO_2 material). For example, the proposed MZI-based sensor composed of SMF-NCF-RCF-SMF structure can be applied for sensing temperature, RI and curvature. All the parameters can be measured by detecting the variation of light transmittance in the fiber sensor which can be attributed to environment-induced alteration of fiber characteristics, such as RI distribution, length, etc. However, to some extent, SiO_2 may not be the optimal

material for measuring different factors. For example, the thermal expansion coefficient and thermo-optic coefficient of SiO₂ are relatively small which means that the temperature sensitivity of all-fiber sensors is relatively low. Thus, in order to improve the sensitivity of fiber sensors, many kinds of materials with a larger thermal expansion or thermo-optic coefficient can be used as the coater or filler, such as polydimethylsiloxane (PDMS), polyimide or graphene material. In addition, under some circumstances, the material combination could be indispensable for fiber sensors, such as the measurement of the magnetic field, as SiO₂ has no response to the variation of the magnetic field.

Therefore, future work can be focused on materials-assisted fiber sensors to develop extensive and practical applications. The packaging technique is also an important problem we should attach importance to because materials-assisted fiber sensors may confront a big problem of sensor instability which can be caused by materials alteration or loose combination due to temperature change or chemical corrosion. By considering both advantages and disadvantages of materials combination, a variety of fiber sensors coated with materials can be developed which will bring a new milestone for the application of optical fiber sensing.

Bibliography

1. S. Iijima, "Helical microtubules of graphitic carbon," *Nature* **354**, 56–58 (1991).
2. J. H. H. Kroto, S. O'Brien, R. Curl and R. Smalley, , " C60: Buckminsterfullerene," *Nature* **318**, 162– 163 (1985).
3. A. G. K. Novoselov, S. Morozov, D. Jiang, Y. Zhang, S. Dubonos, I. Grigorieva and A. Firsov, "Electric Field Effect in Atomically Thin Carbon Films," *Science* **306**, 666–669 (2004).
4. C. Soldano, A. Mahmood, and E. Dujardin, "Production, properties and potential of graphene," *Carbon* **48**, 2127-2150 (2010).
5. V. Singh, D. Joung, L. Zhai, S. Das, S. I. Khondaker, and S. Seal, "Graphene based materials: Past, present and future," *Progress in Materials Science* **56**, 1178-1271 (2011).
6. X. W. C. LEE, J. W. KYSAR, and J. HONE, "Measurement of the Elastic Properties and Intrinsic Strength of Monolayer Graphene," *Science* 2008, pp. 385–388.
7. E. H. Hwang and S. Das Sarma, "Acoustic phonon scattering limited carrier mobility in two-dimensional extrinsic graphene," *Physical Review B* **77**(2008).
8. S. G. A. Balandin, W. Bao, I. Calizo, D. Teweldebrhan, F. Miao, and C. Lau, , "Superior Thermal Conductivity of Single-Layer Graphene," *Nano letters* **8**, 902–907 (2008).
9. D. J. K. Novoselov, B. Zhang, S. Morozov, H. Stormer, U. Zeitler, J. Maan, G. Boebinger, P. Kim and A. Geim,, "Room-Temperature Quantum Hall Effect in Graphene," *Science* **315**, 1379–1379 (2007).
10. Y. H. Y. Wang, Y. Song, X. Zhang, Y. Ma, J. Liang and Y. Chen,, "Room-Temperature Ferromagnetism of Graphene," *Nano letters* **9**, 220–224 (2009).
11. P. Avouris, "Graphene: electronic and photonic properties and devices," *Nano Lett* **10**, 4285-4294 (2010).
12. F. Bonaccorso, Z. Sun, T. Hasan, and A. C. Ferrari, "Graphene photonics and optoelectronics," *Nature Photonics* **4**, 611-622 (2010).
13. S. Y. Zhou, G. H. Gweon, J. Graf, A. V. Fedorov, C. D. Spataru, R. D. Diehl, Y. Kopelevich, D. H. Lee, S. G. Louie, and A. Lanzara, "First direct observation of Dirac fermions in graphite," *Nature Physics* **2**, 595-599 (2006).
14. S. Yu, X. Wu, Y. Wang, X. Guo, and L. Tong, "2D Materials for Optical Modulation: Challenges and Opportunities," *Adv Mater* **29**(2017).
15. K. Kim, J. Y. Choi, T. Kim, S. H. Cho, and H. J. Chung, "A role for graphene in silicon-based semiconductor devices," *Nature* **479**, 338-344 (2011).
16. N. Youngblood, Y. Anugrah, R. Ma, S. J. Koester, and M. Li, "Multifunctional graphene optical modulator and photodetector integrated on silicon waveguides," *Nano Lett* **14**, 2741-2746 (2014).

17. C. T. Phare, Y.-H. Daniel Lee, J. Cardenas, and M. Lipson, "Graphene electro-optic modulator with 30 GHz bandwidth," *Nature Photonics* **9**, 511-514 (2015).
18. Q. Bao, H. Zhang, Y. Wang, Z. Ni, Y. Yan, Z. X. Shen, K. P. Loh, and D. Y. Tang, "Atomic-Layer Graphene as a Saturable Absorber for Ultrafast Pulsed Lasers," *Advanced Functional Materials* **19**, 3077-3083 (2009).
19. W. Li, B. Chen, C. Meng, W. Fang, Y. Xiao, X. Li, Z. Hu, Y. Xu, L. Tong, H. Wang, W. Liu, J. Bao, and Y. R. Shen, "Ultrafast all-optical graphene modulator," *Nano Lett* **14**, 955-959 (2014).
20. S. Yu, X. Wu, K. Chen, B. Chen, X. Guo, D. Dai, L. Tong, W. Liu, and Y. Ron Shen, "All-optical graphene modulator based on optical Kerr phase shift," *Optica* **3** (2016).
21. X. Gan, C. Zhao, Y. Wang, D. Mao, L. Fang, L. Han, and J. Zhao, "Graphene-assisted all-fiber phase shifter and switching," *Optica* **2**(2015).
22. F. Xia, H. Wang, D. Xiao, M. Dubey, and A. Ramasubramaniam, "Two-dimensional material nanophotonics," *Nature Photonics* **8**, 899-907 (2014).
23. Z. Sun, A. Martinez, and F. Wang, "Optical modulators with 2D layered materials," *Nature Photonics* **10**, 227-238 (2016).
24. M. Zhang, Q. Wu, F. Zhang, L. Chen, X. Jin, Y. Hu, Z. Zheng, and H. Zhang, "2D Black Phosphorus Saturable Absorbers for Ultrafast Photonics," *Advanced Optical Materials* **7**(2019).
25. S. J. Koester and M. Li, "High-speed waveguide-coupled graphene-on-graphene optical modulators," *Applied Physics Letters* **100**(2012).
26. R. Hao, J. Jin, X. Wei, X. Jin, X. Zhang, and E. Li, "Recent developments in graphene-based optical modulators," *Frontiers of Optoelectronics* **7**, 277-292 (2014).
27. S. Yu, C. Meng, B. Chen, H. Wang, X. Wu, W. Liu, S. Zhang, Y. Liu, Y. Su, and L. Tong, "Graphene decorated microfiber for ultrafast optical modulation," *Opt Express* **23**, 10764-10770 (2015).
28. E. J. Lee, S. Y. Choi, H. Jeong, N. H. Park, W. Yim, M. H. Kim, J. K. Park, S. Son, S. Bae, S. J. Kim, K. Lee, Y. H. Ahn, K. J. Ahn, B. H. Hong, J. Y. Park, F. Rotermund, and D. I. Yeom, "Active control of all-fibre graphene devices with electrical gating," *Nat Commun* **6**, 6851 (2015).
29. M. Liu, X. Yin, E. Ulin-Avila, B. Geng, T. Zentgraf, L. Ju, F. Wang, and X. Zhang, "A graphene-based broadband optical modulator," *Nature* **474**, 64-67 (2011).
30. M. G. Wood, S. Campione, S. Parameswaran, T. S. Luk, J. R. Wendt, D. K. Serkland, and G. A. Keeler, "Gigahertz speed operation of epsilon-near-zero silicon photonic modulators," *Optica* **5**(2018).
31. V. Soriano, M. Midrio, G. Contestabile, I. Asselberghs, J. Van Campenhout, C. Huyghebaert, I. Goykhman, A. K. Ott, A. C. Ferrari, and M. Romagnoli, "Graphene-silicon phase modulators with gigahertz bandwidth," *Nature Photonics* **12**, 40-44 (2017).
32. M. K. Shah, S.-W. Ye, X.-H. Zou, F. Yuan, A. Jha, Y. Zhang, R.-G. Lu, and Y. Liu, "Graphene-Assisted Electroabsorption Optical Modulator Using D-Microfiber," *IEEE Journal of Selected Topics in Quantum Electronics* **23**, 89-93 (2017).
33. R. Amin, J. B. Khurgin, and V. J. Sorger, "Waveguide-based electro-absorption modulator performance: comparative analysis," *Opt Express* **26**, 15445-15470 (2018).

BIBLIOGRAPHY

34. E. Dremetsika, B. Dlubak, S. P. Gorza, C. Ciret, M. B. Martin, S. Hofmann, P. Seneor, D. Dolfi, S. Massar, P. Emplit, and P. Kockaert, "Measuring the nonlinear refractive index of graphene using the optical Kerr effect method," *Opt Lett* **41**, 3281-3284 (2016).
35. N. A. Savostianova and S. A. Mikhailov, "Optical Kerr effect in graphene: Theoretical analysis of the optical heterodyne detection technique," *Physical Review B* **97**(2018).
36. N. Vermeulen, D. Castello-Lurbe, M. Khoder, I. Pasternak, A. Krajewska, T. Ciuk, W. Strupinski, J. Cheng, H. Thienpont, and J. Van Erps, "Graphene's nonlinear-optical physics revealed through exponentially growing self-phase modulation," *Nat Commun* **9**, 2675 (2018).
37. F. Zhou, R. Hao, X.-F. Jin, X.-M. Zhang, and E.-P. Li, "A Graphene-Enhanced Fiber-Optic Phase Modulator With Large Linear Dynamic Range," *IEEE Photonics Technology Letters* **26**, 1867-1870 (2014).
38. Q. Kuang, C. Lao, Z. L. Wang, Z. Xie, and L. Zheng, "High-sensitivity humidity sensor based on a single SnO(2) nanowire," *J Am Chem Soc* **129**, 6070-6071 (2007).
39. Q. Qi, T. Zhang, Q. Yu, R. Wang, Y. Zeng, L. Liu, and H. Yang, "Properties of humidity sensing ZnO nanorods-base sensor fabricated by screen-printing," *Sensors and Actuators B: Chemical* **133**, 638-643 (2008).
40. F. Vetrone, R. Naccache, A. Zamarron, A. Juarranz de la Fuente, F. Sanz-Rodriguez, L. Martinez Maestro, E. Martin Rodriguez, D. Jaque, J. Garcia Sole, and J. A. Capobianco, "Temperature sensing using fluorescent nanothermometers," *ACS Nano* **4**, 3254-3258 (2010).
41. D. Zhang, H. Chang, P. Li, R. Liu, and Q. Xue, "Fabrication and characterization of an ultrasensitive humidity sensor based on metal oxide/graphene hybrid nanocomposite," *Sensors and Actuators B: Chemical* **225**, 233-240 (2016).
42. M. Wang, D. Zhang, A. Yang, D. Wang, and X. Zong, "Fabrication of polypyrrole/graphene oxide hybrid nanocomposite for ultrasensitive humidity sensing with unprecedented sensitivity," *Journal of Materials Science: Materials in Electronics* **30**, 4967-4976 (2019).
43. S. M. Borisov, A. S. Vasylevska, C. Krause, and O. S. Wolfbeis, "Composite Luminescent Material for Dual Sensing of Oxygen and Temperature," *Advanced Functional Materials* **16**, 1536-1542 (2006).
44. F. Ye, C. Wu, Y. Jin, Y. H. Chan, X. Zhang, and D. T. Chiu, "Ratiometric temperature sensing with semiconducting polymer dots," *J Am Chem Soc* **133**, 8146-8149 (2011).
45. E. S. Araújo, J. Libardi, P. M. Faia, and H. P. de Oliveira, "Humidity-sensing properties of hierarchical TiO₂:ZnO composite grown on electrospun fibers," *Journal of Materials Science: Materials in Electronics* **28**, 16575-16583 (2017).
46. E. S. Araújo and V. N. S. Leão, "TiO₂/WO₃ heterogeneous structures prepared by electrospinning and sintering steps: Characterization and analysis of the impedance variation to humidity," *Journal of Advanced Ceramics* **8**, 238-246 (2019).
47. T. Kurashima, T. Horiguchi, and M. Tateda, "Distributed-Temperature Sensing Using Stimulated Brillouin-Scattering in Optical Silica Fibers," *Optics Letters* **15**, 1038-1040 (1990).
48. M. Sibinski, M. Jakubowska, and M. Sloma, "Flexible temperature sensors on fibers," *Sensors (Basel)* **10**, 7934-7946 (2010).

49. T. G. Giallorenzi, J. A. Bucaro, A. Dandridge, G. H. Sigel, J. H. Cole, S. C. Rashleigh, and R. G. Priest, "Optical Fiber Sensor Technology," *Ieee Journal of Quantum Electronics* **18**, 626-665 (1982).
50. B. Culshaw, "Optical Fiber Sensor Technologies: Opportunities and—Perhaps—Pitfalls," *Journal of Lightwave Technology* **22**, 39-50 (2004).
51. A. I. Gusarov, F. Berghmans, O. DeParis, A. F. Fernandez, Y. Defosse, P. Megret, M. Decreton, and M. Blondel, "High total dose radiation effects on temperature sensing fiber Bragg gratings," *Ieee Photonics Technology Letters* **11**, 1159-1161 (1999).
52. Y. C. Tan, W. B. Ji, V. Mamidala, K. K. Chow, and S. C. Tjin, "Carbon-nanotube-deposited long period fiber grating for continuous refractive index sensor applications," *Sensors and Actuators B: Chemical* **196**, 260-264 (2014).
53. Y. Huang, W. Zhu, Z. Li, G. Chen, L. Chen, J. Zhou, H. Lin, J. Guan, W. Fang, X. Liu, H. Dong, J. Tang, H. Guan, H. Lu, Y. Xiao, J. Zhang, H. Wang, Z. Chen, and J. Yu, "High-performance fibre-optic humidity sensor based on a side-polished fibre wavelength selectively coupled with graphene oxide film," *Sensors and Actuators B: Chemical* **255**, 57-69 (2018).
54. Y. Zhao, R.-j. Tong, M.-Q. Chen, and F. Xia, "Relative humidity sensor based on hollow core fiber filled with GQDs-PVA," *Sensors and Actuators B: Chemical* **284**, 96-102 (2019).
55. S. M. Tripathi, A. Kumar, R. K. Varshney, Y. B. P. Kumar, E. Marin, and J. P. Meunier, "Strain and Temperature Sensing Characteristics of Single-Mode–Multimode–Single-Mode Structures," *Journal of Lightwave Technology* **27**, 2348-2356 (2009).
56. L. Jiang, J. Yang, S. Wang, B. Li, and M. Wang, "Fiber Mach-Zehnder interferometer based on microcavities for high-temperature sensing with high sensitivity," *Optics Letters* **36**, 3753-3755 (2011).
57. L. H. Chen, T. Li, C. C. Chan, R. Menon, P. Balamurali, M. Shailender, B. Neu, X. M. Ang, P. Zu, W. C. Wong, and K. C. Leong, "Chitosan based fiber-optic Fabry–Perot humidity sensor," *Sensors and Actuators B: Chemical* **169**, 167-172 (2012).
58. B. Dong, B. Zhang, J. Ng, Y. Wang, and C. Yu, "Ultrahigh-Sensitivity Fiber Acoustic Sensor With a Dual Cladding Modes Fiber Up-Taper Interferometer," *IEEE Photonics Technology Letters* **27**, 2234-2237 (2015).
59. B. Dong, Y. Ge, Y. Wang, and C. Yu, "High extinction-ratio dual thin-taper fiber interferometer fabricated by arc-discharge and its performance as sensors," *Optics Communications* **355**, 225-229 (2015).
60. L. V. Nguyen, D. Hwang, S. Moon, D. S. Moon, and Y. J. Chung, "High temperature fiber sensor with high sensitivity based on core diameter mismatch," *Optics Express* **16**, 11369-11375 (2008).
61. M. F. L. De Volder, S. H. Tawfick, R. H. Baughman, and A. J. Hart, "Carbon Nanotubes: Present and Future Commercial Applications," *Science* **339**, 535-539 (2013).
62. J. N. Coleman, U. Khan, W. J. Blau, and Y. K. Gun'ko, "Small but strong: A review of the mechanical properties of carbon nanotube–polymer composites," *Carbon* **44**, 1624-1652 (2006).

BIBLIOGRAPHY

63. A. Modi, N. Koratkar, E. Lass, B. Q. Wei, and P. M. Ajayan, "Miniaturized gas ionization sensors using carbon nanotubes," *Nature* **424**, 171-174 (2003).
64. J.-W. Han, B. Kim, J. Li, and M. Meyyappan, "Carbon Nanotube Based Humidity Sensor on Cellulose Paper," *The Journal of Physical Chemistry C* **116**, 22094-22097 (2012).
65. W. Qiu, Q. Li, Z.-K. Lei, Q.-H. Qin, W.-L. Deng, and Y.-L. Kang, "The use of a carbon nanotube sensor for measuring strain by micro-Raman spectroscopy," *Carbon* **53**, 161-168 (2013).
66. A. Abdelhalim, M. Winkler, F. Loghin, C. Zeiser, P. Lugli, and A. Abdellah, "Highly sensitive and selective carbon nanotube-based gas sensor arrays functionalized with different metallic nanoparticles," *Sensors and Actuators B: Chemical* **220**, 1288-1296 (2015).
67. S. Ryu, P. Lee, J. B. Chou, R. Z. Xu, R. Zhao, A. J. Hart, and S. G. Kim, "Extremely Elastic Wearable Carbon Nanotube Fiber Strain Sensor for Monitoring of Human Motion," *Acs Nano* **9**, 5929-5936 (2015).
68. W. Yuan, H. Qian, Y. Liu, Z. Wang, and C. Yu, "Highly Sensitive Temperature and Humidity Sensor Based on Carbon Nanotube-Assisted Mismatched Single-Mode Fiber Structure," *Micromachines (Basel)* **10**(2019).
69. T. Y. Hu, Y. Wang, C. R. Liao, and D. N. Wang, "Miniaturized fiber in-line Mach-Zehnder interferometer based on inner air cavity for high-temperature sensing," *Optics Letters* **37**, 5082-5084 (2012).
70. P. Lu, L. Men, K. Sooley, and Q. Chen, "Tapered fiber Mach-Zehnder interferometer for simultaneous measurement of refractive index and temperature," *Applied Physics Letters* **94**(2009).
71. B. Dong, Y. Peng, Y. Wang, and C. Yu, "Mode Division Multiplexing in a Fiber Modal Interferometer for Dual-Parameters Measurement," *IEEE Photonics Technology Letters* **28**, 143-146 (2016).
72. B. Yin, S. Wu, M. Wang, W. Liu, H. Li, B. Wu, and Q. Wang, "High-sensitivity refractive index and temperature sensor based on cascaded dual-wavelength fiber laser and SNHNS interferometer," *Opt Express* **27**, 252-264 (2019).
73. Q. F. Ma, Z. Q. Tou, K. Ni, Y. Y. Lim, Y. F. Lin, Y. R. Wang, M. H. Zhou, F. F. Shi, L. Niu, X. Y. Dong, and C. C. Chan, "Carbon-nanotube / Polyvinyl alcohol coated thin core fiber sensor for humidity measurement," *Sensors and Actuators B: Chemical* **257**, 800-806 (2018).
74. J. E. Antonio-Lopez, Z. S. Eznavah, P. LiKamWa, A. Schulzgen, and R. Amezcua-Correa, "Multicore fiber sensor for high-temperature applications up to 1000 degrees C," *Opt Lett* **39**, 4309-4312 (2014).
75. E. Li, X. Wang, and C. Zhang, "Fiber-optic temperature sensor based on interference of selective higher-order modes," *Applied Physics Letters* **89**(2006).
76. X. Wen, T. Ning, Y. Bai, C. Li, J. Li, and C. Zhang, "Ultrasensitive temperature fiber sensor based on Fabry-Perot interferometer assisted with iron V-groove," *Opt Express* **23**, 11526-11536 (2015).

77. F. Zhang, X. Xu, J. He, B. Du, and Y. Wang, "Highly sensitive temperature sensor based on a polymer-infiltrated Mach-Zehnder interferometer created in graded index fiber," *Opt Lett* **44**, 2466-2469 (2019).
78. J. M. Corres, J. Bravo, I. R. Matias, and F. J. Arregui, "Nonadiabatic tapered single-mode fiber coated with humidity sensitive nanofilms," *IEEE Photonics Technology Letters* **18**, 935-937 (2006).
79. J. Mathew, Y. Semenova, G. Rajan, P. Wang, and G. Farrell, "Improving the sensitivity of a humidity sensor based on fiber bend coated with a hygroscopic coating," *Optics & Laser Technology* **43**, 1301-1305 (2011).
80. S. Deng, H. Meng, X. Wang, X. Fan, Q. Wang, M. Zhou, X. Guo, Z. Wei, F. Wang, C. Tan, and X. Huang, "Graphene oxide-film-coated splitting ratio-adjustable Mach-Zehnder interferometer for relative humidity sensing," *Opt Express* **27**, 9232-9240 (2019).
81. W. Liang, Y. Huang, Y. Xu, R. K. Lee, and A. Yariv, "Highly sensitive fiber Bragg grating refractive index sensors," *Applied Physics Letters* **86**(2005).
82. B. Wang, K. Ni, P. Wang, Q. Ma, W. Tian, and L. Tan, "A CNT-coated refractive index sensor based on Michelson interferometer with thin-core fiber," *Optical Fiber Technology* **46**, 302-305 (2018).
83. W. Yan, Q. Han, Y. Chen, H. Song, X. Tang, and T. Liu, "Fiber-loop ring-down interrogated refractive index sensor based on an SNS fiber structure," *Sensors and Actuators B: Chemical* **255**, 2018-2022 (2018).
84. T. Nan, B. Liu, Y. Wu, J. Wang, Y. Mao, L. Zhao, T. Sun, and J. Wang, "Ultrasensitive strain sensor based on Vernier- effect improved parallel structured fiber-optic Fabry-Perot interferometer," *Opt Express* **27**, 17239-17250 (2019).
85. T. Paixao, F. Araujo, and P. Antunes, "Highly sensitive fiber optic temperature and strain sensor based on an intrinsic Fabry-Perot interferometer fabricated by a femtosecond laser," *Opt Lett* **44**, 4833-4836 (2019).
86. T. Paixão, F. Araújo, and P. Antunes, "Highly sensitive fiber optic temperature and strain sensor based on an intrinsic Fabry-Perot interferometer fabricated by a femtosecond laser," *Optics Letters* **44**, 4833 (2019).
87. L. Yi and Y. Changyuan, "Highly stretchable hybrid silica/polymer optical fiber sensors for large-strain and high-temperature application," *Opt Express* **27**, 20107-20116 (2019).
88. L. Yi and Y. Changyuan, "Highly stretchable hybrid silica/polymer optical fiber sensors for large-strain and high-temperature application," *Optics Express* **27**, 20107 (2019).
89. K. Tian, Y. Xin, W. Yang, T. Geng, J. Ren, Y.-X. Fan, G. Farrell, E. Lewis, and P. Wang, "A Curvature Sensor Based on Twisted Single-Mode–Multimode–Single-Mode Hybrid Optical Fiber Structure," *Journal of Lightwave Technology* **35**, 1725-1731 (2017).
90. D. Barrera, J. Madrigal, and S. Sales, "Long Period Gratings in Multicore Optical Fibers for Directional Curvature Sensor Implementation," *Journal of Lightwave Technology* **36**, 1063-1068 (2018).

BIBLIOGRAPHY

91. S. Dong, B. Dong, C. Yu, and Y. Guo, "High Sensitivity Optical Fiber Curvature Sensor Based on Cascaded Fiber Interferometer," *Journal of Lightwave Technology* **36**, 1125-1130 (2018).
92. B. Jiang, Z. Bai, C. Wang, Y. Zhao, J. Zhao, L. Zhang, and K. Zhou, "In-Line Mach-Zehnder Interferometer With D-Shaped Fiber Grating for Temperature-Discriminated Directional Curvature Measurement," *Journal of Lightwave Technology* **36**, 742-747 (2018).
93. S. Marrujo-Garcia, I. Hernandez-Romano, M. Torres-Cisneros, D. A. May-Arriola, V. P. Minkovich, and D. Monzon-Hernandez, "Temperature-independent curvature sensor based on in-fiber Mach-Zehnder interferometer using hollow-core fiber," *Journal of Lightwave Technology*, 1-1 (2020).
94. Q. Zhao, J. Qian, Q. An, and B. Du, "Speedy fabrication of free-standing layer-by-layer multilayer films by using polyelectrolyte complex particles as building blocks," *Journal of Materials Chemistry* **19**(2009).
95. V. Semwal and B. D. Gupta, "Highly sensitive surface plasmon resonance based fiber optic pH sensor utilizing rGO-Pani nanocomposite prepared by in situ method," *Sensors and Actuators B: Chemical* **283**, 632-642 (2019).
96. M. Quan, J. Tian, and Y. Yao, "Ultra-high sensitivity Fabry-Perot interferometer gas refractive index fiber sensor based on photonic crystal fiber and Vernier effect," *Opt Lett* **40**, 4891-4894 (2015).
97. M. Hou, F. Zhu, Y. Wang, Y. Wang, C. Liao, S. Liu, and P. Lu, "Antiresonant reflecting guidance mechanism in hollow-core fiber for gas pressure sensing," *Opt Express* **24**, 27890-27898 (2016).
98. X. Wang, S. Wang, J. Jiang, K. Liu, P. Zhang, W. Wu, and T. Liu, "High-accuracy hybrid fiber-optic Fabry-Perot sensor based on MEMS for simultaneous gas refractive-index and temperature sensing," *Opt Express* **27**, 4204-4215 (2019).
99. B. Xu, J. Huang, X. Xu, A. Zhou, and L. Ding, "Ultrasensitive NO Gas Sensor Based on the Graphene Oxide-Coated Long-Period Fiber Grating," *ACS Appl Mater Interfaces* **11**, 40868-40874 (2019).
100. Q. Yao, G. Ren, K. Xu, L. Zhu, H. Khan, M. Mohiuddin, M. W. Khan, B. Y. Zhang, A. Jannat, F. Haque, S. Z. Reza, Y. Wang, X. Wen, A. Mitchell, and J. Z. Ou, "2D Plasmonic Tungsten Oxide Enabled Ultrasensitive Fiber Optics Gas Sensor," *Advanced Optical Materials* **7**(2019).
101. H. Meng, W. Shen, G. Zhang, C. Tan, and X. Huang, "Fiber Bragg grating-based fiber sensor for simultaneous measurement of refractive index and temperature," *Sensors and Actuators B: Chemical* **150**, 226-229 (2010).
102. C. R. Liao, Y. Wang, D. N. Wang, and M. W. Yang, "Fiber In-Line Mach-Zehnder Interferometer Embedded in FBG for Simultaneous Refractive Index and Temperature Measurement," *IEEE Photonics Technology Letters* **22**, 1686-1688 (2010).
103. C. R. Liao, H. F. Chen, and D. N. Wang, "Ultracompact Optical Fiber Sensor for Refractive Index and High-Temperature Measurement," *Journal of Lightwave Technology* **32**, 2531-2535 (2014).

104. T. Wang and M. Wang, "Fabry–Pérot Fiber Sensor for Simultaneous Measurement of Refractive Index and Temperature Based on an In-Fiber Ellipsoidal Cavity," *IEEE Photonics Technology Letters* **24**, 1733-1736 (2012).
105. X.-Y. Zhang, Y.-S. Yu, C.-C. Zhu, C. Chen, R. Yang, Y. Xue, Q.-D. Chen, and H.-B. Sun, "Miniature End-Capped Fiber Sensor for Refractive Index and Temperature Measurement," *IEEE Photonics Technology Letters* **26**, 7-10 (2014).
106. H. Lu, Y. Yue, J. Du, L. Shao, T. Wu, J. Pan, and J. Hu, "Temperature and liquid refractive index sensor using P-D fiber structure-based Sagnac loop," *Opt Express* **26**, 18920-18927 (2018).
107. Y. Dong, S. Xiao, B. Wu, H. Xiao, and S. Jian, "Refractive Index and Temperature Sensor Based on D-Shaped Fiber Combined With a Fiber Bragg Grating," *IEEE Sensors Journal* **19**, 1362-1367 (2019).
108. W. Yuan and C. Yu, "Dual Demodulation of Temperature and Refractive Index Using Ring Core Fiber Based Mach-Zehnder Interferometer," *Micromachines (Basel)* **12**(2021).
109. X. Li, N. K. Chen, L. Xi, H. Zhang, X. Zhang, W. Zhang, and X. Tang, "Micro-fiber Mach-Zehnder interferometer based on ring-core fiber," *Opt Express* **27**, 34603-34610 (2019).
110. S. Gao, C. Ji, Q. Ning, W. Chen, and J. Li, "High-sensitive Mach-Zehnder interferometric temperature fiber-optic sensor based on core-offset splicing technique," *Optical Fiber Technology* **56**(2020).
111. S. Qizhen, S. Xiaohui, J. Weihua, X. Zhilin, L. Haipeng, L. Deming, and Z. Lin, "Graphene-Assisted Microfiber for Optical-Power-Based Temperature Sensor," *IEEE Photonics Technology Letters* **28**, 383-386 (2016).
112. J. N. Wang and J. L. Tang, "Photonic crystal fiber Mach-Zehnder interferometer for refractive index sensing," *Sensors (Basel)* **12**, 2983-2995 (2012).
113. Y. C. Tan, Z. Q. Tou, V. Mamidala, K. K. Chow, and C. C. Chan, "Continuous refractive index sensing based on carbon-nanotube-deposited photonic crystal fibers," *Sensors and Actuators B: Chemical* **202**, 1097-1102 (2014).
114. J. Kang, J. Yang, X. Zhang, C. Liu, and L. Wang, "Intensity Demodulated Refractive Index Sensor Based on Front-Tapered Single-Mode-Multimode-Single-Mode Fiber Structure," *Sensors (Basel)* **18**(2018).
115. B. Dai, X. Shen, X. Hu, L. Yang, H. Li, J. Peng, and J. Li, "Temperature-Insensitive Refractive Index Sensor with Etched Microstructure Fiber," *Sensors (Basel)* **19**(2019).
116. H. Chunyang, D. Hui, L. Xianli, and D. Shaofei, "Temperature insensitive refractive index sensor based on single-mode micro-fiber Sagnac loop interferometer," *Applied Physics Letters* **104**(2014).
117. G. An, S. Li, T. Cheng, X. Yan, X. Zhang, X. Zhou, and Z. Yuan, "Ultra-stable D-shaped Optical Fiber Refractive Index Sensor with Graphene-Gold Deposited Platform," *Plasmonics* **14**, 155-163 (2018).
118. D. Barot, G. Wang, and L. Duan, "High-Resolution Dynamic Strain Sensor Using a Polarization-Maintaining Fiber Bragg Grating," *IEEE Photonics Technology Letters* **31**, 709-712 (2019).

BIBLIOGRAPHY

119. X. Dong, Z. Luo, H. Du, X. Sun, K. Yin, and J. a. Duan, "Highly sensitive strain sensor based on a novel Mach–Zehnder mode interferometer with TCF-PCF-TCF structure," *Optics and Lasers in Engineering* **116**, 26-31 (2019).
120. L. Lu, Y. Zhou, J. Pan, T. Chen, Y. Hu, G. Zheng, K. Dai, C. Liu, C. Shen, X. Sun, and H. Peng, "Design of Helically Double-Leveled Gaps for Stretchable Fiber Strain Sensor with Ultralow Detection Limit, Broad Sensing Range, and High Repeatability," *ACS Appl Mater Interfaces* **11**, 4345-4352 (2019).
121. L. Costa, H. F. Martins, S. Martin-Lopez, M. R. Fernandez-Ruiz, and M. Gonzalez-Herraez, "Fully Distributed Optical Fiber Strain Sensor With 10–12 $\epsilon/\sqrt{\text{Hz}}$ Sensitivity," *Journal of Lightwave Technology* **37**, 4487-4495 (2019).
122. R. Li, Y. Tan, Y. Chen, L. Hong, and Z. Zhou, "Investigation of sensitivity enhancing and temperature compensation for fiber Bragg grating (FBG)-based strain sensor," *Optical Fiber Technology* **48**, 199-206 (2019).
123. W. Yi-Ping and R. Yun-Jiang, "A novel long period fiber grating sensor measuring curvature and determining bend-direction simultaneously," *IEEE Sensors Journal* **5**, 839-843 (2005).
124. X. Dong, Y. Liu, L.-Y. Shao, J. Kang, and C.-L. Zhao, "Temperature-Independent Fiber Bending Sensor Based on a Superimposed Grating," *IEEE Sensors Journal* **11**, 3019-3022 (2011).
125. B. Sun, Y. Huang, S. Liu, C. Wang, J. He, C. Liao, G. Yin, J. Zhao, Y. Liu, J. Tang, J. Zhou, and Y. Wang, "Asymmetrical in-fiber Mach-Zehnder interferometer for curvature measurement," *Opt Express* **23**, 14596-14602 (2015).
126. S. Zhang, A. Zhou, H. Guo, Y. Zhao, and L. Yuan, "Highly sensitive vector curvature sensor based on a triple-core fiber interferometer," *OSA Continuum* **2**(2019).
127. B. Renganathan, D. Sastikumar, G. Gobi, N. Rajeswari Yogamalar, and A. Chandra Bose, "Nanocrystalline ZnO coated fiber optic sensor for ammonia gas detection," *Optics & Laser Technology* **43**, 1398-1404 (2011).
128. S. H. Kassani, J. Park, Y. Jung, J. Kobelke, and K. Oh, "Fast response in-line gas sensor using C-type fiber and Ge-doped ring defect photonic crystal fiber," *Opt Express* **21**, 14074-14083 (2013).
129. B. Renganathan, D. Sastikumar, G. Gobi, N. R. Yogamalar, and A. C. Bose, "Gas sensing properties of a clad modified fiber optic sensor with Ce, Li and Al doped nanocrystalline zinc oxides," *Sensors and Actuators B: Chemical* **156**, 263-270 (2011).
130. S. H. Kassani, R. Khazaeinezhad, Y. Jung, J. Kobelke, and K. Oh, "Suspended Ring-Core Photonic Crystal Fiber Gas Sensor With High Sensitivity and Fast Response," *IEEE Photonics Journal* **7**, 1-9 (2015).
131. Y. Luo, C. Chen, K. Xia, S. Peng, H. Guan, J. Tang, H. Lu, J. Yu, J. Zhang, Y. Xiao, and Z. Chen, "Tungsten disulfide (WS_2) based all-fiber-optic humidity sensor," *Opt Express* **24**, 8956-8966 (2016).
132. J. Shi, D. Xu, W. Xu, Y. Wang, C. Yan, C. Zhang, D. Yan, Y. He, L. Tang, W. Zhang, T. Liu, and J. Yao, "Humidity Sensor Based on Fabry–Perot Interferometer and Intracavity Sensing of Fiber Laser," *Journal of Lightwave Technology* **35**, 4789-4795 (2017).

133. X. Wang, G. Farrell, E. Lewis, K. Tian, L. Yuan, and P. Wang, "A Humidity Sensor Based on a Singlemode-Side Polished Multimode–Singlemode Optical Fibre Structure Coated with Gelatin," *Journal of Lightwave Technology* **35**, 4087-4094 (2017).
134. Y. Zhao, Y. Peng, M.-q. Chen, F. Xia, and R.-J. Tong, "U-shaped microfiber coupler coated with polyvinyl alcohol film for highly sensitive humidity detection," *Sensors and Actuators A: Physical* **285**, 628-636 (2019).
135. J. Yang, C. Guan, Z. Yu, M. Yang, J. Shi, P. Wang, J. Yang, and L. Yuan, "High sensitivity humidity sensor based on gelatin coated side-polished in-fiber directional coupler," *Sensors and Actuators B: Chemical* **305**(2020).
136. H. Gong, X. Yang, K. Ni, C.-L. Zhao, and X. Dong, "An Optical Fiber Curvature Sensor Based on Two Peanut-Shape Structures Modal Interferometer," *IEEE Photonics Technology Letters* **26**, 22-24 (2014).
137. W. Yuan, Q. Zhao, L. Li, Y. Wang, and C. Yu, "Simultaneous measurement of temperature and curvature using ring-core fiber-based Mach-Zehnder interferometer," *Optics Express* **29**, 17915-17925 (2021).
138. Y. Wang, D. Richardson, G. Brambilla, X. Feng, M. Petrovich, M. Ding, and Z. Song, "Intensity Measurement Bend Sensors Based on Periodically Tapered Soft Glass Fibers," *Opt Lett* **36**, 558–560 (2011).
139. L. Niu, C.-L. Zhao, H. Gong, Y. Li, and S. Jin, "Curvature sensor based on two cascading abrupt-tapers modal interferometer in single mode fiber," *Optics Communications* **333**, 11-15 (2014).
140. Y. Zhao, F. Xia, and M.-q. Chen, "Curvature sensor based on Mach–Zehnder interferometer with vase-shaped tapers," *Sensors and Actuators A: Physical* **265**, 275-279 (2017).
141. O. Frazao, S. F. O. Silva, J. Viegas, J. M. Baptista, J. L. Santos, J. Kobelke, and K. Schuster, "All Fiber Mach–Zehnder Interferometer Based on Suspended Twin-Core Fiber," *IEEE Photonics Technology Letters* **22**, 1300-1302 (2010).
142. Y.-P. Li, W.-G. Zhang, S. Wang, L. Chen, Y.-X. Zhang, B. Wang, T.-Y. Yan, X.-Y. Li, and W. Hu, "Bending Vector Sensor Based on a Pair of Opposite Tilted Long-Period Fiber Gratings," *IEEE Photonics Technology Letters* **29**, 224-227 (2017).
143. C. Lu, J. Su, X. Dong, T. Sun, and K. T. V. Grattan, "Simultaneous Measurement of Strain and Temperature With a Few-Mode Fiber-Based Sensor," *Journal of Lightwave Technology* **36**, 2796-2802 (2018).
144. J. Ma, H. H. Yu, X. Jiang, and D. S. Jiang, "High-performance temperature sensing using a selectively filled solid-core photonic crystal fiber with a central air-bore," *Opt Express* **25**, 9406-9415 (2017).
145. A. D. Gomes, M. Becker, J. Dellith, M. I. Zibaii, H. Latifi, M. Rothhardt, H. Bartelt, and O. Frazao, "Multimode Fabry(-)Perot Interferometer Probe Based on Vernier Effect for Enhanced Temperature Sensing," *Sensors (Basel)* **19**(2019).
146. Y. Wang, C. Shen, W. Lou, F. Shentu, C. Zhong, X. Dong, and L. Tong, "Fiber optic relative humidity sensor based on the tilted fiber Bragg grating coated with graphene oxide," *Applied Physics Letters* **109**(2016).

BIBLIOGRAPHY

147. D. Lopez-Torres, C. Elosua, J. Villatoro, J. Zubia, M. Rothhardt, K. Schuster, and F. J. Arregui, "Photonic crystal fiber interferometer coated with a PAH/PAA nanolayer as humidity sensor," *Sensors and Actuators B: Chemical* **242**, 1065-1072 (2017).
148. R. Chu, C. Guan, Y. Bo, J. Shi, Z. Zhu, P. Li, J. Yang, and L. Yuan, "All-optical graphene-oxide humidity sensor based on a side-polished symmetrical twin-core fiber Michelson interferometer," *Sensors and Actuators B: Chemical* **284**, 623-627 (2019).
149. K. Yang, J. He, C. Liao, Y. Wang, S. Liu, K. Guo, J. Zhou, Z. Li, Z. Tan, and Y. Wang, "Femtosecond Laser Inscription of Fiber Bragg Grating in Twin-Core Few-Mode Fiber for Directional Bend Sensing," *Journal of Lightwave Technology* **35**, 4670-4676 (2017).
150. A. Kumar Paul, A. Krishno Sarkar, A. B. S. Rahman, and A. Khaleque, "Twin Core Photonic Crystal Fiber Plasmonic Refractive Index Sensor," *IEEE Sensors Journal* **18**, 5761-5769 (2018).
151. N. A. M. Zainuddin, M. M. Ariannejad, P. T. Arasu, S. W. Harun, and R. Zakaria, "Investigation of cladding thicknesses on silver SPR based side-polished optical fiber refractive-index sensor," *Results in Physics* **13**(2019).
152. B. Xu, C. Wang, D. N. Wang, Y. Liu, and Y. Li, "Fiber-tip gas pressure sensor based on dual capillaries," *Opt Express* **23**, 23484-23492 (2015).
153. T. Wang, W. Yasukochi, S. Korposh, S. W. James, R. P. Tatam, and S.-W. Lee, "A long period grating optical fiber sensor with nano-assembled porphyrin layers for detecting ammonia gas," *Sensors and Actuators B: Chemical* **228**, 573-580 (2016).
154. F. Tan, S. Chen, W. Lyu, Z. Liu, C. Yu, C. Lu, and H. Y. Tam, "Non-invasive human vital signs monitoring based on twin-core optical fiber sensors," *Biomed Opt Express* **10**, 5940-5951 (2019).
155. F. Tan, W. Lyu, S. Chen, Z. Liu, and C. Yu, "Contactless vital signs monitoring based on few-mode and multi-core fibers," *Opto-Electronic Advances* **3**, 190034-190034 (2020).
156. Z. Chen, D. Lau, J. T. Teo, S. H. Ng, X. Yang, and P. L. Kei, "Simultaneous measurement of breathing rate and heart rate using a microbend multimode fiber optic sensor," *J Biomed Opt* **19**, 057001 (2014).
157. M. Krej, L. Dziuda, and F. W. Skibniewski, "A method of detecting heartbeat locations in the ballistocardiographic signal from the fiber-optic vital signs sensor," *IEEE J Biomed Health Inform* **19**, 1443-1450 (2015).
158. H.-f. Hu, S.-j. Sun, R.-q. Lv, and Y. Zhao, "Design and experiment of an optical fiber micro bend sensor for respiration monitoring," *Sensors and Actuators A: Physical* **251**, 126-133 (2016).
159. M. Fajkus, J. Nedoma, R. Martinek, V. Vasinek, H. Nazeran, and P. Siska, "A Non-Invasive Multichannel Hybrid Fiber-Optic Sensor System for Vital Sign Monitoring," *Sensors (Basel)* **17**(2017).
160. Y. Koyama, M. Nishiyama, and K. Watanabe, "Smart Textile Using Hetero-Core Optical Fiber for Heartbeat and Respiration Monitoring," *IEEE Sensors Journal* **18**, 6175-6180 (2018).

161. S. Wang, X. Ni, L. Li, J. Wang, Q. Liu, Z. Yan, L. Zhang, and Q. Sun, "Noninvasive Monitoring of Vital Signs Based on Highly Sensitive Fiber Optic Mattress," *IEEE Sensors Journal* **20**, 6182-6190 (2020).
162. W. Xu, S. Bian, B. Dong, Y. Shen, S. Han, C. Yu, W. Zhao, and Y. Wang, "Unobtrusive vital signs and activity monitoring based on dual mode fiber," *Optical Fiber Technology* **64**(2021).
163. S. Akita, H. Sasaki, K. Watanabe, and A. Seki, "A humidity sensor based on a hetero-core optical fiber," *Sensors and Actuators B: Chemical* **147**, 385-391 (2010).
164. D. Li, H. Lu, W. Qiu, J. Dong, H. Guan, W. Zhu, J. Yu, Y. Luo, J. Zhang, and Z. Chen, "Molybdenum disulfide nanosheets deposited on polished optical fiber for humidity sensing and human breath monitoring," *Optics Express* **25**(2017).
165. A. Lopez Aldaba, D. Lopez-Torres, C. Elosua, J. L. Auguste, R. Jamier, P. Roy, F. J. Arregui, and M. Lopez-Amo, "SnO₂-MOF-Fabry-Perot optical sensor for relative humidity measurements," *Sensors and Actuators B: Chemical* **257**, 189-199 (2018).
166. B. Jiang, Z. Bi, Z. Hao, Q. Yuan, D. Feng, K. Zhou, L. Zhang, X. Gan, and J. Zhao, "Graphene oxide-deposited tilted fiber grating for ultrafast humidity sensing and human breath monitoring," *Sensors and Actuators B: Chemical* **293**, 336-341 (2019).
167. Y. Yi, Y. Jiang, H. Zhao, G. Brambilla, Y. Fan, and P. Wang, "High-Performance Ultrafast Humidity Sensor Based on Microknot Resonator-Assisted Mach-Zehnder for Monitoring Human Breath," *ACS Sens* **5**, 3404-3410 (2020).
168. J. Li, H. Qu, and M. Skorobogatiy, "Squeezed hollow-core photonic Bragg fiber for surface sensing applications," *Opt Express* **24**, 15687-15701 (2016).
169. J. Li, K. Nallappan, H. Guerboukha, and M. Skorobogatiy, "3D printed hollow core terahertz Bragg waveguides with defect layers for surface sensing applications," *Opt Express* **25**, 4126-4144 (2017).
170. J. Li and K. Nallappan, "Optimization of hollow-core photonic Bragg fibers towards practical sensing implementations," *Optical Materials Express* **9**(2019).
171. W. Yuan, L. Li, Y. Wang, Z. Lian, D. Chen, C. Yu, and C. Lu, "Temperature and curvature insensitive all-fiber sensor used for human breath monitoring," *Optics Express* **29**, 26375-26384 (2021).
172. Y. Wang, G. Yan, Z. Lian, C. Wu, and S. He, "Liquid-level sensing based on a hollow core Bragg fiber," *Opt Express* **26**, 21656-21663 (2018).
173. Z. Liu and H.-Y. Tam, "Fabrication and Sensing Applications of Special Microstructured Optical Fibers," in *Selected Topics on Optical Fiber Technologies and Applications* (2018).
174. B. Du, D. Yang, X. She, Y. Yuan, D. Mao, Y. Jiang, and F. Lu, "MoS₂-based all-fiber humidity sensor for monitoring human breath with fast response and recovery," *Sensors and Actuators B: Chemical* **251**, 180-184 (2017).
175. M. Liu, X. Yin, and X. Zhang, "Double-layer graphene optical modulator," *Nano Lett* **12**, 1482-1485 (2012).
176. M. Mohsin, D. Schall, M. Otto, A. Nocolak, D. Neumaier, and H. Kurz, "Graphene based low insertion loss electro-absorption modulator on SOI waveguide," *Opt Express* **22**, 15292-15297 (2014).

BIBLIOGRAPHY

177. Y. Hu, M. Pantouvaki, J. Van Campenhout, S. Brems, I. Asselberghs, C. Huyghebaert, P. Absil, and D. Van Thourhout, "Broadband 10 Gb/s operation of graphene electro-absorption modulator on silicon," *Laser & Photonics Reviews* **10**, 307-316 (2016).
178. V. Sorianello, M. Midrio, and M. Romagnoli, "Design optimization of single and double layer Graphene phase modulators in SOI," *Opt Express* **23**, 6478-6490 (2015).